

國立交通大學

光電工程研究所

博士學位論文

多面體變異在三元鹵化物及黃銅礦結構化合物對二階非  
線性光學性質影響之理論與實驗研究

Theoretical and experimental studies of second-order nonlinear  
optical properties for various polyhedron distortions in ternary  
halides and some chalcopyrite compounds


研究生： 唐立權  
指導教授： 張振雄 教授  
              黃中堯 教授

中華民國九十八年七月

多面體變異在三元鹵化物及黃銅礦結構化合物對二階非線性光學性質影響  
之理論與實驗研究

Theoretical and experimental studies of second-order nonlinear optical  
properties for various polyhedron distortions in ternary halides and  
some chalcopyrite compounds

研究生： 唐立權                      Student: Li-Chuan Tang  
指導教授： 張振雄 教授          Advisors: Chen-Shiung Chang  
                 黃中堯 教授                      Jung-Yau Huang



國立交通大學  
光電工程研究所  
博士學位論文

A Thesis Submitted to Institute of Electro-Optical Engineering  
College of Electrical and Computer Engineering National Chiao Tung  
University in partial Fulfillment of the Requirements for the Degree of  
DOCTOR OF PHILOSOPHY

in

Electro-Optical Engineering

July 2009

Hsinchu, Taiwan, Republic of China

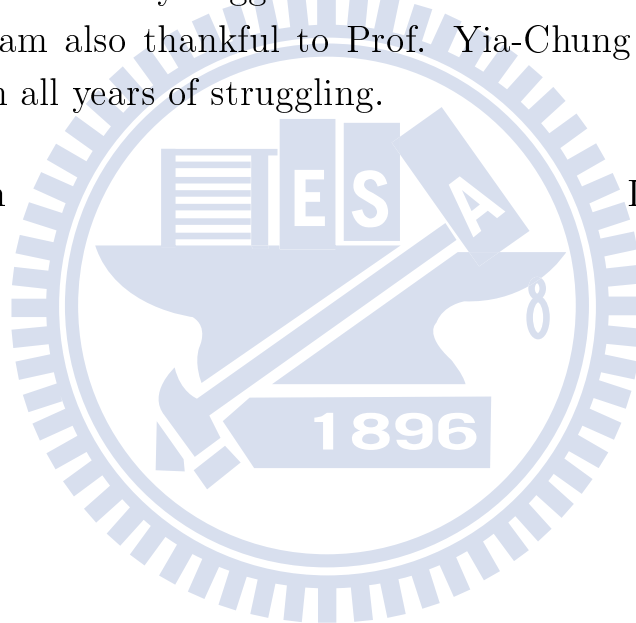
中華民國九十八年七月

## Acknowledgments (誌謝)

I would like to thank Cheng-Shiung Chang and Jung-Yau Huang, my supervisors, for their many suggestions and constant support during this research. I am also thankful to Prof. Yia-Chung Chang for his guidance through all years of struggling.

HsinChu, Taiwan  
June 30, 2009

Li-Chuan Tang



## 中文摘要

鈣鈦礦結構之三元鹵化物是新興的紅外線非線性光學材料，它同時有鈣鈦礦晶體結構變異的有趣議題，也有優良的紅外線非線性光學特性。除了傳統以陰、陽離子半徑所定義的結構變異參數，高史密斯變形因數；本論文也提出了體心陽離子偏移量、面心陰離子偏移量以及（自立方變成菱方）晶胞角度偏移量等三個新的結構參數，同時以第一原理計算方法、晶體合成和實驗方法進行系統化的分析與探討各結構參數對三元鹵化物非線性光學的影響與相關性。從計算與實驗分析結果顯示，菱方晶系的三元鹵化物晶體隨著結構參數的變化同時造成相當大的二階非線性光學係數的變化；電子能態計算結果顯示這系列的晶體具有直接能隙，但並非在倒格子空間的原（伽瑪）點上，而是在倒格子空間的對角點上點上；計算能隙值雖較低於實驗值，而菱方晶系的三元鹵化物晶體具有較大的計算能隙值，此趨勢與實驗值一致。

本論文進一步成長並分析另一屬黃銅礦結構的紅外線非線性光學材料，銀鎳硫、銀鎳硒、銀鎳硫硒；這是陰、陽離子互為四配位四面體離子團內結構的一類



晶體，本論文同樣以第一原理計算方法、晶體成長和實驗方法進行系統化的分析與探討陰離子取代、各結構參數對銀鎵硫、銀鎵硒、銀鎵硫硒非線性光學的影響與相關性。發現陰離子取代，以接近線性比例改變了晶體的能隙、非線性係數與紅外線吸收的截止波長。

由於本論文所使用的第一原理計算方法以及開發附屬計算工具均成功地探討了前述兩類結構的紅外線非線性光學材料，因此，將此理論方法推展至寬能隙黃銅礦結構與相關結構的三元氮化物晶體進行系統化的分析；二價的第一位陽離子、四價的第二位陽離子與氮離子互為四配位四面體離子團內結構，因合成與晶體成長不易，目前可比較、參考的數據、文獻有限，但第一原理計算方法以及所開發附屬計算工具顯示這類三元氮化物晶體具有不同但寬廣的能隙值（約從三個電子伏特到六個電子伏特），實驗值會大於前述的計算值，又兼具非零二階非線性光學係數，可期待此材料在可見光與紫外線非線性光學方面的應用。

## Abstract

Microstructures, electronic structures, linear- and nonlinear-optical properties of the crystals with two main polyhedron categories are examined in this study by using both the first principles calculation and the experimental methods. The studied crystals include the rhombohedral ternary halides ( $ABX_3$  ( $A=Cs, Rb, B=Ge, X=Cl, Br, I$ )), the wide-bandgap ternary nitrides ( $A^{II}B^{IV}N_2$  ( $A^{II} = Be, Mg, B^{IV} = C, Si, Ge$ )), and chalcopyrite  $AgGaS_2$ ,  $AgGaSe_2$ , and  $AgGa(S_xSe_{1-x})_2$ . First, one of the most important parts, systematic studies based on first-principles calculations of second-order optical susceptibilities as well as the dielectric function for  $CsGeX_3$  ( $X=Cl, Br, \text{ and } I$ ; CGX) are presented. The relation between structural properties and the optoelectronic responses are examined. The structural factors,  $\Delta\alpha$ ,  $d_{Ge}$ ,  $d_X$  are proposed to describe the degree of distortion from an ideal perovskite structure.  $\Delta\alpha$  and  $d_{Ge}$  increase when the halide anions are changed

from Cl to I; while halide anion displacement,  $d_X$ , decreases. The structural distortion effect on these rhombohedral CGX crystals is analyzed via the first-principles calculations. The dielectric function and the second harmonic generation (SHG) response coefficient also increase with increasing  $\Delta\alpha$  and  $d_{Ge}$ . The direct bandgaps,  $E_G$ , of CsGeX<sub>3</sub> all occur at the  $R$ -point,  $\Delta E_R$ . The experimental bandgaps of CGX crystals become smaller, i.e.  $E_G^{CGC}(3.67\text{eV}) > E_G^{CGB}(2.32\text{eV}) > E_G^{CGI}(1.53\text{eV})$ , as the  $\Delta\alpha$  and  $d_{Ge}$  increase, i.e.  $d_{Ge}^{CGC} < d_{Ge}^{CGB} < d_{Ge}^{CGI}$ . Partial density of states (PDOS) analysis revealed that the valence band maximum (VBM) and conduction band minimum (CBM) are mainly contributed from the p-orbitals of Germanium. The calculated magnitudes of  $\chi_{ijk}^{(2)}$  are close to some reported experimental values near the band gap. Second, the nonlinear optical (NLO) property of hydrated rubidium germanium chloride (HRGC),  $\text{RbGeCl}_3 \cdot x(\text{H}_2\text{O})$ , is identified. Infrared absorption data support structural evidence that HRGC contain coordinated water molecules with strong hydrogen bond. The infrared spectrum indicated HRGC is transparent in most of the infrared region with only little influence from water. Calculations based on density functional theory shows that the band gap of the  $\text{RbGeCl}_3$  (RGC) crystal is at least 3.84eV, which is larger than that of the infrared

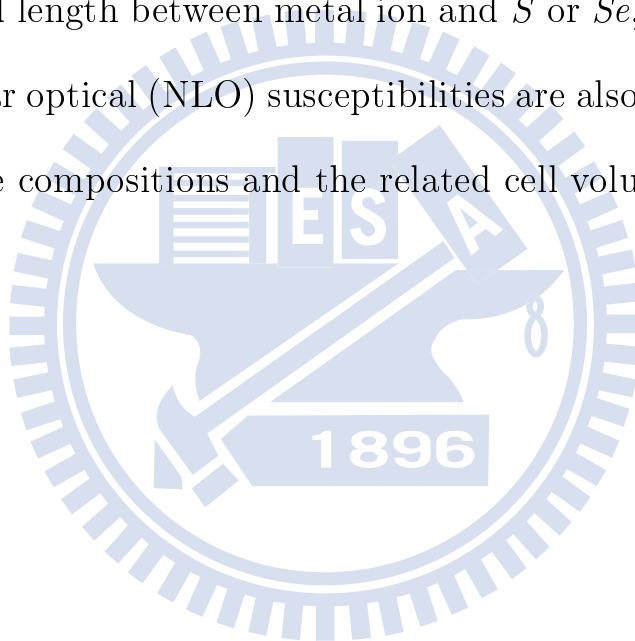
(IR) NLO crystal CsGeCl<sub>3</sub>. Single crystals of HRGC, sized up to 3 × 2 × 1 cm<sup>3</sup>, were grown in aqueous solution by a slow dehydrate technique. The synthetic, structural, and optical properties of an off-centrosymmetric IR nonlinear optical (NLO) RbGeCl<sub>3</sub> · x(H<sub>2</sub>O) crystal were investigated experimentally. Powder second harmonic generation (PSHG) measurement indicates that the crystal structure of HRGC becomes off-centrosymmetric. Precise X-ray diffraction measurements showed that [100] family diffraction peaks split slightly. Unlike the RGC crystal structure whose space group is P2<sub>1</sub> $\bar{m}$ , the HRGC crystal loses the inversion symmetry. Comparisons with known NLO material KH<sub>2</sub>PO<sub>4</sub> (KDP), indicate that HRGC's NLO susceptibility,  $\chi^{(2)}$ , is about one third of that for KDP. The absorption edge of HRGC occurred at 310nm ( $\approx 4.0$  eV), which indicates NLO HRGC crystal can have larger laser damage threshold. According to the *FTIR* measurement, HRGC has a transparent region from 0.31 to 30  $\mu\text{m}$ , thus it can be applied to wider optical spectrum from ultraviolet, visible, to mid-IR.

Third, both tetragonal and orthorhombic ternary nitrides  $A^{II}B^{IV}N_2$  ( $A^{II}=\text{Be, Mg}$ ;  $B^{IV}=\text{C, Si, Ge}$ ) are studied by using the first principles calculation, and are compared to the available experimental results.

This study reveals the electronic properties, linear and second-order nonlinear optical (*NLO*) properties of the ternary nitrides compounds with chalcopyrite structure performed using the Linear Augmented Slater-Type Orbitals (LASTO) method. The linear and second-order optical susceptibilities as functions of frequency are presented. Specifically, we study the relation between the structural properties and the optical responses. Our electronic band structure and projected density of states (PDOS) analysis reveal that these chalcopyrite  $A^{II}B^{IV}N_2$  compounds are direct (with band extrema located at the  $\Gamma$ -point) and their band gaps are wide [from 2.68eV ( $BeGeN_2$ ) to 4.24eV( $MgCN_2$ )]. Our PDOS analysis also shows that the effective masses of highest valence band are heavy in  $MgSiN_2$  and  $MgGeN_2$ , which are different from other  $A^{II}B^{IV}N_2$  compounds. Our calculations show this new category of wide-bandgap ternary nitrides have potential applications in optoelectronics.

Finally, the lattice parameters, electronic structures, optical and bulk properties of tetragonal nonlinear optical crystals,  $AgGa(S_xSe_{1-x})_2$  ( $x=0.0, 0.25, 0.5, 0.75, \text{ and } 1.0$ ), have been analyzed theoretically with first-principle calculation and measured experimentally in each composition. Our calculation results indicate that in these compounds, their

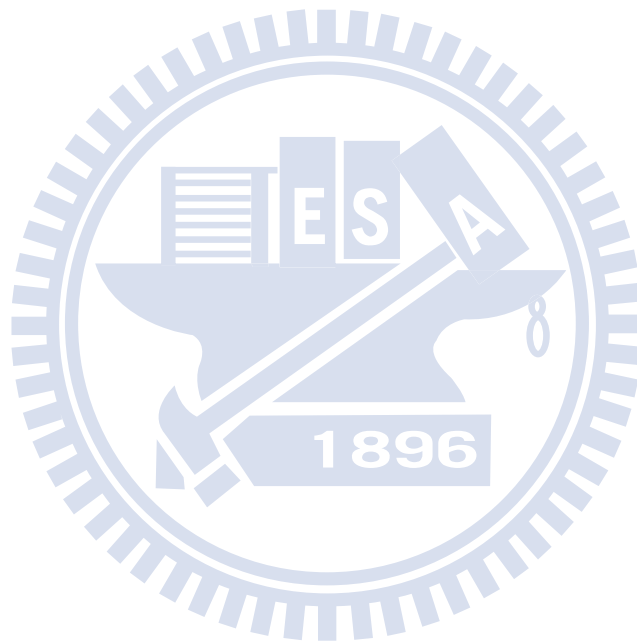
electronic band gaps, optical properties, and bulk moduli are linearly dependent, which are compatible with the experimental measurements. We also find the proportionally mixed electronic contributions from sulfur and selenium at band edges via the partial density of state (PDOS) analysis of . The linear-dependent relationship of their electronic properties can be considered as the cell-volume-effect. Furthermore, the cell parameters, bond length between metal ion and  $S$  or  $Se$ , band gap values, and nonlinear optical (NLO) susceptibilities are also found linearly dependent on the compositions and the related cell volumes.



# Acronym and notation

The terminologies and abbreviations in Optoelectronics and the first principles calculation used in this thesis are based upon the related textbooks and their definitions can also be found in Dmitrev's "Handbook of Nonlinear Optical crystals" [1] and Boyd's "Nonlinear Optics" [2]. For the reader's convenience, the acronyms and notations are listed in Appendices A and B which can be folded out and read in conjunction with the main text.

# 目錄





# Contents

誌謝	iii
中文摘要	iv
英文摘要	vi
Acronym and notation	xi
目錄	xii
圖目錄	xvii
表目錄	xxvi
<b>1 Introduction</b>	<b>1</b>
1.1 Considerations in Opto-Electronic Materials . . . . .	3
1.2 The Ternary Halides . . . . .	5
1.3 The tetrahedron in Chalcopyrite ternary compounds . . .	11

1.4	The First Principles Calculation . . . . .	17
<b>2</b>	<b>Methods for Simulations and Experiments</b>	<b>21</b>
2.1	Synthesis . . . . .	21
2.1.1	Synthesis and Structural Properties . . . . .	24
2.2	X-ray diffraction . . . . .	25
2.3	Single crystal growth by using the vertical Bridgmen furnace . . . . .	27
2.4	Thermogravimetric measurements . . . . .	28
2.5	Second-order nonlinear optical measurements . . . . .	28
2.6	Optical transmission measurements . . . . .	33
2.7	The first principles calculations . . . . .	34
2.7.1	Computational Schemes . . . . .	35
2.7.2	Calculation details for $\text{AgGa}(\text{S}_x\text{Se}_{1-x})_2$ . . . . .	38
2.7.3	Calculations of structural properties . . . . .	41
2.7.4	Calculations of electronic properties . . . . .	43
2.7.5	The Linear Combination of Atomic Orbital Method	43
2.7.6	Optical response functions . . . . .	46
2.7.7	Frequency-dependent Optical Properties . . . . .	49
2.7.8	Second-Order Nonlinear Susceptibilities . . . . .	50

### 3 Innovative Non-linear Optical Material: the Ternary Halides 54

3.1	Structures of Rhombohedral, Cubic, and Tetragonal Ternary Halides . . . . .	55
3.1.1	X-ray diffraction . . . . .	58
3.1.2	Crystal structure and mechanical properties . . . . .	58
3.2	Electronic Band Structures and Density of States Analysis	63
3.3	Electronic and Linear Optical Properties . . . . .	65
3.3.1	Linear Optical Properties and the Electronic Properties . . . . .	67
3.3.2	Linear Optical Properties and the Structural Effects	67
3.4	Nonlinear Optical Properties . . . . .	70
3.4.1	Second-order nonlinear optical susceptibilities . . . . .	76
3.4.2	Structural Effects on Second-Order Nonlinear Susceptibilities . . . . .	78
3.4.3	Electronic Properties and Second-Order Nonlinear Susceptibilities . . . . .	81
3.5	Transmittance spectrum . . . . .	82
3.6	Thermogravimetric Analysis . . . . .	84
3.7	Results and Discussion . . . . .	85

<b>4</b>	<b>Chalcopyrite-like compounds with tetrahedron distortions and their optical properties</b>	<b>103</b>
4.1	Nonlinear optical crystals $AgGa(S_xSe_{1-x})_2$ . . . . .	103
4.1.1	Crystal structure and mechanical properties . . . . .	104
4.1.2	Electronic structures, density of states, and optical spectrum . . . . .	107
4.1.3	Second-order nonlinear optical susceptibilities . . . . .	111
4.2	Innovative Wide Bandgap Materials: the Ternary Nitrides, and their Optical properties . . . . .	113
4.2.1	Hexagonal and Tetragonal Ternary Nitrides . . . . .	113
4.2.2	Electronic and optical properties . . . . .	114
<b>5</b>	<b>Conclusion</b>	<b>129</b>
<b>6</b>	<b>Perspectives</b>	<b>135</b>
	参考文献	137
	附錄	152
<b>A</b>	<b>Acronym</b>	<b>153</b>
<b>B</b>	<b>Notation</b>	<b>155</b>

# 圖目錄



# List of Figures

1.1	The crystal structure of rhombohedral $\text{CsGeX}_3$ is distorted from an ideal perovskite structure. The labels in the figure are the names of species ( $\text{X}=\text{Cl}$ , $\text{Br}$ , and $\text{I}$ ) and the proposed rhombohedral distortion factors. . . . .	10
1.2	The crystal structure of tetragonal chalcopyrite . . . . .	13
1.3	The supercell of two unit cells of the diamond structure .	14
1.4	The supercell of two unit cells of zinc-blende crystal structure . . . . .	15
1.5	Illustrations of the first-principles total energy minimization scheme. . . . .	20
2.1	The synthesis procedure of monoclinic nonlinear optical crystal HRGC. . . . .	23
2.2	Experimental setup used for measuring the second harmonic scattering pattern from a crystalline powder sample.	30

2.3	Float chart of optoelectronic material design from first principles Calculations . . . . .	36
2.4	The crystal structure of tetragonal chalcopyrite . . . . .	40
3.1	X-ray powder diffraction of the crystal HRGC. It is shown that the XRD peaks shift from that of RGC. A major peak height at [310] is observed in the NLO crystals HRGC.	60
3.2	Volume optimuization results for the (a) rhombohedral (R3m) and cubic (Pm-3m) $CsGeCl_3$ ; (b) rhombohedral (R3m) and cubic (Pm-3m) $CsGeBr_3$ ; and (c) rhombohedral (R3m) and orthorhombic (Pmmm) $CsGeI_3$ . . . . .	62
3.3	Results for the calculated electronic band structure of $CsGeX_3$ . . . . .	65
3.4	The density of state analysis of rhombohedral $CsGeX_3$ crystals. . . . .	66
3.5	Imaginary $\chi_{xx}^{(1)}$ and $\chi_{zz}^{(1)}$ for the rhombohedral $CsGeX_3$ crystals. . . . .	68
3.6	Results for the calculated unpolarized dielectric function (the first row) and dielectric function in [111] direction of rhombohedral $CsGeX_3$ . . . . .	70

3.7	The total (a) absolute, (b) imaginary part, and (c) real part of frequency-dependent second-order nonlinear optical susceptibility, component $\chi_{zxx}^{(2)}$ , by using equation 2.27 are calculated for <i>CsGeCl<sub>3</sub></i> (black), <i>CsGeBr<sub>3</sub></i> (red), and <i>CsGeI<sub>3</sub></i> (green). . . . .	91
3.8	The total (a) absolute, (b) imaginary part, and (c) real part of frequency-dependent second-order nonlinear optical susceptibility, component $\chi_{zzz}^{(2)}$ , by using equation 2.27 are calculated for <i>CsGeCl<sub>3</sub></i> (black), <i>CsGeBr<sub>3</sub></i> (red), and <i>CsGeI<sub>3</sub></i> (green). . . . .	92
3.9	The powder second harmonic generation results of rhombohedral nonlinear optical crystal <i>CsGeBr<sub>3</sub></i> . . . . .	93
3.10	The comparison of integrated powder second harmonic generation intensity of nonlinear optical crystal <i>KDP</i> , <i>CsGeCl<sub>3</sub></i> and <i>CsGeBr<sub>3</sub></i> . . . . .	94
3.11	One of the as-grown <i>RbGeCl<sub>3</sub> · x(H<sub>2</sub>O)</i> crystals and the crystal structure model of the monoclinic <i>RbGeCl<sub>3</sub></i> crystal, whose space group is <i>P2<sub>1</sub><math>\bar{m}</math></i> . . . . .	95



3.12	Analysis of hydradizayion contribution in the NLO crystals the second-harmonic susceptibility $\chi^{(2)}$ and the scaled values of $\chi^{(2)}$ of the NLO crystals $RbGeCl_3H_2O$ . . . . .	96
3.13	Electronic band structure of the crystals $RbGeCl_3$ . . . . .	97
3.14	The density of state analysis contribution in the crystals $RbGeCl_3$ . . . . .	97
3.15	(a) Measured transmittance of the crystal $RbGeCl_3 \cdot x(H_2O)$ . (b) The measured FTIR of the crystal $RbGeCl_3 \cdot x(H_2O)$ . (c) The measured Raman spectra the crystal $RbGeCl_3 \cdot x(H_2O)$ . . . . .	98
3.16	The transmission analysis of rhombohedral nonlinear optical crystal $CsGeBr_3$ in the mid-infrared range . . . . .	98
3.17	The thermal analysis of (a) rhombohedral nonlinear optical crystal $CsGeBr_3$ m and (b) monoclinic nonlinear optical crystal HRGC. . . . .	99

3.18	Second-order nonlinear optical susceptibility components of rhombohedral CsGeCl <sub>3</sub> projected for various atomic species and energy bands using eq. 2.25. The contribution of each species is projected to $\chi_{xzx}^{(2)} (= \chi_{zxx}^{(2)})$ , $\chi_{yyy}^{(2)}$ , and $\chi_{zzz}^{(2)}$ in CsGeCl <sub>3</sub> . Absolute value of SHG susceptibility $\chi_{xyz}^{(2)}(\omega; \omega, 0)$ , solid line for CsGeCl <sub>3</sub> . . . . .	100
3.19	Second-order nonlinear optical susceptibility components of rhombohedral CsGeBr <sub>3</sub> projected for various atomic species and energy bands using eq. 2.25. The contribution of each species is projected to $\chi_{xzx}^{(2)} (= \chi_{zxx}^{(2)})$ , $\chi_{yyy}^{(2)}$ , and $\chi_{zzz}^{(2)}$ in CsGeBr <sub>3</sub> . Absolute value of SHG susceptibility $\chi_{xyz}^{(2)}(\omega; \omega, 0)$ , solid line for CsGeBr <sub>3</sub> . . . . .	101
3.20	Second-order nonlinear optical susceptibility of components of rhombohedral CsGeI <sub>3</sub> projected for various atomic species and energy bands using eq. 2.25. The contribution of each species is projected to $\chi_{xzx}^{(2)} (= \chi_{zxx}^{(2)})$ , $\chi_{yyy}^{(2)}$ , and $\chi_{zzz}^{(2)}$ in CsGeI <sub>3</sub> . Absolute value of SHG susceptibility $\chi_{xyz}^{(2)}(\omega; \omega, 0)$ , solid line for CsGeI <sub>3</sub> . . . . .	102

4.1	X-ray powder diffraction of the NLO crystals $AgGa(S_xSe_{1-x})_2$ . It is shown that the XRD peaks shift with S composition. A minimum peak height at [312] is observed when the S and Se was half substitution in the NLO crystals $AgGa(S_xSe_{1-x})_2$ . . . . .	106
4.2	Absorption edge measurements of the NLO crystals $AgGa(S_xSe_{1-x})_2$ .	108
4.3	The first-principles calculated bandgaps and photo-luminescence measurements of the NLO crystals $AgGa(S_xSe_{1-x})_2$ . (*): ref.[3] . . . . .	109
4.4	Band structures of the NLO crystals $AgGa(S_xSe_{1-x})_2$ . . . . .	110
4.5	Analysis of partial density of states (PDOS) of s- and p-orbital contribution via S and Se in the NLO crystals $AgGa(S_xSe_{1-x})_2$ . . . . .	119
4.6	The first-principles calculation of the second-harmonic susceptibility $\chi^{(2)}$ and the scaled values of $\chi^{(2)}$ of the NLO crystals $AgGa(S_xSe_{1-x})_2$ . The scaled $\chi^{(2)}$ values are estimated from that of the $AgGaS_2$ with a cubic power of $E_g$ . . . . .	120

4.7 Electronoc band-structures of various chalcopyrite  $A^{II}B^{IV}N_2$  ( $A^{II}=\text{Be, Mg}; B^{IV}=\text{C, Si, Ge}$ ) with sapce group symmetry I-42d (no. 122). They are (a)  $BeCN_2$ ; (b)  $BeSiN_2$ ; (c)  $BeGeN_2$ ; (d)  $MgCN_2$ ; (e)  $MgSiN_2$ ; and (f)  $MgGeN_2$ .  
122

4.8 The band-structures of (a) chalcopyrite  $ZnGeN_2$  and (b) orthorhombic  $ZnGeN_2$ . . . . . 123

4.9 Density of State of various chalcopyrite  $A^{II}B^{IV}N_2$  ( $A^{II}=\text{Be, Mg}; B^{IV}=\text{C, Si, Ge}$ ) with sapce group symmetry I-42d (no. 33). They are (a) $BeCN_2$ ; (b) $BeSiN_2$ ; (c) $BeGeN_2$ ; (d) $MgCN_2$ ; (e) $MgSiN_2$ ; and (f) $MgGeN_2$ ; . . . . . 124

4.10 Dielectric functions of various tetragonal  $A^{II}B^{IV}N_2$  ( $A^{II}=\text{Be, Mg}; B^{IV}=\text{C, Si, Ge}$ ) with sapce group symmetry I-42d (no. 122). They are (a) $BeCN_2$ ; (b) $BeSiN_2$ ; (c) $BeGeN_2$ ; (d) $MgCN_2$ ; (e) $MgSiN_2$ ; and (f) $MgGeN_2$ ; . . . . . 125

4.11 Frequency-dependent second order nonlinear susceptibilities of various tetragonal  $A^{II}B^{IV}N_2$  ( $A^{II}=\text{Be, Mg}; B^{IV}=\text{C, Si, Ge}$ ) with space group symmetry I-42d (no. 122). They are (a) Total  $\chi_{xyz}^{(2)}(-2\omega; \omega, \omega)$  responses; (b) Totally imaginary  $\chi_{xyz}^{(2)}(-2\omega; \omega, \omega)$  responses; (c) Totally real  $\chi_{xyz}^{(2)}(-2\omega; \omega, \omega)$  responses; . . . . . 126

4.12 Frequency-dependent second order nonlinear susceptibilities of various tetragonal  $A^{II}B^{IV}N_2$  ( $A^{II}=\text{Be, Mg}; B^{IV}=\text{C, Si, Ge}$ ) with space group symmetry I-42d (no. 122). They are (a) Total  $\chi_{zxy}^{(2)}(-2\omega; \omega, \omega)$  responses; (b) Totally imaginary  $\chi_{zxy}^{(2)}(-2\omega; \omega, \omega)$  responses; (c) Totally real  $\chi_{zxy}^{(2)}(-2\omega; \omega, \omega)$  responses. . . . . 127

4.13 Absolute values of frequency-dependent second order nonlinear susceptibilities for both structures I-42d and Pna21.  
128

# 表目錄



# List of Tables

3.1	Distorted structural factors obtained from the experimental lattice constants and the First-Principles results of the Rhombohedral NLO crystals $CsGeX_3$ . . . . .	57
3.2	Lattice constants and the $Ge$ 's fractional coordinates of the Rhombohedral NLO crystals $CsGeBr_3$ and $CsGeCl_3$ . The first principles calculation results and the measured values by using the XRD and Rietveld refinement were compared. . . . .	59
3.3	Bulk modulus, the optimized volumes, and the minimized total energies of the rhombohedral $NLO$ crystals $CsGeX_3$ . . . . .	89

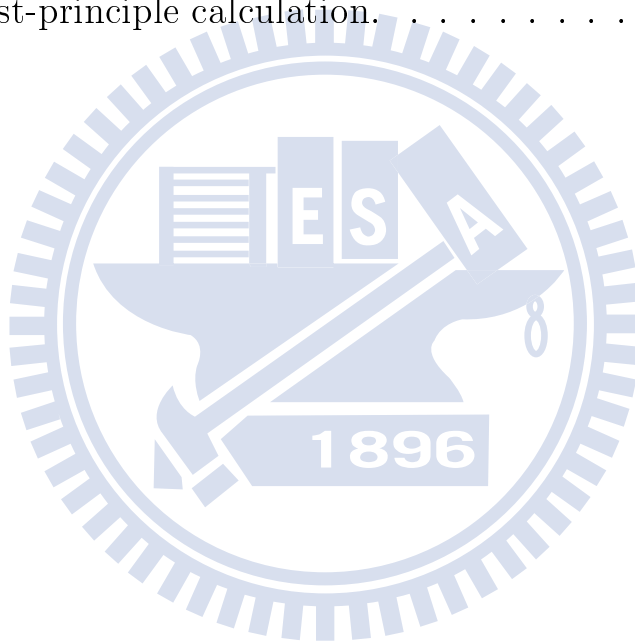
3.4	Calculated optical properties, the linear and second order optical responses at zero frequency and non-linear optical coefficients of $CsGeX_3$ (X=Cl, Br, and I) crystals . Available experimental data are also listed for comparison. . . . .	90
3.5	Non-linear optical coefficients of NLO crystals $CsGeBr_3$ , $CsGeCl_3$ , $KDP$ (as a reference), and $BBO$ . They were integrated from the reflection powder second-harmonic generation signals in same measured conditions . . . . .	90
3.6	Second-order non-linear optical susceptibilities of rhombohedral $CsGeCl_3$ , $CsGeBr_3$ , and $CsGeI_3$ crystals. They were estimated from the <i>ab initio</i> without employing the band-gap correction scheme . . . . .	93
4.1	Structural parameters, bond-lengths, and bulk modulus of the NLO crystals $AgGa(S_xSe_{1-x})_2$ . The calculated values are obtained via first-principles calculation with the supercell model. . . . .	117



4.2 Structural parameters and bond-lengths of the NLO crystals  $AgGa(S_xSe_{1-x})_2$ , which are obtained via first-principles calculation with the single-unit-cell model. . . . . 118

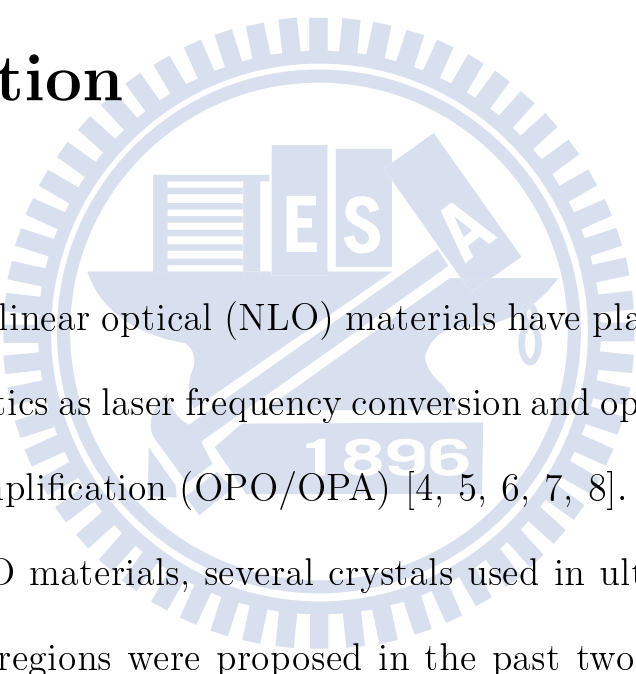
4.3 The structural parameters of the NLO crystals  $A^{II}B^{IV}N_2$ . 121

4.4 The calculated bandgap values and optical susceptibilities in zero frequency of the NLO crystals  $A^{II}B^{IV}N_2$  by using first-principle calculation. . . . . 123



# Chapter 1

## Introduction



Second-order nonlinear optical (NLO) materials have played a key role in such area of optics as laser frequency conversion and optical parametric oscillation/amplification (OPO/OPA) [4, 5, 6, 7, 8]. For inorganic second-order NLO materials, several crystals used in ultraviolet (UV) and visible (vis) regions were proposed in the past two decades, e.g.,  $\text{KH}_2\text{PO}_4$  (KDP),  $\text{KTiOPO}_4$  (KTP),  $\beta\text{-BaB}_2\text{O}_4$  (BBO),  $\text{LiB}_3\text{O}_5$  (LBO), etc. But in the infrared (IR) region the current materials, such as  $\text{AgGaSe}_2$ ,  $\text{ZnGeP}_2$ , are not good enough for applications, mainly due to their low laser damage threshold, as their band gaps are narrow. So the search for new NLO materials in IR region becomes one of the most

important challenges due to their potentially wide applications in fields such as laser technology and molecular spectroscopy [1]. Not only the UV NLO materials but also the IR ones are still under-explored.

However, choosing a proper crystal or material is always a crucial consideration. Relating properties of substances to their structures has been a major objective of modern physics and this also happens to be a prime concern of solid state physicists. Some of the properties of importance in condensed matter physics are electronic, magnetic, dielectric and optical. An important class of materials is that of ferroics, which possess several orientation states that can be switched from one to another by the application of an appropriate force; ferroelectric materials, e.g. the rhombohedral perovskite ternary halides and oxides, [9, 10, 11, 12, 13, 14, 15] form a very important subgroup of this class of materials. The other important class of materials discussed here is the tetrahedrons in chalcopyrite crystals which has been gained considerable importance in recent years. In this study, the electronic and optical properties to the polyhedron influences on the rhombohedrally distorted perovskite ternary halides and some important chalcopyrite

compounds, e.g. the ternary nitrides ( $ABN_2$ ),  $AgGaS_2$ ,  $AgGaSe_2$ , and  $AgGa(SSe)_2$ .<sup>[16]</sup> The requirements of the NLO materials and the related compounds are introduced below.

## 1.1 Considerations in Opto-Electronic Materials

The major concern of an opto-electronic crystal is its electronic properties, or the electronic band structure behavior. For instance, the absorption edge and the damage threshold are directly proportional to the bandgap, and the optical susceptibilities are inversely proportional to the bandgaps, etc. However, a good SHG material should also consider the following attributes: transparency in the relevant wavelengths; ability to withstand laser irradiation and chemical stability. Most importantly, the material in question must be crystallographically non-centrosymmetric (NCS). Mathematically it has been known for some time that only an NCS arrangement of atoms can produce a second-order NLO response [1, 2, 17]. These four specifications are related to electronic band structure behaviors, e.g., the damage threshold is

directly proportional to the bandgap of the crystal. So, the electronic related measurements and calculations of electronic properties are the first important task on studying these SHG materials.

As a new class of rhombohedral ternary halides  $ABX_3$  ( $A = \text{Cs, Rb}$ ,  $B = \text{Ge, Cd}$ ,  $X = \text{Cl, Br, I}$ ) [18, 19, 20] crystals will be examined whether they meet all the above requirements or not. Furthermore,  $ABX_3$  have the potential applications on the higher-order nonlinear optical behaviors like the perovskite ternary oxides, e.g.  $\text{BaTiO}_3$ . [13, 14, 15]

In order to correlate the structure and physical properties of optoelectronic solids, it is essential to have a description of valence electrons that bind the atoms in the solid state. Two limiting descriptions of atomic outer electrons are available: the band theory and the localized-electron theory or the ligand-field theory. When there is appreciable overlap between orbitals of neighbouring atoms, the band theory of Bloch and Wilson is applicable. The theory assumes that valence electrons are shared equally by all the like atoms in the crystals. In the last decade, a great deal of attention has been denoted to the wide-band-

gap material with chalcopyrite structure, e.g. the ternary nitrides.

## 1.2 The Ternary Halides

Ternary halides are potential materials for nonlinear optical applications in the infrared because of their transparency. [21] Recently, several ternary halides in  $ABX_3$  ( $A=Cs, Rb, B=Ge, Cd, X=Cl, Br, I$ ) [19, 20, 18, 12, 22, 23, 23, 24, 11] were discovered to exhibit second-order NLO properties. Rhombohedral  $CsGeCl_3$  (CGC) was found to possess excellent second-order NLO properties, displaying a second-harmonic generation (SHG) efficiency five times larger than that of  $KH_2PO_4$  (KDP) and a damage threshold of  $200MW/cm^2$  [23]. The electronic and linear optical properties of  $CsGeI_3$  (CGI) were also reported by Tang *et al* [12]. At the same time,  $CsCdBr_3$  was found by Ren *et al* [25] to be NCS, i.e. the symmetry of inversion center is absent. Rhombohedral  $CsGeBr_3$  (CGB), which was found to possess better second-order NLO properties than CGC, exhibiting a SHG about ten times larger than that of KDP [11]. The ternary halides recently

became a new category of nonlinear optical (NLO) materials, which are potentially applicable from visible to infrared. These NLO applications include difference-frequency mixing, optical parametric generation and amplification. The electronic and linear optical properties of  $CsGeI_3$  were also reported by Tang *et al*[12].  $CsCdBr_3$  was found to be non-centrosymmetric, i.e., lack of inversion symmetry, by Ren *et al*[25]. At the same time, Ren *et al.* also reported a structure-tuned ternary halide, i.e.  $RbCdI_3 \cdot xH_2O$  (rubidium cadmium iodide monohydrate, RCIM)[26], which showed sizable second-order NLO effects. Similar to RCIM, HRGC [ $RbGeCl_3 \cdot x(H_2O)$ , with  $0.0 \leq x \leq 0.2$ ] also possesses strong NLO effects, which are also examined in this work.

One of the continued challenges in ternary halides concerns the elucidation of structure-property relationships. Nowhere is this more true than the second-order nonlinear optical (NLO) properties, i.e., SHG properties. Viable SHG materials must possess the attributes which mentioned in Chap. 1.1.

In an ideal perovskite structure, the cell parameters are  $a = b = c$

and  $\alpha = \beta = \gamma = 90^\circ$  with cubic space group  $Pm - 3m$  (No. 221) as in the high temperature phases of cubic  $CsGeCl_3$  and  $CsGeBr_3$  [27, 28, 29, 30, 31]. The cell parameters of cubic  $CsGeBr_3$  are  $a = b = c = 5.362\text{\AA}$  and  $\alpha = \beta = \gamma = 90^\circ$  with space group  $Pm - 3m$  (No. 221). The cell edges of rhombohedral (room temperature phase)  $CsGeBr_3$  are longer than those of the cubic (high temperature) phase, and the lattice angles of rhombohedral (room temperature phase)  $CsGeBr_3$  are slightly smaller than  $90^\circ$ .

The structural distortion was considered as one of the contributions to  $CsGeX_3$ 's optical nonlinearity. For perovskite-type ternary oxides  $ABO_3$  and halides  $CsGeX_3$ , Goldschmidt's tolerance factor  $t_G$  [32, 33] serves as a discriminating parameter for classifying perovskites in terms of their structure modifications and the resulting physical properties [34, 35, 36, 37, 38]. The type of stacking depends on the tolerance factor  $t_G$  [32, 33]

$$t_G = \frac{(r_A + r_X)}{\sqrt{2} \cdot (r_B + r_X)}, \quad (1.1)$$

where  $A$  denotes the large cation,  $B$  the smaller one,  $X$  the anion, and



$r$  the ionic radii of Shannon and Prewitt [39, 40], which depend on the coordination number and bonding-specimens. According to the empirical condition, a crystal structure tends to follow an ideal perovskite model when  $0.97 \leq t_G \leq 1.03$ . The structural parameters of  $CsGeBr_3$ , which were reported in Refs. [27, 28, 29, 30, 31], are listed in Table 3.2. The reported lattice parameters of  $CsGeX_3$  at room temperature, and the atomic positions of ternary halide crystals obtained by using the WIEN2k[41] package are summarized in the last three rows in Table 3.2 for comparison. The tolerance factors,  $t_G$ , of  $CsGeX_3$  crystals are 1.009(4), 1.027, and 0.984, respectively. (see the far right column in Table 3.2). They are close to the empirically ideal perovskite structure with  $t_G = 1.0$ . Thus, the CGX crystals should behave like an ideal perovskite structure. However, experimental evidence indicates that CGX crystals at room temperature all have a rhombohedral structure. To give a better description, it seems necessary to consider the effect of some extra structure factors.

First, the lattice angles reduce uniformly and slightly in comparison to

the ideal perovskite structure.

$$\Delta\alpha = \frac{(90 - \alpha_{rhomb})}{90} \times 100. \quad (1.2)$$

Second, the smaller B-site cation, Germanium, displaces along the diagonal axis from the cell center to the corner by a distance

$$d_{Ge}^{rhomb} = |(\vec{r}_{Ge}^{fc} - \vec{r}_{Ge}^{rhomb})| \times 100. \quad (1.3)$$

Finally, the displacements of different anions, X(=Cl, Br, and I), can be described as

$$d_X^{rhomb} = |(\vec{r}_X^{fc} - \vec{r}_X^{rhomb})| \times 100, \quad (1.4)$$

where  $\vec{r}$  denotes the position vector of ions in fractional coordinates. These factors are also illustrated in Figure 1.1.

In this thesis, there are some interesting features about the rhombohedral CGX crystals which will be discussed. First of all, CGX materials have the same crystal structure, and they possess identical space group symmetry, R3m (160). Traditional empirical equation, the Goldschmidt's tolerance factor[32, 33], cannot properly predict their crystal models. CGX crystals typically exhibit a rhombohedral deformation from an ideal perovskite crystal structure. Second, they have large NLO susceptibility. Third, the transparent spectra of CGX crystals can be extended to much longer wavelength ( $\approx 20\mu\text{m}$ ) in infrared

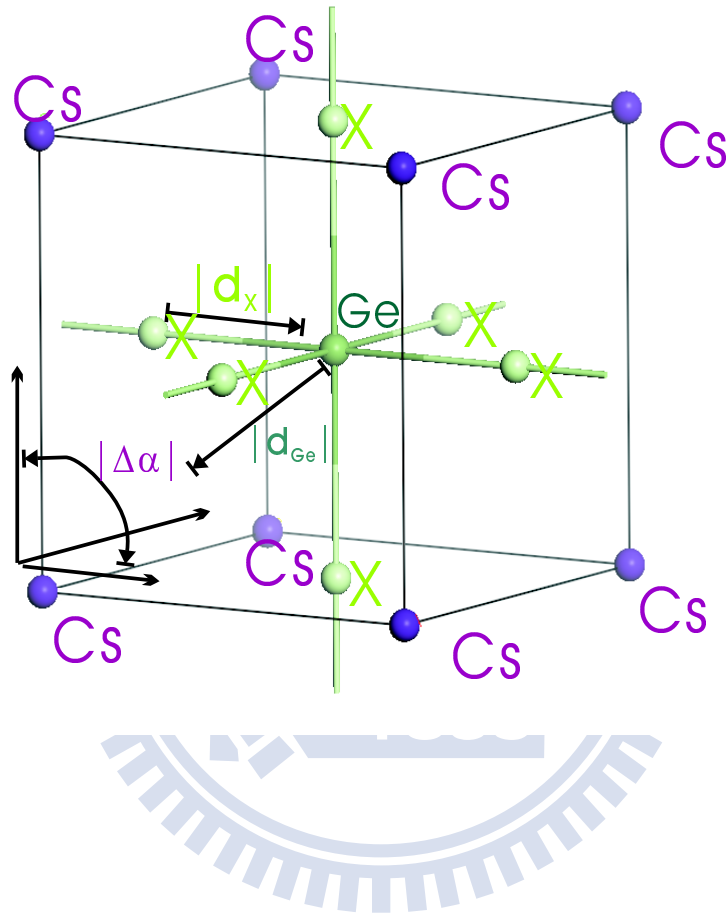


圖 1.1: The crystal structure of rhombohedral  $\text{CsGeX}_3$  is distorted from an ideal perovskite structure. The labels in the figure are the names of species ( $X=\text{Cl}$ ,  $\text{Br}$ , and  $\text{I}$ ) and the proposed rhombohedral distortion factors.

range. Therefore, CGX crystals could have applications in wider optical spectral range. The only shortcoming of CGX crystals is that good crystal size and quality are difficult to achieve. In this study, the first two interesting features mentioned above would be emphasized. In order to understand the properties of  $CsGeX_3$  crystals mentioned in the previous paragraph systematical analysis on the effect of CGX's structural factor on their electronic and optical properties is carried out.

Both the experimental and calculated lattice parameters will be compared in Chap. ??.

### 1.3 The tetrahedron in Chalcopyrite ternary compounds

In the last decade, a great deal of attention has devoted to the wide-band-gap material with chalcopyrite structure, e.g. the ternary nitrides.[42]

The ternary  $A^{II}B^{IV}N_2$  ( $A^{II} = Be, Mg, B^{IV} = C, Si, Ge$ ) compounds are derived from III-V compounds by replacing the group-III element

with group-II and group-IV elements. The hexagonal  $A^{II}B^{IV}N_2$  structurally ordered compounds with space group of Pna21 (pseudo-wurtzite structure) [43] were studied by J. Y. Huang et al, and the interesting electronic, optical and structural properties were reported in the same article. However, there were few research results in  $II - IV - N_2$  compounds which have structure changes from zinc-blende to chalcopyrite structure with space group of I-42d (pseudo-zinc-blende structure) [44]. Similar to  $AgGaS_2$ ,  $AgGaSe_2$ ,  $AgGa(S_xSe_{1-x})_2$ , [16]  $II-IV-P_2$ , and/or  $II-IV-As_2$  compounds, chalcopyrite  $II-IV-N_2$  compounds are expected to have a large optical non-linearity. Thus,  $A^{II}B^{IV}N_2$  compounds have potential applications in optical band-pass and/or band-rejection filters, second harmonic generators, optical mixers, and parametric oscillators, like other chalcopyrite compounds [45].

The crystal structure of the tetragonal chalcopyrite,  $A^{II}B^{IV}N_2$ , is shown in Fig. 1.2. Comparing with the diamond structure in fig. 1.3 and the Zinc-blende structure in fig. 1.4, the unit cell of a chalcopyrite exhibits  $I\bar{4}2d$  symmetry ( $a = b \neq c$ ,  $\alpha = \beta = \gamma = 90^\circ$ )[46, 47], which can be considered as a superstructure of two zinc-blende structures. Four metal

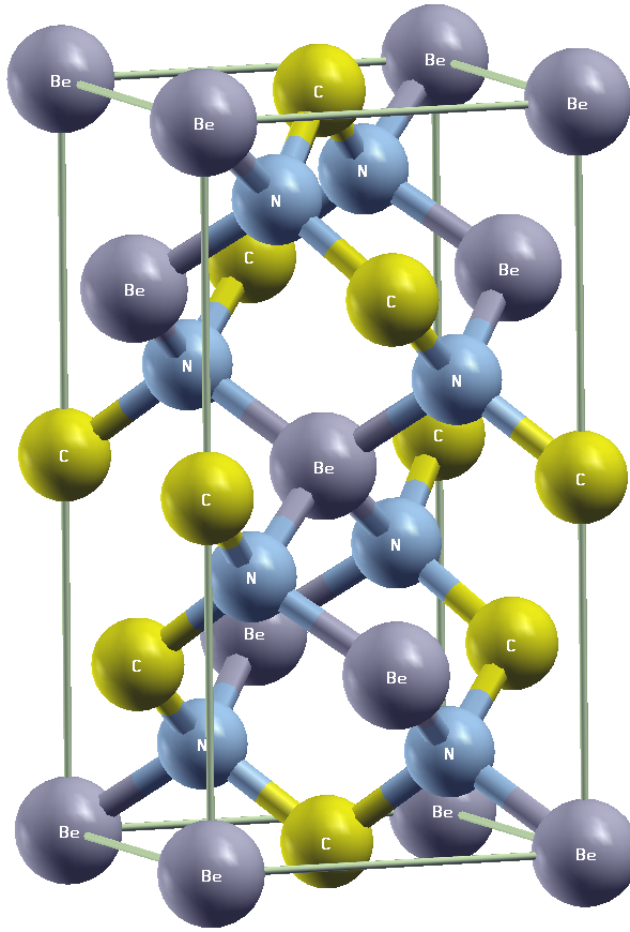


圖 1.2: The crystal structure of tetragonal chalcopyrite

atoms  $A^{II}$ ,  $B^{IV}$ , and eight crystallographically equivalent  $N$  atoms occupy the positions  $[(x, y, z); (\bar{x}, \bar{y}, \bar{z}); (y, \bar{x}, \bar{z}); (\bar{y}, x, \bar{z}); (\bar{x}+1/2, y, \bar{z}+3/4); (x+1/2, \bar{y}, \bar{z}+3/4); (\bar{y}+1/2, \bar{x}, z+3/4); (y+1/2, x, z+3/4)]$ . In chalcopyrite  $A^{II}B^{IV}N_2$  ( $A^{II} = Be, Mg, B^{IV} = C, Si, Ge$ ) crystals, metal atoms are tetrahedrally coordinated around  $N$  and vice versa. II-IV- $V_2$  compounds have a large optical non-linearity, and they are promising materials.  $ZnGeN_2$  is one of the II-IV- $V_2$  compounds, and expected to

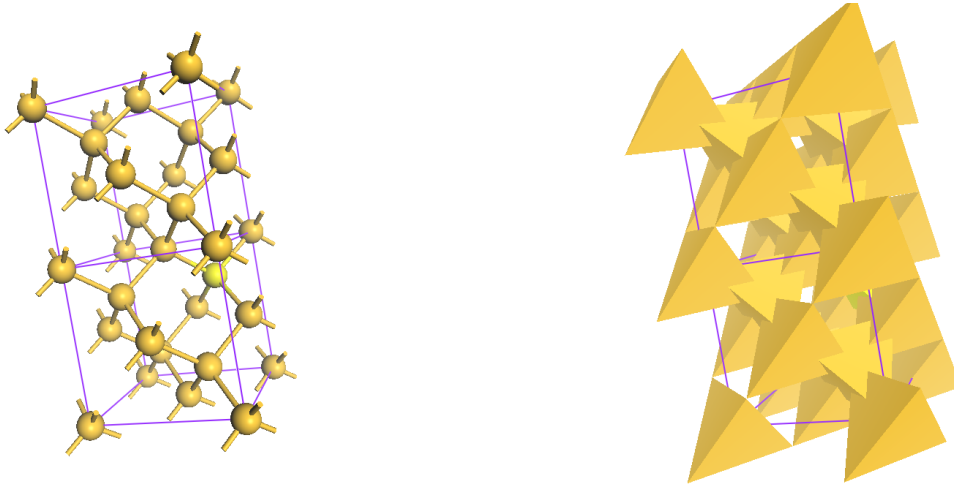


圖 1.3: The supercell of two unit cells of the diamond structure

have a wide band gap. Our theoretical calculation shows that there is a large difference in refractive index between  $ZnGeN_2$  and GaN. Moreover,  $A^{II}B^{IV}N_2$  compounds have a small lattice mismatch to GaN along the a-axis and their optical properties remain unexplored. In this study, linear and nonlinear optical properties of single crystalline  $A^{II}B^{IV}N_2$  compounds are investigated.

The chalcopyrite structure has two types of distortion, namely, tetragonal ( $\eta = c/2a \neq 1$ ) and tetrahedral (described by an internal parameter  $u$ ) with respect to the zinc-blende cubic structure [48, 49, 50]. The parameter  $u$  can be used as a measure of bond-length mismatch through

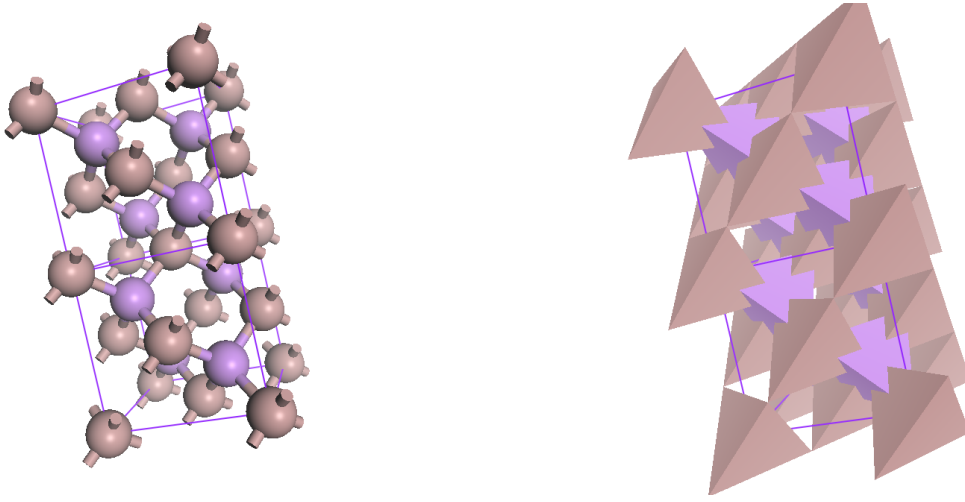


圖 1.4: The supercell of two unit cells of zinc-blende crystal structure

the relation

$$(u - 0.25)^2 = \frac{d_{AN}^2 - d_{BN}^2}{a^2}, \quad (1.5)$$

where the subscripts  $A = Be, Mg$ , and  $B = C, Si, Ge$ .

Recently, epitaxial growth of  $ZnGeN_2$  was succeeded on GaN/sapphire [25] or sapphire substrates [11]. Absorption spectra and excitonic luminescence of  $ZnGeN_2$ , and their temperature dependence were reported [32, 33].  $A^{II}B^{IV}N_2$  ( $A^{II} = Be, Mg$ ,  $B^{IV} = C, Si, Ge$ ) compounds, however, have not been well investigated. In this work, we report studies on the electronic band structures, linear and nonlinear optical responses such as the complex dielectric functions and the frequency-



dependent  $\chi_{ijk}^{(2)}(-2\omega; \omega, \omega)$  susceptibilities by means of the Linear Augmented Slater-Type Orbitals (LASTO) method. [51, 52, 53, 54, 55] The anisotropy of optical properties for  $A^{II}B^{IV}N_2$  is also examined.

The most important technique to generate tunable coherent radiation in the mid-infrared spectrum is based on second order nonlinear optical (NLO) processes in a noncentrosymmetric crystal. These NLO processes include difference-frequency mixing, optical parametric generation and amplification.

Crystals used for mid-IR generation with frequency down conversion schemes should possess wide optical transparency range from  $1\mu\text{m}$  to well beyond  $5\mu\text{m}$ . Currently those crystals are very limited and only a few of them have really become commercially available [56]. Among those candidates,  $AgGaS_2$  and  $AgGaSe_2$  are well known with their wide transparency, large birefringence, high optical damage threshold and nonlinearity. To meet the demand from specific applications, one may wish to adjust the linear and nonlinear optical properties of  $AgGa(S_xSe_{1-x})_2$  by varying the alloy composition [57, 58, 59]. Unfortunately, there is very little work on the solid solution of these ternary

and quaternary chalcogenides [59, 3, 60, 61, 62, 63].

In this paper, we present the first-principles calculation of electronic structures, optical and bulk properties of tetragonal nonlinear optical crystals,  $AgGa(S_xSe_{1-x})_2$  ( $x=0.0, 0.25, 0.5, 0.75, \text{ and } 1.0$ ). We report the synthesis method of single crystals and measurements of the optical properties in each composition. The nonlinear coefficients of  $AgGa(S_xSe_{1-x})_2$  are also carried out to reveal the potential of these crystals in NLO applications. These calculations are compared with the experimental data and the literature values. Our analysis with band-by-band and atomic species projection technique not only yields useful information about material properties, but also provides deep insight into the fundamental understanding of the electronic structures and optical properties of tetragonal nonlinear optical crystals,  $AgGa(S_xSe_{1-x})_2$ .

## 1.4 The First Principles Calculation

In philosophy, a first principle is a basic, foundational proposition or assumption that cannot be deduced from any other proposition or as-

sumption. In mathematics, first principles are referred to as axioms or postulates. In condense matter physics, first principles simulation, a quatumn-machenics-based calculation scheme, is a powerful tool for searching materials with specified properties, satifying the requirements of the most modern technology. It can save lots of effort and cost when it is difficult to synthesize and investigate all kinds of compounds experimentally.

The first principles calculation is based on density functional theory (DFT) which is used in physics and chemistry to investigate the electronic structure (principally the ground state) of many-body systems, in particular atoms, molecules, and the condensed phases. With DFT theory, the properties of a many-electron system can be determined by using functionals, i.e. functions of another function, which in this case is the spatially dependent electron density. Hence the name density functional theory comes from the use of functionals of the electron density.

DFT has been very popular for calculations in solid state physics since

the 1970s. In many cases the results of DFT calculations for solid-state systems agreed quite satisfactorily with experimental data. Also, the computational costs were relatively low when compared to traditional ways which were based on the complicated many-electron wavefunction, such as Hartree-Fock theory and its descendants. However, DFT was not considered accurate enough for calculations in quantum chemistry until the 1990s, when the approximations used in the theory were greatly refined to better model the exchange and correlation interactions. DFT is now a leading method for electronic structure calculations in chemistry and solid-state physics. There are four of the most popular first principles calculation programs which are used in this thesis. They are Abinit,[64, 65] CASTEP[66, 67], WIEN2k,[41] and LASTO.[51, 52, 53, 54, 55]

The general flow chart of the first principles calculation scheme is shown in Fig. 1.5.

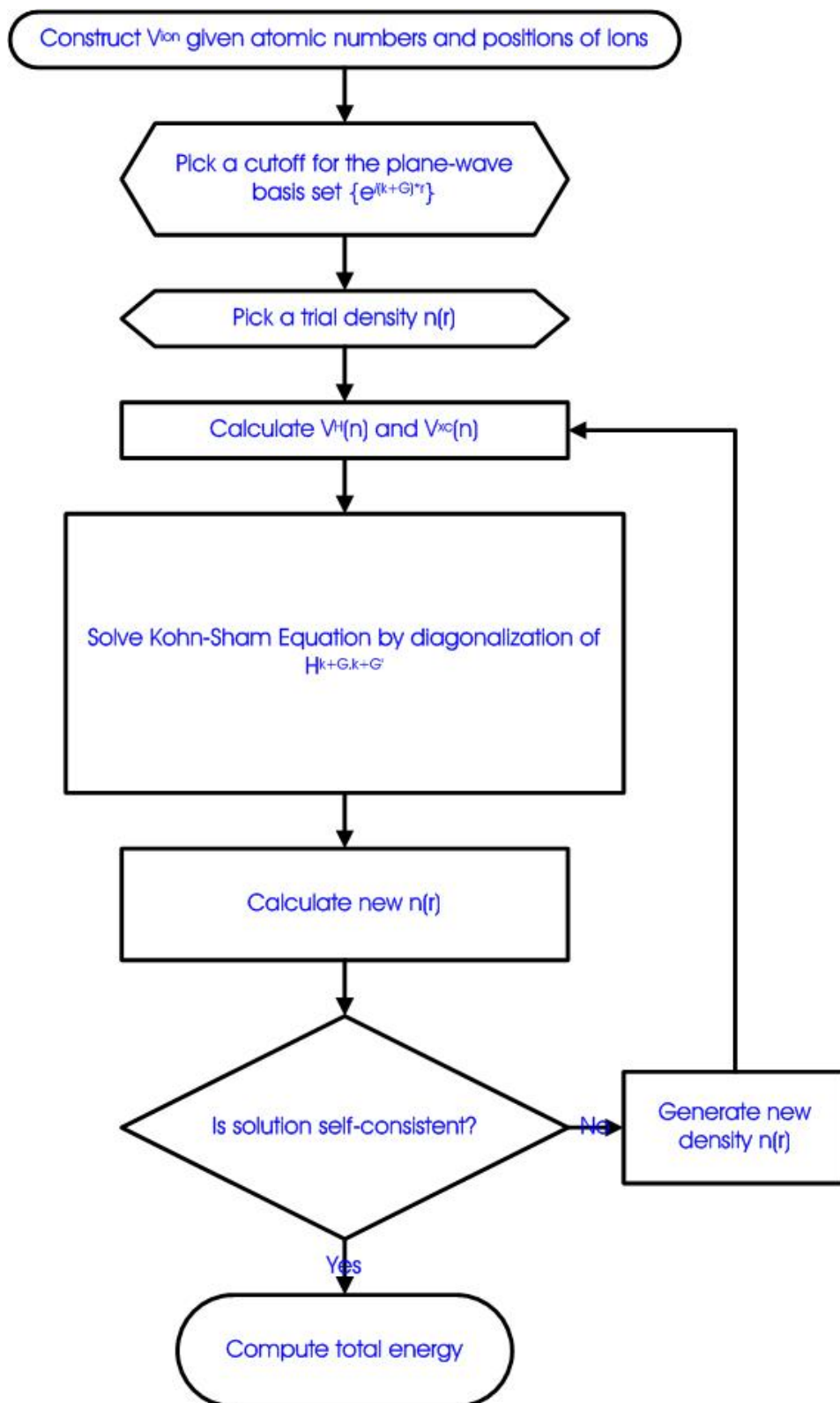


圖 1.5: Illustrations of the first-principles total energy minimization scheme.

## Chapter 2

# Methods for Simulations and Experiments

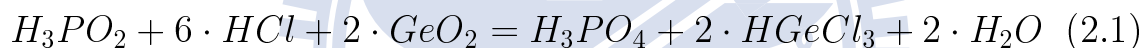


In this chapter, the studied methods, both experimental and theoretical ones, are proposed.

### 2.1 Synthesis

The synthetic procedure of ternary halides,  $ABX_3$ , is similar in Fig. 2.1, which is modified from the work of Gu and coworkers [22, 23, 24]. Chritensen *et al* [68] and Tananaev *et al* [69] used different synthesis

methods, but their methods were complex and the productivity was poor. We adopted the modified method for synthesizing  $\text{RbGeCl}_3 \cdot x(\text{H}_2\text{O})$ . 25 ml of 50%  $\text{H}_3\text{PO}_2$ , 25 ml of 37.5%  $\text{HCl}$  and 5 g of  $\text{GeO}_2$  were loaded into a 500 ml beaker, and then heated to  $85\text{-}90^\circ\text{C}$ . The solution was vigorously mixed for 5 h then cooled to room temperature. After removing the precipitate, 6.05 g  $\text{RbCl}$  was added and the temperature raised to the boiling point, then the mixture was cooled to room temperature again. A white precipitation was formed. The reaction equations are as follows:



and



Recrystallization is achieved via mixing the precipitation  $\text{RbGeCl}_3$  with 1 : 1 concentrated  $\text{HCl}$  and alcohol solution and we can obtain colorless  $\text{RbGeCl}_3 \cdot x(\text{H}_2\text{O})$  crystals. HRGC is synthesized by a similar procedure, as reported by Nyqvist *et al* [70]. The synthesis is carried out in an aqueous solution under normal condition. Analytical pure  $\text{RbCl}$  and  $\text{GeCl}_2$  (with mole ratio 1 : 1) were dissolved in a certain amount of hot distilled water, and colorless crystals were separated out during cooling.

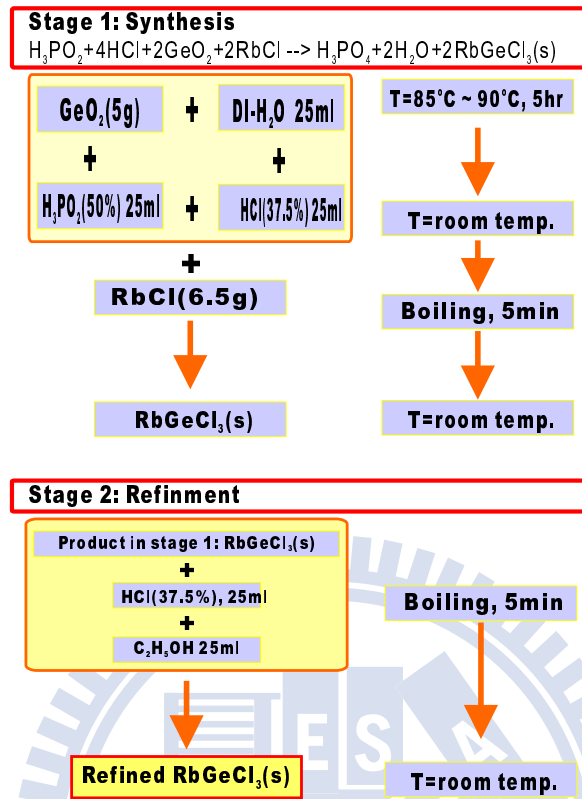


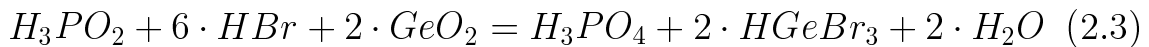
圖 2.1: The synthesis procedure of monoclinic nonlinear optical crystal HRGC.

Crystal is grown by utilizing a solvent slow evaporation technique in an aqueous solution. The size of the single crystal reached  $3 \times 2 \times 1 \text{ cm}^3$  (see Fig. 3.11).

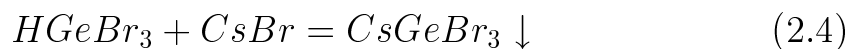


### 2.1.1 Synthesis and Structural Properties

The synthetic procedure of ternary halides,  $ABX_3$ , is similar to that of  $RbGeCl_3$  in Fig. 2.1, which was modified from the work done by Gu *et al* [22, 23, 24]. Chritensen and Tananaev *et al* [68, 69] used different synthesis methods, but their methods seemed complex and the productivity was poor. In this study, 50%  $H_3PO_2$  (25ml) was loaded with 43.5%  $HBr$  (25ml) and  $GeO_2$  (5.25g) into a 500ml beaker, and then heated to  $85^\circ C$ - $90^\circ C$ . The solution was vigorously mixed for 5 hours and then cooled to room temperature. After removing the precipitate,  $CsBr$  (10.72g) was added and the temperature raised to boiling, then the mixture was naturally cooled to room temperature again. A yellow precipitation, about 22.30g, was formed. The reaction equations were listed as follows:



then



Recrystalization was done by mixing the precipitation  $CsGeBr_3$  with 1 : 1 concentrated  $HBr$  and alcohol solution to give the yellow crystals  $CsGeBr_3$ . Rhombohedral  $CsGeBr_3$  crystal could be considered as a

highly distorted perovskite crystal structure, and is shown in Figure 1.1. The reported [27, 28, 29, 30, 31] lattice parameters of  $CsGeBr_3$  at room temperature were  $a = b = c = 5.635\text{\AA}$ ,  $\alpha = \beta = \gamma = 88.74^\circ$  with noncentrosymmetric rhombohedral space group  $R3m$  (No.160).

Rhombohedral  $CsGeBr_3$  crystal was synthesized and sieved into different particle-size in order to measure and analyze its structural and optical properties. The measured values of CGB, synthesized in this work and by using the XRD and Rietveld refinement, will also be compared with the reported and the first principles calculation results in Table 3.2. Positions of the constituents in the Rhombohedral NLO crystals  $CsGeBr_3$  could be easily generated.

## 2.2 X-ray diffraction

The X-ray single crystal structure analysis is used to confirm the structure of the product. A single crystal with dimensions of  $1.10 \times 0.80 \times 0.40 \text{ mm}^3$  is mounted on a Enraf-Nonius CAD4 diffractometer using a graphite-monochromated Cu  $K\alpha$  ( $\lambda=1.542 \text{ \AA}$ ) radiation. The data were

collected at room temperature using the  $\omega/2\theta$  scan mode and corrected for Lorentz and polarization effects as well as the absorption during data reduction using Enraf-Nonius Molen/VAX software.

Although the structure of HRGC has been reported[46, 47], we felt it important to determine the structure to better understand the SHG properties. Our data confirm that HRGC crystallizes in the noncentrosymmetric rhombohedral space group  $P2_1\bar{m}$  (No.11) with  $a=7.988 \text{ \AA}$ ,  $b=6.941 \text{ \AA}$ ,  $c=5.800 \text{ \AA}$ ,  $\alpha = \gamma = 90.0^\circ$ , and  $\beta = 106.34^\circ$ . The cell parameters estimated from the first-principles calculation based on the WIEN2k[41] package are  $a=8.375 \text{ \AA}$ ,  $b=7.141 \text{ \AA}$ ,  $c=5.918 \text{ \AA}$ ,  $\alpha = \gamma = 90.0^\circ$ , and  $\beta = 107.24^\circ$ , which compare well with the single-crystal data.

## 2.3 Single crystal growth by using the vertical Bridgmen furnace

To understand the nature of optical transitions and other relevant effects on the calculated optical properties, we grow the bulk crystals by using the Bridgman technique in a vertical furnace. All the starting reagents have a nominal purity of 99.999%. Particular attention is paid to the mole ratios between the starting reagents. Since vapor compositions and partial pressure of the gaseous species are unknown, the optimum conditions for high quality crystal growth are empirically found. X-ray diffraction (XRD) measurement is used to determine the lattice parameters of all the crystals. In addition, the crystals of certain orientation relative to crystallographic axes are cut into pellets and polished both sides for optical measurements.

## 2.4 Thermogravimetric measurements

The thermo-gravimetric analysis (TGA) measurement in static air was performed on a Shimadzu DT-40 at a scan rate of  $20^{\circ}\text{C}/\text{min}$ . By using DTA1700 high temperature analysis instrument, thermal properties were measured.

Thermogravimetry (TG, %) and derivative thermogravimetry (DTG, mg/min) were employed to characterize the thermal and structural behaviors of CGB. Thermogravimetric analysis was carried out, on polycrystalline  $\text{CsGeBr}_3$ , in air at a heating rate of  $5^{\circ}\text{C}/\text{min}$  to  $550^{\circ}\text{C}$  with a Seiko 320 TG/DTA (Thermogravimetry / Differential Thermal Analysis).

## 2.5 Second-order nonlinear optical measurements

Powder SHG measurements, which were reported by Chen *et al*[71], were performed on a modified Kurtz-NLO [72] system using 1064 nm light (Fig. 2.2). A continuum Minilite II laser, operating at 1 Hz, is

used for all measurements. The average energy of laser pulse is 3 mJ. Since the SHG efficiency of powders has been shown to depend strongly on particle size [72, 73], polycrystalline HRGC is ground and sieved (Newark Wire Cloth) into distinct particle size ranges,  $\leq 20 \mu\text{m}$ , 20 to 45  $\mu\text{m}$ , 45 to 63  $\mu\text{m}$ , 63 to 75  $\mu\text{m}$ , 75 to 90  $\mu\text{m}$ , 90 to 125  $\mu\text{m}$ , and 125 to 138  $\mu\text{m}$ . To make relevant comparison with known SHG materials, crystalline KDP is also ground and sieved into the same particle-size ranges. All of the powders were placed in separate capillary tubes. The SHG, i.e., 532nm green light, radiation is collected in reflection and detected by a photomultiplier tube (Oriel Instruments). To detect only the SHG light, a 532 nm narrow-ban-pass interference filter is attached to the tube. A digital oscilloscope (Tektronix TDS 302) is used to view the SHG signal. Considering a normally incident beam with wavelength  $\lambda$  on a crystal plate with thickness  $L$ , the total second-harmonic intensity can be expressed as [74]

$$I_{2\omega} = \frac{128\pi^5 d_{eff}^2 I_{\omega}^2 L^2}{n_{\omega}^2 n_{2\omega} \lambda_{2\omega}^2 c} \cdot \frac{\sin^2(\Delta k L/2)}{(\Delta k L/2)^2}, \quad (2.5)$$

where  $\Delta k = k(2\omega) - 2k(\omega)$ ,  $I_{\omega}$  is the intensity of the incident fundamental beam,  $n_{\omega}$ ,  $n_{2\omega}$ , and  $d_{eff}$  are the indices of refraction and the effective nonlinearity of the crystal plate. When the plate is made with

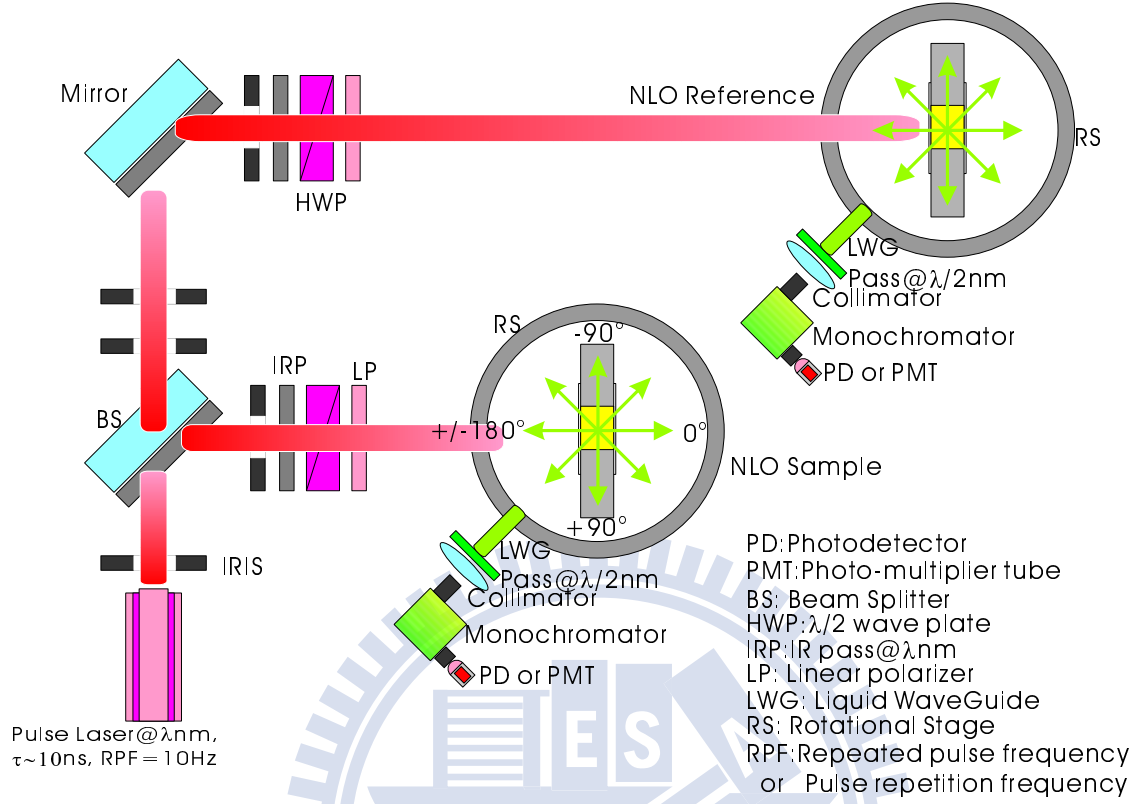


圖 2.2: Experimental setup used for measuring the second harmonic scattering pattern from a crystalline powder sample.

crystalline powders, the second-harmonic intensity becomes [75]

$$I_{2\omega} = \frac{512\pi^3 I_{\omega}^2 \bar{l}_c^2}{n_{\omega}^2 n_{2\omega} \lambda_{2\omega}^2 c} \cdot \langle d_{eff}^2 \rangle \cdot \frac{L}{r} \cdot \sin^2 \left[ \frac{\pi}{2} \left( \frac{\bar{r}}{\bar{l}_c} \right) \right]. \quad (2.6)$$

Here  $\bar{r}$  denotes the averaged particle size,

$$\bar{l}_c = \langle \lambda_{\omega} / 4(n_{2\omega} - n_{\omega}) \rangle \quad (2.7)$$

is the coherent length, and  $\langle d_{eff}^2 \rangle$ , the square of the effective nonlinearity averaged over the orientation distribution of crystalline powders.

When the second-harmonic generation is not phase matchable, eq. (2.6)

leads to the following asymptotic forms [75]:

$$I_{2\omega} \rightarrow \left\{ \begin{array}{l} \frac{256\pi^3 I_\omega^2 \bar{l}_c^2}{n_\omega^2 n_{2\omega} \lambda_{2\omega}^2 c} \cdot (L/\bar{r}) \cdot \langle d_{eff}^2 \rangle, \leftarrow \bar{r} \gg \bar{l}_c \\ \frac{128\pi^5 I_\omega^2}{n_\omega^2 n_{2\omega} \lambda_{2\omega}^2 c} \cdot L \cdot \bar{r} \langle d_{eff}^2 \rangle, \leftarrow \bar{r} \ll \bar{l}_c \end{array} \right\}. \quad (2.8)$$

If the second-harmonic generation satisfies the type-I phase matching condition, we can rewrite eq. (2.5) as [76]

$$I_{2\omega}(\bar{r}, \theta) = \frac{128\pi^5 I_\omega^2}{n_\omega^2 n_{2\omega} \lambda_{2\omega}^2 c} \cdot L \cdot \bar{r} \langle d_{eff}^2 \rangle \cdot \frac{\sin^2[\frac{\pi}{2} \frac{\bar{r}}{\bar{l}_{pm}} (\theta - \theta_{pm})]}{[\frac{\pi}{2} \frac{\bar{r}}{\bar{l}_{pm}} (\theta - \theta_{pm})]}, \quad (2.9)$$

where

$$\bar{l}_{pm} = \lambda / (4 |\Delta n_{B,2\omega}| \sin 2\theta_{pm}), \quad (2.10)$$

and  $\theta_{pm}$  is the phase matching angle. Here  $\Delta n_{B,2\omega} = n_{E,2\omega} - n_{O,2\omega}$  denotes the birefringence of material at the second-harmonic wavelength.

In the event that  $\bar{r} \gg \bar{l}_{pm}$  or  $\bar{r} \ll \bar{l}_{pm}$ , eq. (2.9) can be simplified to

$$I_{2\omega} \rightarrow \left\{ \begin{array}{l} \frac{256\pi^4 I_\omega^2}{n_\omega^2 n_{2\omega} \lambda_{2\omega}^2 c} \cdot L \cdot \bar{l}_{pm} \langle d_{eff}^2 \rangle, \leftarrow \bar{r} \gg \bar{l}_{pm} \\ \frac{128\pi^5 I_\omega^2}{n_\omega^2 n_{2\omega} \lambda_{2\omega}^2 c} \cdot L \cdot \bar{r} \langle d_{eff}^2 \rangle, \leftarrow \bar{r} \ll \bar{l}_{pm} \end{array} \right\}. \quad (2.11)$$

Chen *et al*[71] derived a useful empirical formula, which possesses the correct asymptotic forms in eq. (2.11), to depict the overall variation in second harmonic intensity with particle size  $\bar{r}$

$$I_{2\omega} = I_0 \sqrt{1 - \exp[-(\bar{r}/A)^2]} \quad (2.12)$$



with

$$I_0 = \frac{256\pi^4 I_\omega^2}{n_\omega^2 n_{2\omega} \lambda_{2\omega}^2 c} \cdot L \cdot \bar{l}_{pm} \langle d_{eff}^2 \rangle \quad (2.13)$$

and

$$A \approx 9 \cdot \bar{l}_{pm}. \quad (2.14)$$

An experimental arrangement for measuring the second harmonic scattering pattern from crystalline powders is described in Fig. 2.2. In this setup, a normally incident beam is shed on the sample cell. A liquid light guide with its input end attached to a rotation stage is employed to collect the second harmonic intensity at various scattering angles. We can integrate the second harmonic pattern over scattering angle to yield the total second harmonic intensity,  $I_{2\omega}$ . The second harmonic pattern over scattering angle to yield the total second harmonic intensity,  $I_{2\omega}$ , was integrated. The square of the effective nonlinearity,  $\langle d_{eff}^2 \rangle$ , averaged over the orientation distribution of crystalline powders of an unknown crystal, e.g., HRGC or CGB, was determined by

$$\begin{aligned} \langle d_{eff}^2 \rangle_{HRGC} &= \langle d_{eff}^2 \rangle_{KDP} \cdot \frac{I_{2\omega,HRGC}^{total} \cdot n_{\omega,HRGC}^2 \cdot n_{2\omega,HRGC}}{I_{2\omega,KDP}^{total} \cdot n_{\omega,KDP}^2 \cdot n_{2\omega,KDP}} \\ &\approx \langle d_{eff}^2 \rangle_{KDP} \cdot \frac{I_{2\omega,HRGC}^{total} \cdot n_{HRGC}^3}{I_{2\omega,KDP}^{total} \cdot n_{KDP}^3} \end{aligned} \quad (2.15)$$

with a reference NLO crystal, e.g. KDP, when  $n \approx n_\omega \approx n_{2\omega}$ .

## 2.6 Optical transmission measurements

Because wide transparent range is a crucial consideration for developing innovative NLO crystals used in IR range. The UV-vis electronic absorption spectra of HRGC were performed on a Hitachi 3400 UV-vis spectrophotometer. The infrared spectrum was recorded on a NICOLET 170SX FT-IR (Fourier-transform infrared) spectrophotometer with KBr pellet from 4000 to 400  $\text{cm}^{-1}$ . The HRGC transparent spectrum measurement was prepared by using HRGC solvent and HRGC as a pressed powder tablet. Then, the far-IR limitation of HRGC was detected by its Raman peaks.

The samples with parallel opposite faces are located inside a vacuum cryostat, cooled by liquid nitrogen. Optical transmission spectra are recorded from visible to mid-IR. Besides, the form of the fundamental absorption edge and photoluminescence spectra are analyzed and the band gap energy,  $E_g$ , is measured. The long-wave length transmission spectra is also determined by Fourier transformed infrared (FTIR) measurements.

## 2.7 The first principles calculations

The first principles, i.e. *ab initio*, calculations optimized cell parameters were compared with the experimental data. The first principles calculations were performed by using plane-wave-pseudopotential approach within the framework of density-functional theory (DFT) implemented in CASTEP software [66, 67]. The summation over the Brillouin zone (BZ) was carried out with a special k-point sampling using Monkhorst-Pack grid [77].

In order to save computation time, the special k-point set was reduced to 8-k points ( $3 \times 3 \times 3$  mesh) for the calculation of the equilibrium lattice constants and mechanical properties. The equilibrium lattice constants and fractional atomic coordinates were deduced from the total-energy minimization. Relaxation of the lattice parameters and atomic positions was carried out under the constraint of the unit cell space-group symmetry.

### 2.7.1 Computational Schemes

In order to gain the intrinsic understanding of optoelectronic materials, first principles simulation with various programs has been employed in this study. (see Fig. 2.3) From first principles calculations, many guidelines and designing indicator can be carried out.

The structural parameters are determined by using both the pseudopotential plane waves method (CASTEP package)[66, 67] and the full-potential linearized augmented plane wave (*FLAPW*) method (WIEN2K package).[41] In order to save computation time, 8 special k-points in the irreducible segment of the Brillouin zone ( $10 \times 10 \times 10$  mesh) were used for the calculation of the equilibrium lattice constants and mechanical properties. Using a larger set of k-points was found to lead to about only 1% difference in the equilibrium lattice constants.

The obtained lattice parameters were used to calculate the electronic properties of  $A^{II}B^{IV}N_2$ . In order to understand the nature of optical

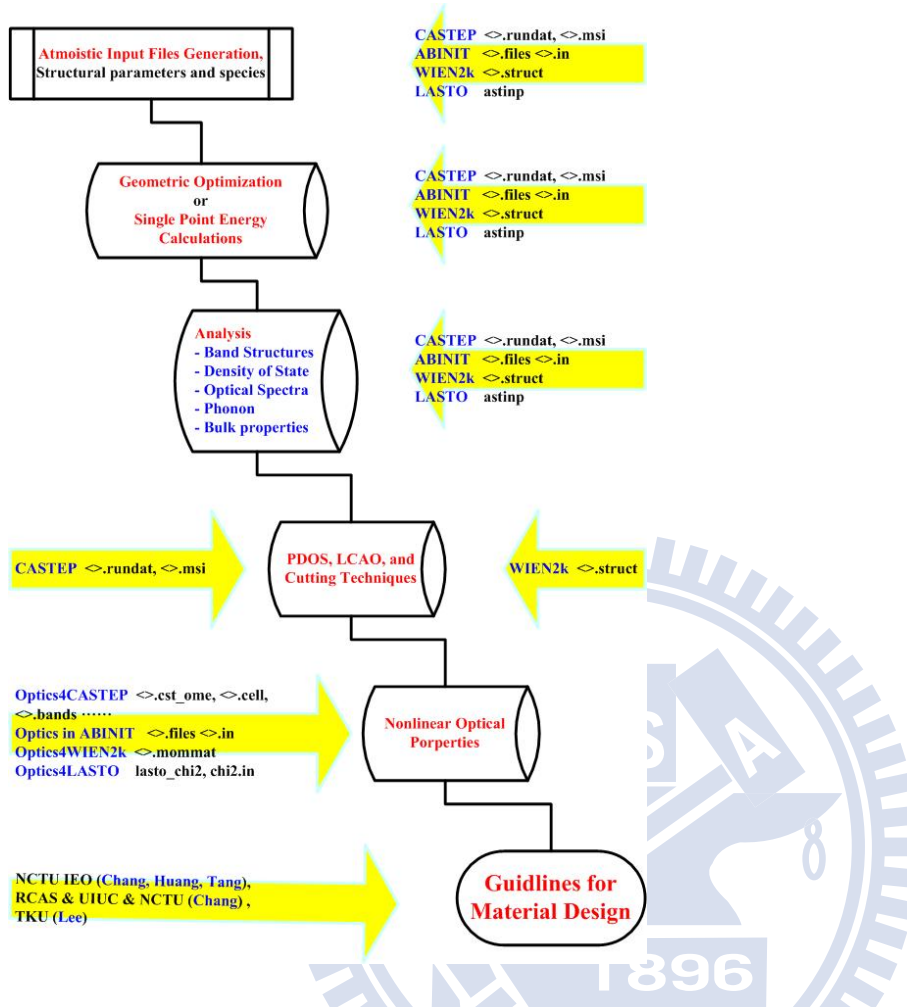


圖 2.3: Flow chart of optoelectronic material design from first principles Calculations transitions and other relevant effects on the calculated optical properties, an analysis of the local densities of states and other electronic properties of these  $A^{II}B^{IV}N_2$  crystals were made. It was useful for extracting the local (atomic) information of the materials. Those radial pseudo atomic wave functions were the ones used to generate pseudopotentials and therefore, had the best consistency with the solved Bloch states. The projected values were equivalent to the coefficients

of LCAO (Linear Combination of Atomic Orbitals) type expansion of original Bloch states using pseudo atomic orbitals as basis functions. The collection of those coefficients can be extracted local information from the system as a whole, where in the present work it is the PDOS (Partial or Projected Density of States) plots being used as an analysis tool.

The analytic expressions for the nonlinear response functions are based on the formalism of Sipe and Ghahramani, [45] as extended and developed in the length gauge by Aversa and Sipe; [78] the response calculation is at the level of the independent particle approximation. This approach has the advantage that the response coefficients are inherently free of any unphysical divergences at zero frequency, a consequence of a careful treatment and separation of interband and intraband transitions. 'Sum rules' are not required to eliminate artificial divergences. The recent work of Dal Corso and Mauri, [79] based on an elegant Wannier function approach, is also free of such divergences.

The full band structure calculation in this work utilized the norm-conserving pseudo-potential plane wave within the local density approx-

imation (LDA). This first-principles method is more reliable than the empirical method employed by Moss and co-workers [80, 81, 82, 83, 84]. Huang and Ching [85, 86, 87] neglect the 'scissors' modification in the matrix elements; based on the evidence, [88] and the results of our own calculations, this does not much influence on the tendency in the determination of the response functions. The local field effects was not included in this work. As suggested by the work of Levine and Allan, [88] significant corrections for the materials considered here at the level of second-order response are expected. However, the inclusion of local field effects can be done in a straightforward way within our formalism.

### 2.7.2 Calculation details for $\text{AgGa}(\text{S}_x\text{Se}_{1-x})_2$

The crystal structure of the tetragonal chalcopyrite,  $\text{AgGaS}_2$  or  $\text{AgGaSe}_2$ , is shown in Fig. 2.4. The unit cell exhibits  $I-42d$  symmetry ( $a = b \neq c$ ,  $\alpha = \beta = \gamma = 90^\circ$ )[46, 47], which can be considered as a superstructure of two zinc-blende structures. Four metal atoms  $\text{Ag}$ ,  $\text{Ga}$ , and eight crystallographically equivalent  $\text{S}$  or  $\text{Se}$  atoms occupy the positions  $[(x, y, z); (\bar{x}, \bar{y}, \bar{z}); (y, \bar{x}, \bar{z}); (\bar{y}, x, \bar{z}); (\bar{x} + 1/2, y, \bar{z} + 3/4); (x + 1/2, \bar{y}, \bar{z} + 3/4);$

$(\bar{y} + 1/2, \bar{x}, z + 3/4); (y + 1/2, x, z + 3/4)]$ . In  $AgGa(S_xSe_{1-x})_2$  crystals, metal atoms are tetrahedrally coordinated by  $S$  or  $Se$  and vice versa. The calculations are performed by using *ab initio* plane-wave-pseudopotential approach within the framework of density-functional theory (DFT) implemented in CASTEP software[66]. We assemble the supercell of  $AgGaS_2$  by enlarging a-direction and b-direction twice ( $2 \times 2 \times 1$ ), and then fractionally ( $x=0.00, 0.25, 0.5, 0.75, \text{ and } 1.0$ ) substitute atoms by atoms. The summation over the Brillouin zone (BZ) is carried out with a special k-point sampling using Monkhorst-Pack grid[77]). A kinetic-energy cutoff of 580 eV, 4-k special points and 96 bands are used to ensure the convergence in the calculation of the optical properties. In order to save computation time, we reduce special k-point set to 8-k points ( $3 \times 3 \times 3$  mesh) for the calculation of the equilibrium lattice constants and mechanical properties. We find that the smaller set of k-points causes only less than 2 percent difference in the equilibrium lattice constants. For comparison, we also build up a non-supercell model ( $1 \times 1 \times 1$ ), hereafter named the single-unit-cell-model) with the same fractional substitution and perform the similar calculation as those with the supercell models. In our *ab initio* calculation, we choose both the 3-electron shallow-core pseudopotential in the



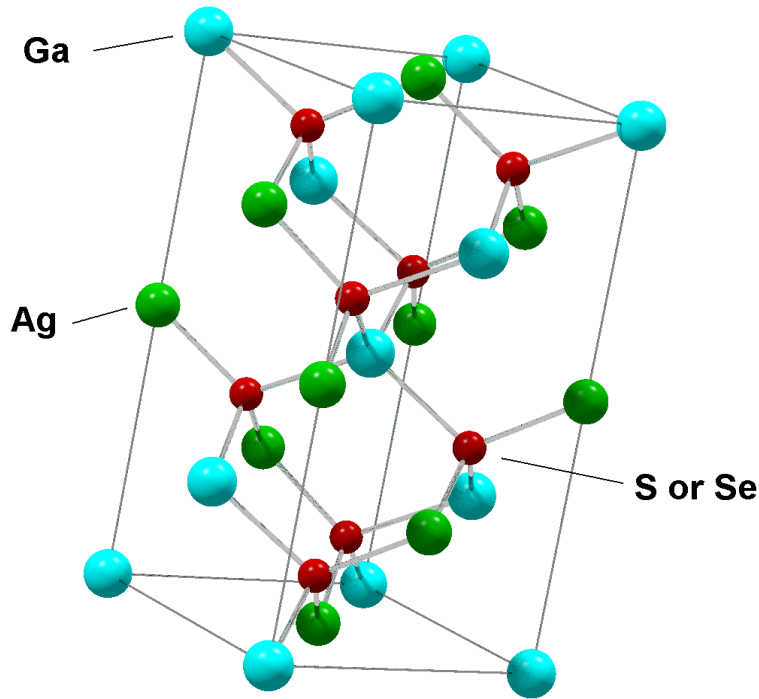


圖 2.4: The crystal structure of tetragonal chalcopyrite

supercell-model and the 13-electron shallow-core pseudopotential in single unit-cell-model for gallium series to take into account the noticeable hybridization between (3)d-shell and (4)p-shell electrons.[89, 90, 91] We use the obtained lattice parameters to calculate the electronic properties of  $AgGa(S_xSe_{1-x})_2$  by proportionally substituting  $S$  and  $Se$  into the supercell and the single-unit-cell-model. In order to understand the nature of optical transitions and other relevant effects on the calculated optical properties, we analyze the local densities of states and other electronic properties of these  $AgGa(S_xSe_{1-x})_2$  crystals.

### 2.7.3 Calculations of structural properties

The equilibrium lattice constants and fractional atomic coordinates are deduced from the total-energy minimization. We carry out the relaxation of the lattice parameters and atomic positions under the constraint of the unit cell space-group symmetry. Energy-volume relations are obtained by varying unit-cell volume and the results were fitted to the Murnaghan equation of state[92] The mechanical properties, e.g. bulk modulus, are determined by the Equation of state:[?]

$$E(V) = E_0 + \frac{B_0 V}{B'_0} \left( \frac{(V_0/V)^{B'_0}}{B'_0 - 1} + 1 \right) - \frac{B_0 V_0}{B'_0 - 1}$$

$$P(V) = \frac{B_0}{B'_0} \left( \left( \frac{V_0}{V} \right)^{B'_0} - 1 \right) \quad (2.16)$$

and the modified Equation of state:[93]

$$E(V) = E_0 + \frac{9V_0 B_0}{16} \left\{ \left[ \left( \frac{V_0}{V} \right)^{\frac{2}{3}} - 1 \right]^3 B'_0 + \left[ \left( \frac{V_0}{V} \right)^{\frac{2}{3}} - 1 \right]^2 \left[ 6 - 4 \left( \frac{V_0}{V} \right)^{\frac{2}{3}} \right] \right\}$$

$$P(V) = \frac{3B_0}{2} \left[ \left( \frac{V_0}{V} \right)^{\frac{7}{3}} - \left( \frac{V_0}{V} \right)^{\frac{5}{3}} \right] \left\{ 1 + \frac{3}{4} (B'_0 - 4) \left[ \left( \frac{V_0}{V} \right)^{\frac{2}{3}} - 1 \right] \right\} \quad (2.17)$$

Firstly, the equilibrium lattice constants and fractional atomic coordinates are determined from procedure of the total-energy minimization.

We carry out the relaxation of the lattice parameters and atomic positions under a constraint of the fixed space-group symmetry. Energy-volume relations are obtained by varying unit-cell volumes and the results were fitted to the Murnaghan equation of state. From the fit, an estimate of the static bulk modulus at zero pressure, and the first-order pressure derivative of the bulk modulus can be obtained. Two types of distortion in the chalcopyrite structure which mentioned in the chapter 1.3 with respect to the zincblende cubic structure [48, 49, 50] are also discussed later.

Our computer simulations include analysis and optimization of atomic arrangement in the crystals under consideration and predictions of their electronic and optical properties. The atomic arrangements were determined by using the WIEN2K package.[41]

#### 2.7.4 Calculations of electronic properties

Secondly, we use the obtained lattice parameters to calculate the electronic properties. In order to understand the nature of optical transitions and other relevant effects on the calculated optical properties, we study the local densities of states and other electronic properties of these crystals.

#### 2.7.5 The Linear Combination of Atomic Orbital Method

In order to determine the optical response functions in a full band structure approach, one requires the eigenvalues and velocity matrix elements at many  $\mathbf{k}$  points in the Brillouin zone (BZ). The velocity matrix elements, in turn, require a knowledge of the electronic wave functions. For this purpose, we employ a first-principles approach in the form of the linear combination of atomic orbitals (LCAO) method. As this method has been previously discussed,[94, 95] we highlight only a few of its pertinent features.

Let  $\Psi_{nk}(\vec{r})$  be the self-consistent wave function of the crystal at the  $n$ -th band and  $k$ -th point in the Brillouin-Zone (BZ).  $\Psi_{nk}(\vec{r})$  can be decomposed into a linear combination of the atomic orbitals  $\Phi_{lm}^{(i)}(\vec{r})$  of  $i$ -th atom by

$$\Psi_{nk}(\vec{r}) = \sum_{i \in (\text{atoms})} \sum_l \sum_{m=-l}^{m=+l} C_{nk,lm}^{(i)} \Phi_{lm}^{(i)}(\vec{r}) \quad (2.18)$$

where  $C_{nk,lm}^{(i)} = \int_{V_o} \Psi_{nk}(\vec{r}) \cdot \Phi_{lm}^{(i)*}(\vec{r}) dV$  denotes the projection coefficients.

The  $l$ -th orbital of the  $\beta$ -species contributes to the population by a fraction of  $h_{nk,l}^{(\beta)}$  [96]

$$h_{nk,l}^{(\beta)} = \sum_{i \in (\beta)} \sum_{m=-l}^{m=+l} C_{nk,lm}^{(i)} C_{nk,lm}^{(i)*} / \sum_{i \in (\beta, \beta, \gamma, \dots)} \sum_l \sum_{m=-l}^{m=+l} C_{nk,lm}^{(i)} C_{nk,lm}^{(i)*}. \quad (2.19)$$

By using the planewave basis set in planewave pseudopotential (PPP) scheme, the representation of natural atomic orbitals around the centers of atoms is missing. However, this disadvantage could be overcome by projecting the Bloch states onto the atomic orbitals constructed using the radial pseudo atomic wavefunctions of each angular momentum channels for each elements (the angular parts are simply spherical harmonic functions) [97, 98]. It is useful for extracting the local (atomic) information of the materials. Those radial pseudo atomic wavefunctions are the ones used to generate pseudopotentials and therefore, had

the best consistency with the Bloch states. The projected values are equivalent to the coefficients of LCAO (Linear Combination of Atomic Orbitals) type expansion of original Bloch states using pseudo atomic orbitals as basis functions. The collection of those coefficients can be used to extract local information from the system as a whole, where in the present work it is the PDOS (Partial or Projected Density of States) plots been used as an analysis tool. This atomic projection concept is then employed for resolving interesting components from the total density of states (TDOS)

$$PDOS(\beta, l, E) = \sum_n \sum_k h_{nk,l}^{(\beta)} \delta(E - E_{nk}) \quad (2.20)$$

The partial density states (PDOS) could be used to provide valuable insight into the formation of energy bandgap and the nature of transitions from which the linear and nonlinear optical properties are originated.

The atomic projection concept was then employed for resolving interesting components from total density of states (DOS). We define the local density of states (LDOS) and projected density states (PDOS) as

$$LDOS(\alpha, E) = \sum_n \sum_k \sum_l h_{nk,l}^{(\alpha)} \delta(E - E_{nk}) \quad (2.21)$$

and

$$PDOS(\alpha, l, E) = \sum_n \sum_k h_{nk,l}^{(\alpha)} \delta(E - E_{nk}) \quad (2.22)$$

which can provide valuable insight into the nature of transitions from which the linear and nonlinear optical properties were originated. The  $l$ -th orbital of the  $\beta$ -species contributes to eigenfunctions by a fraction,  $h_{nk,l}^{(\beta)}$  [96], defined as eq. 2.19. We calculate PDOS by using the WIEN2K package. [41]

### 2.7.6 Optical response functions

In a crystalline solid, the most important optical transitions did not change the momentum or the spin of the electrons involved in the transition. In terms of an energy band structure this means that one only has to consider optical excitations from an occupied state of the same spin for each  $k$  vector in the BZ.

The linear optical properties of a dielectric crystalline material can therefore be described with a dielectric function of  $\epsilon_{ij}(\vec{q}, \omega)$  at  $\vec{q}=0$ .

When the incident photon energy is higher than the bandgap  $E_G$ , the material can attenuate the photon flux. The absorption coefficient  $\alpha_{ij}(\omega)$  is related to the imaginary part of the dielectric function by [99]

$$\begin{aligned} \text{Im}\epsilon_{ij}(\omega) &= \frac{\lambda n(\omega)}{2\pi} \alpha_{ij}(\omega) \\ &= \frac{8\pi^2 \hbar^2 e^2}{m^2 V} \sum_k \sum_{cv} (f_c - f_v) \frac{p_{cv}^i(k) p_{cv}^j(k)}{E_{vc}^2} \delta(E_{cv}(k) - \hbar\omega). \end{aligned} \quad (2.23)$$

Here  $f_c$  and  $f_v$  represented the Fermi distribution of the conduction band  $c$  and the valence band  $v$ , respectively;  $p_{cv}^i(k, \text{\AA}^{-1})$  denoted the momentum matrix element (MME, in unit of  $\text{\AA}^{-1}$ ) from the conduction band  $c$  to the valence band  $v$  at the  $k$  point of the BZ. The real part of the dielectric function is obtained from the imaginary part with the Kramer-Kronig transformation. For the second-order nonlinear optical (NLO) response, the theoretical description is very complex [99]. However, at the zero frequency limits, the NLO susceptibility can be expressed as

$$\begin{aligned} \chi_{ijk}^{(2)}(0) &= \frac{1}{V} \left(\frac{e\hbar}{m}\right)^3 \sum_k \sum_{vc} \left[ \sum_{c'} \frac{1}{E_{c'c} E_{cv}^2 E_{c'v}^2} (D_{vc'c}^{ijk} + D_{cvc'}^{ijk} + D_{c'cv}^{ijk}) - \right. \\ &\quad \left. \sum_{v'} \frac{1}{E_{vv'} E_{cv}^2 E_{c'v}^2} (D_{v'cv}^{ijk} + D_{vv'c}^{ijk} + D_{c'vv'}^{ijk}) \right] \end{aligned} \quad (2.24)$$

where  $D_{nml}^{ijk} = \text{Im}[p_{nm}^i (p_{ml}^j p_{ln}^k + p_{ml}^k p_{ln}^j)]/2$ . Decomposing  $\chi_{ijk}^{(2)}(0)$  into various contributions from atomic species or orbitals are of interest



here. This can be properly done by calculating the contribution from the  $\beta$ -th species as [100]

$$\begin{aligned} \chi_{ijk}^{(2)}(\beta, E) = & \frac{1}{V} \left( \frac{e\hbar}{m} \right)^3 \sum_l \sum_k \sum_{vc} [h_{vk,l}^{(\beta)} \delta(E - E_{vk}) + h_{ck,l}^{(\beta)} \delta(E - E_{ck})] \\ & \times \left[ \sum_{c'} \frac{(D_{vc'c}^{ijk} + D_{cv'c'}^{ijk} + D_{c'cv}^{ijk})}{E_{c'c} E_{cv}^2 E_{c'v}^2} - \sum_{v'} \frac{(D_{v'cv}^{ijk} + D_{vv'e}^{ijk} + D_{c'v'}^{ijk})}{E_{vv'} E_{cv}^2 E_{c'v}^2} \right] \end{aligned} \quad (2.25)$$

Equation 2.25 is very similar to eq. 2.22 except that the second-order nonlinear optical strengths served as the weighting factor. We shall use this equation to obtain insight into the underlying mechanism of the NLO susceptibility. In Chap. 3.4 the calculated and the experimental results will be compared and discussed.

Tang *et al* used the same approach in both local-density approximation (LDA) and generalized-gradient approximation (GGA) with norm-conserving pseudopotentials to investigate the electronic structures, optical and bulk properties of the rhombohedral ternary halides [12] and the orthorhombic ternary nitrides [43]. The analysis with band-by-band and atomic species projection technique [12, 43] both yielded useful information about material properties and provided deep insight into the fundamental understanding of the electronic structures and optical

properties of rhombohedral nonlinear optical crystals, CsGeX<sub>3</sub> (X=Cl, Br, and I).

### 2.7.7 Frequency-dependent Optical Properties

For the linear susceptibility, we adopt the analytic expression given by[45]

$$\tilde{\chi}_I^{ab}(-\omega; \omega) = \frac{e^2}{\Omega \hbar} \sum_{nm\mathbf{k}} f_{nm} \frac{r_{nm}^a(\mathbf{k}) r_{mn}^b(\mathbf{k})}{[\omega_{nm}(\mathbf{k}) + (\Delta/\hbar)(\delta_{mc} - \delta_{nc}) - \omega]}, \quad (2.26)$$

where  $n$  and  $m$  label energy bands;  $f_{mn} \equiv f_m - f_n$ , with  $f_i$  the Fermi occupation factor.  $\mathbf{k}$  denote the wave vectors in the Brillouin zone.  $\omega_{mn}(k) \equiv \omega_m(k) - \omega_n(k)$  denote the frequency differences.  $r_{mn}$  are the dipole matrix elements, which are related to the velocity matrix elements,  $v_{mn}$  via  $r_{mn} = v_{mn}/(i\omega_{nm})$ .  $\Delta$  denotes the constant shift used in the 'scissors approximation' to correct the energy band gap difference caused by the local density approximation.  $\delta_{mc} = 1$  if band  $m$  denotes one of the conduction bands.

For the second-order response we write[45]

$$\begin{aligned} \chi_{abc}^{(2)}(-\omega_\beta - \omega_\gamma; \omega_\beta, \omega_\gamma) = & \chi_{abc,II}^{(2)}(-\omega_\beta - \omega_\gamma; \omega_\beta, \omega_\gamma) \\ & + \eta_{abc,II}(-\omega_\beta - \omega_\gamma; \omega_\beta, \omega_\gamma) + \frac{i}{(\omega_\beta + \omega_\gamma)} \end{aligned} \quad (2.27)$$

$$\text{sigma}_{abc,II}(-\omega_\beta - \omega_\gamma; \omega_\beta, \omega_\gamma), \quad (2.28)$$

where  $\chi_{abc,II}^{(2)}$  represents the purely interband contribution.  $\eta_{abc,II}$  describes the contribution from the modulation of the linear susceptibility by the intraband motion of the electrons. The third term is due to the modification of the intraband motion by the polarization energy associated with the interband transition. Explicit expressions for  $\chi_{abc}^{(2)}(-2\omega : -\omega, -\omega)$  and  $\chi_{abc}^{(2)}(-\omega : -\omega, 0)$  can be found in Appendix B of Ref. [45]. To include the 'scissors operator' effect, we simply replace  $\omega_{nm}(\mathbf{k})$  in these expressions by  $\omega_{nm}(\mathbf{k}) + (\Delta/\hbar)(\delta_{mc} - \delta_{nc})$ .

### 2.7.8 Second-Order Nonlinear Susceptibilities

For the second-order nonlinear optical (NLO) response, the theoretical description by Raskheev *et al.* [99] was very complex. However, at the zero frequency limits, the NLO susceptibility could be expressed as

[43, 16]

$$\chi_{ijk}^{(2)}(0) = \frac{1}{V} \left(\frac{e\hbar}{m}\right)^3 \sum_k \sum_{vc} \left[ \sum_{c'} \frac{1}{E_{c'e} E_{cv}^2 E_{c'v}^2} (D_{vc'e}^{ijk} + D_{cv'e}^{ijk} + D_{c'ev}^{ijk}) - \sum_{v'} \frac{1}{E_{vv'} E_{cv}^2 E_{c'v}^2} (D_{v'cv}^{ijk} + D_{vv'c}^{ijk} + D_{c'vv'}^{ijk}) \right] \quad (2.29)$$

where  $D_{nml}^{ijk} = \text{Im}[p_{nm}^i (p_{ml}^j p_{ln}^k + p_{ml}^k p_{ln}^j)]/2$ . Here  $p_{cv}^i(k, \text{\AA}^{-1})$  denoted the momentum matrix element (MME) from the conduction band  $c$  to the valence band  $v$  at the  $k$ -point of BZ. For the photon energy  $\hbar\omega$  of PSHG measurement well below the band-gap, 2.32eV, frequency-dependent  $\chi_{ijk}^{(2)}(-2\omega; \omega, \omega)$  and  $n(\omega)$  were nearly constants in this frequency region [2, 71]. The static  $\chi_{ijk}^{(2)}(0)$  could be considered as good approximation to the frequency-dependent  $\chi_{ijk}^{(2)}(-2\omega; \omega, \omega)$  in the PSHG measurements.

Tang *et al* used the same approach by using both local-density approximation (LDA) and generalized-gradient approximation (GGA) with norm-conserving pseudopotentials to investigate the electronic structures, optical and bulk properties of the rhombohedral ternary halides [12] and the orthorhombic ternary nitrides [43]. The analysis with band-by-band and atomic species projection technique [12, 43] both yielded useful information about material properties and provided deep insight into the fundamental understanding of the electronic structures and

optical properties of rhombohedral nonlinear optical crystals,  $CsGeX_3$  (X=Cl, Br, and I). A kinetic-energy cutoff of 580 eV, 4-k special points and 54 bands were used to ensure the convergence in the calculation of the optical properties.

Various representative calculations of nonlinear bulk susceptibilities which adopt the summations-over-excited states (SOS) scheme were discussed in the review paper of B. Champagne and D. M. Bishop [101]. The models and calculating schemes employed in first principles calculations progressed in parallel to the development of *ab initio* band structure calculation. However, first principles calculations in this paper did not employ any band-gap correction scheme at all for two reasons. First, the effected tendencies with structural distortion and the constituents were focused in this study. Second, the calculated results of  $\chi_{ijk}^{(2)}(-2\omega; \omega, \omega)$  were still diversified after various band-gap correction schemes were employed. The scissors operator approximation, one of the band-gap correction schemes, was good enough. However, in this study, we focused on the structural and the constituent effect on the NLO susceptibilities, and there was no any band-gap correction scheme

will be implemented, discussed, and developed.

In Chap. 3.4 the calculated and the experimental results will be compared and discussed.



## Chapter 3

# Innovative Non-linear Optical Material: the Ternary Halides

The first principles calculation of frequency-dependent linear optical susceptibilities and electronic band structures of CGX rhombohedral nonlinear optical crystals,  $CsGeX_3$  (X=Cl, Br, and I) were performed by using the WIEN2k package. The maximum difference between calculated and measured lattice parameters were less than 1.1%, and this accurate result could almost guarantee the *ab initio* calculated properties of linear electro-optics (LEO) on CGX. However, our first principles calculations indicate that the optimized cell angles of  $CsGeX_3$  are more

distorted from cubic structure than the experimental results. (see Table 3.1)

### 3.1 Structures of Rhombohedral, Cubic, and Tetragonal Ternary Halides

The CGX crystals tend to extend along one of the  $\langle 111 \rangle$  directions. The calculated electronic band structures of rhombohedral CGX were behaved similarly. The CGX crystals tend to extend along one of the  $\langle 111 \rangle$  directions. The calculated electronic band structures of rhombohedral CGX were behaved similarly.

The structural distortion factors obtained from experimental and the WIEN2k calculations are listed in Table 3.1. According to Table. 3.1,  $\Delta\alpha$  and  $d_{Ge}$  increase with increasing atomic weight while  $d_X$  and  $t_G$  decrease with increasing atomic weight. The geometrically optimized cell parameters and distortion factors are listed below the experimental ones in Table 3.2 and Table 3.1, respectively. Similar to the experimen-



tal results, the calculated  $\Delta\alpha$  and  $d_{Ge}$  increase with increasing atomic weight, i.e.  $\Delta\alpha^{CGC} < \Delta\alpha^{CGB} < \Delta\alpha^{CGI}$  and  $d_{Ge}^{CGC} < d_{Ge}^{CGB} < d_{Ge}^{CGI}$ . On the other hand, the calculated  $d_X$  decreases with increasing atomic weight. (see Table. 3.1)

The magnitudes of experimental distortional factors in Table 3.1 can be simplified as some integer ratios. The experimental lattice angles of CGX have the ratios like  $\Delta\alpha_{exp}^{CGC} : \Delta\alpha_{exp}^{CGB} : \Delta\alpha_{exp}^{CGI} \approx 3 : 14 : 16$ , and the calculated results are like  $\Delta\alpha_{cal}^{CGC} : \Delta\alpha_{cal}^{CGB} : \Delta\alpha_{cal}^{CGI} \approx 1 : 2 : 3$ . Additionally, the experimentally measured displacements of B-site cation, Ge, are  $d_{Ge,exp}^{CGC} : d_{Ge,exp}^{CGB} : d_{Ge,exp}^{CGI} \approx 3 : 4 : 5$ , while the calculated results are like  $d_{Ge,cal}^{CGC} : d_{Ge,cal}^{CGB} : d_{Ge,cal}^{CGI} \approx 4 : 6 : 7$ . Finally, the experimentally measured displacements of anion, X, are  $d_{X,exp}^{CGC} : d_{X,exp}^{CGB} : d_{X,exp}^{CGI} \approx 4 : 2 : 1$ , and the calculated results are also  $d_{X,cal}^{CGC} : d_{X,cal}^{CGB} : d_{X,cal}^{CGI} \approx 4 : 2 : 1$ .

The effects of these integer ratios on the electronic and optical properties are discussed in the following chapters.

The results obtained by volume optimization with WIEN2K[41] are shown

表 3.1: Distorted structural factors obtained from the experimental lattice constants and the First-Principles results of the Rhombohedral NLO crystals  $CsGeX_3$ .

	$\Delta\alpha$	$d_{Ge}$	$d_X$
<i>CGC</i> (exp.)	3.077(7)	1.90	5.390(6)
<i>CGB</i> (exp.)	13.955(5)	2.36	2.721(9)
<i>CGI</i> (exp.)	15.555(5)	2.97	1.258(6)
<i>CGC</i> (calc.)	9.766(6)	2.01	5.866(7)
<i>CGB</i> (calc.)	18.922(2)	3.00	3.189(5)
<i>CGI</i> (calc.)	26.055(5)	3.54	1.407(7)

in Fig. 3.2, and the bulk modulus of the different phases of  $CGX$  are also listed in Table 3.3. The summation over the Brillouin zone (BZ) was carried out with a  $10 \times 10 \times 10$  Monkhorst-Pack  $\mathbf{k}$  mesh [77]. The maximum difference between calculated and measured lattice parameters were less than 1.1%, and this accurate result could almost guarantee the *ab initio* calculated properties of linear electro-optics (LEO) on  $CGX$ . However, our first principles calculations indicate that the optimized cell angles of  $CsGeX_3$  are distorted from cubic structure more than the experimental results. (see Table 3.1)

### 3.1.1 X-ray diffraction

Although the structure of  $CsGeBr_3$  has been reported, we felt it important to determine the structure to better understand the SHG properties. The synthesized yellow crystals  $CsGeBr_3$  were crushed, ground, and sieved. X-ray diffractograms were obtained at room temperature by means of  $Cu - K\alpha$  radiation with Siemens D5000 equipment. For determination of the lattice parameters, extra  $CsBr$  crystal was used as an internal standard. Measured pattern was indexed and analyzed, i.e. the full-profile Rietveld refinement, by a non-profit program *PowderCell* [102], which was developed by W Kraus and G Nolze. The structural parameters of  $CsGeBr_3$ , which were reported JCPDS [27, 28, 29, 30, 31], are listed in Table 3.2, for comparison.

### 3.1.2 Crystal structure and mechanical properties

Figure 3.1 shows the X-ray powder diffraction of the crystal HRGC. Each important peak has been labeled on the measured X-ray diffraction (XRD) patterns, e.g. the [111] plane around  $2\theta \approx 20.78^\circ$  or [310] plane about  $2\theta \approx 37.40^\circ$ . These peaks are slightly shifted from ideal

表 3.2: Lattice constants and the *Ge*'s fractional coordinates of the Rhombohedral NLO crystals *CsGeBr<sub>3</sub>* and *CsGeCl<sub>3</sub>*. The first principles calculation results and the measured values by using the XRD and Rietveld refinement were compared.

	$a(=b=c)$	$\alpha(=\beta=\gamma)$	Frac. Coord. of <i>Ge</i>	$t_G$
<i>CsGeBr<sub>3</sub></i> (JCPDS)	5.635(9)	88.74(4)	(0.476(4), 0.476(4), 0.476(4))	1.009(4)
<i>CsGeBr<sub>3</sub></i> (exp.)	5.647(5)	88.79(3)	(0.494(1), 0.494(1), 0.494(1))	
<i>CsGeBr<sub>3</sub></i> ( <i>ab initio</i> )	5.688(5)	88.29(7)	(0.470(9), 0.470(9), 0.470(9))	
<i>CsGeCl<sub>3</sub></i> (JCPDS)	5.434(2)	89.72(3)	(0.481(0), 0.481(0), 0.481(0))	1.027(2)
<i>CsGeCl<sub>3</sub></i> (exp.)	5.446(9)	89.70(8)	(0.499(3), 0.499(3), 0.499(3))	
<i>CsGeCl<sub>3</sub></i> ( <i>ab initio</i> )	5.510(8)	89.12(1)	(0.479(9), 0.479(9), 0.479(9))	

RGC diffraction pattern. From the crystal models used in this study, the water molecules are located between these atomic planes. The water molecules causes the change of interplanar spacing. The peak from [310] planes is found to achieve a minimum peak height when the water of crystallization is 50% occupied ( $x \approx 0.1$ ). The water molecules randomly occupy the crystallographic sites between the [310] planes and cause a reduction in structural factor. The lattice parameters of  $\text{RbGeCl}_3 \cdot x(\text{H}_2\text{O})$  crystals vary linearly with the amount of water.

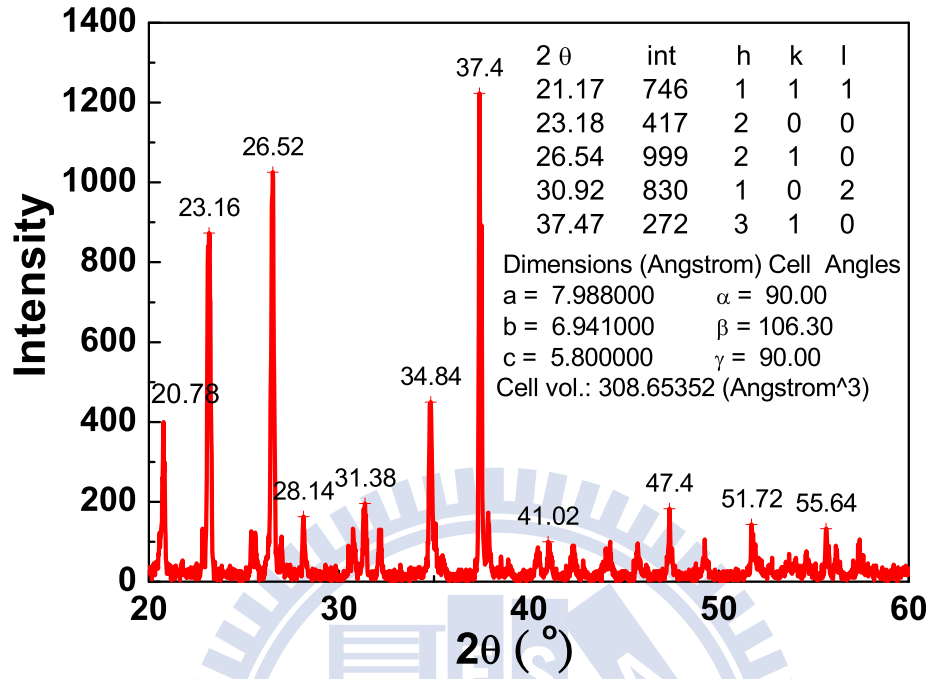


圖 3.1: X-ray powder diffraction of the crystal HRGC. It is shown that the XRD peaks shift from that of RGC. A major peak height at [310] is observed in the NLO crystals HRGC.

From the first-principles calculations based on the WIEN2k package, the equation-of-state parameters such as the bulk modulus and its pressure derivative can be deduced. The bulk modulus for  $\text{RbGeCl}_3 \cdot x(\text{H}_2\text{O})$  is about 9.11 GPa.

The HRGC crystal belongs to a monoclinic space group  $P2_1\bar{m}$  (No.11) with  $a=7.988 \text{ \AA}$ ,  $b=6.941 \text{ \AA}$ ,  $c=5.800 \text{ \AA}$ ,  $\alpha = \gamma = 90.0^\circ$ , and  $\beta =$

106.34°. Figure 3.11 shows the crystal packing along  $a$  and  $c$  directions. Three chloride atoms are bonded to a germanium atom to form a tetrahedron, and two such tetrahedrons are inversely mapped to each other in the primitive cell.

The germanium-chloride tetrahedrons form chain-like rows, which are parallel to one other, while rubidium atoms and water molecules are arranged between the germanium-chlorides chains. Each rubidium or water molecule is surrounded by three parallel germanium-chlorides chains. The bond length analysis showed that the bond lengths of germanium with two dangling chloride atoms, Ge-Cl(1) and Ge-Cl(2), were 2.722(3) Å and 2.738(3) Å, respectively, while the bond lengths of germanium with two bridging chloride atoms, Ge-Cl(3) and Ge-Cl(4), were 2.823(3) Å and 2.830(4) Å, respectively. So there is a distortion within one germanium-chlorides tetrahedron. Furthermore, the connecting ways of the germanium-chlorides tetrahedrons were similar, as the bridging chloride atoms were all located 'below' germanium atoms, while the two dangling chloride atoms within one tetrahedron were located 'above' germanium atoms as shown in Fig. 3.11. This means

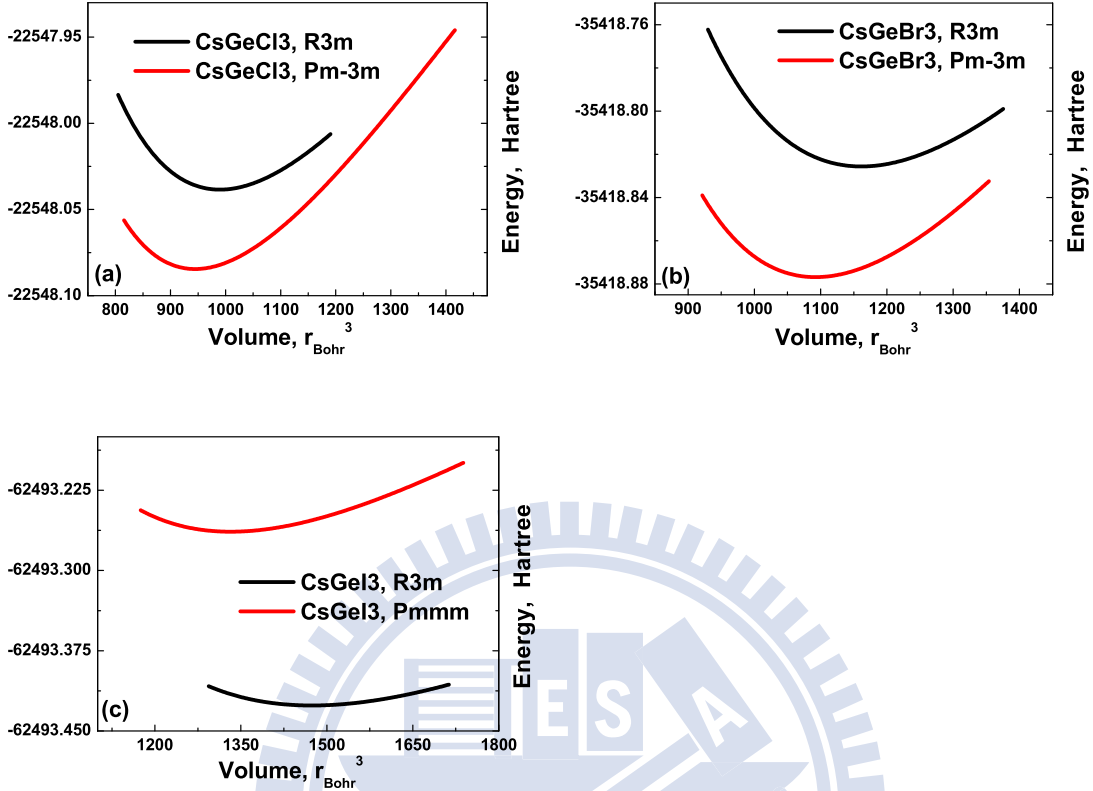


圖 3.2: Volume optimization results for the (a) rhombohedral (R3m) and cubic (Pm-3m)  $\text{CsGeCl}_3$ ; (b) rhombohedral (R3m) and cubic (Pm-3m)  $\text{CsGeBr}_3$ ; and (c) rhombohedral (R3m) and orthorhombic (Pmmm)  $\text{CsGeI}_3$ .

that the distortion directions of all tetrahedrons are similar. This packing mode is favorable for the accumulation of microscopic second-order NLO coefficient and leads to a relatively strong bulk NLO effect.

The equilibrium lattice constants and fractional atomic coordinates were deduced from the total-energy minimization procedure in the

WIEN2K package. Relaxation of lattice parameters and atomic positions was carried out under the constraint of the unit cell space-group symmetry. As shown in Table 3.1, the  $CsGeX_3$  crystals have a noncentrosymmetric rhombohedral space group  $R3m$ . The calculated results are shown in Fig. 3.2 and Table 3.3. It is found that the bulk modulus of  $CGC$  is the largest, and that of  $CGI$  is the smallest. We found that the cell volumes of the low temperature phase ( $R3m$ ) are larger than those of the high temperature phases (Pm-3m or Pmmm), except for  $CGI$ .

## 3.2 Electronic Band Structures and Density of States Analysis

The  $CGX$  crystals tend to extend along one of the  $\langle 111 \rangle$  directions. The calculated electronic band structures of rhombohedral  $CGX$  were behaved similarly. As shown in Fig. 3.3,  $CGX$  crystals have direct band gaps,  $E_G = \Delta E_R$ , at the R(111)-point. According to the electronic band structures of  $CGX$  shown in Fig. 3.3, band transition



energies at  $\Gamma$ -point,  $\Delta E_{\Gamma}$ , are also larger than that at the  $M$ -point,  $\Delta E_M$ . Namely, we have  $\Delta E_{\Gamma} > \Delta E_R > \Delta E_M = E_G$  in rhombohedral  $CGX$  crystals.

The experimental and the calculated band-gap values,  $E_G = \Delta E_R$ , of  $CGX$  both show a decreasing trend from  $CGC$  to  $CGI$ , and they are listed in the first two rows of Table 3.5. These electronic band structures of rhombohedral halides are quite different from the perovskite oxides,  $ABO_3$ , e.g.  $BaTiO_3$ ,  $PbTiO_3$ ,  $SrTiO_3$ , and  $LiNbO_3$ , etc.

As shown in Table 3.5, all calculated band-gap values of rhombohedral  $CGX$  crystals were underestimated with respect to the measured ones. From the density of states analysis in the Fig. 3.4, cation Ge which is located on the longest diagonal axis  $[111]$  plays a key role in determining the strengths of optical transitions.

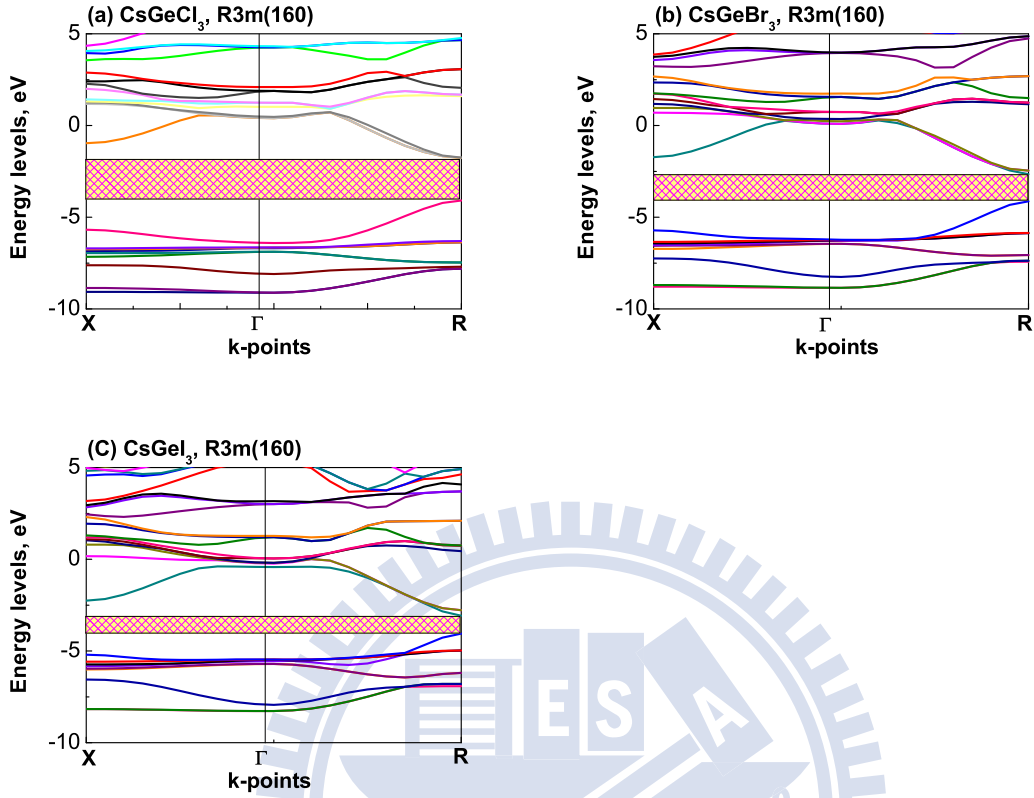


圖 3.3: Results for the calculated electronic band structure of  $CsGeX_3$ .

### 3.3 Electronic and Linear Optical Properties

The lattice parameters obtained above were used to calculate the electronic properties of  $CsGeX_3$  crystals. In order to understand the nature of optical transitions and other relevant effects on the calculated optical properties, an analysis of the local densities of states and other electronic properties of these  $CsGeX_3$  crystals were made.

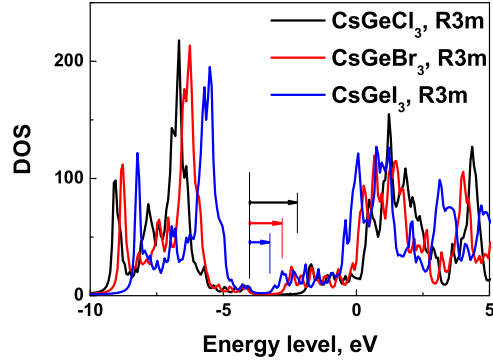


圖 3.4: The density of state analysis of rhombohedral  $CsGeX_3$  crystals.

The first principles calculation of frequency-dependent linear optical susceptibilities and electronic band structures of the stable phase CGX rhombohedral crystals,  $CsGeX_3$  (X=Cl, Br, and I) were performed by using the LASTO method. The self-consistent procedure was performed on the grid of 1000 k-points uniformly distributed in the irreducible tetragonal BZ. The CGX band structures obtained by the LASTO method are very similar to those obtained by the WIEN2K package. However, the LASTO methods is more efficient and it allows us to implement the computation for non-linear optical properties.

### 3.3.1 Linear Optical Properties and the Electronic Properties

The results for the imaginary part of the linear optical susceptibility,  $\text{Im}\chi_{ij}^{(1)}(\omega)$ , are plotted in Fig. 3.3. Although this part of the response function cannot be directly compared with experiment, it can be meaningfully related to the band structure. The structure in  $\text{Im}\chi_{ij}^{(1)}(\omega)$  can be attributed to the same general regions in the band structure for all  $CsGeX_3$ . The onset of the function occurs at the resonance around zero-frequency. The first peak is associated with the  $\Delta E_R = E_G$  optical transition. The second structure in the function for the most part arises from the  $\Delta E_M$  resonance. The complicated structure in the region between 3 and 5 eV is associated with  $\Delta E_T$  resonance with optical peak.

### 3.3.2 Linear Optical Properties and the Structural Effects

In Fig. 3.5, the imaginary parts of the frequency-dependent linear optical susceptibilities,  $\chi_{xx}^{(1)}$  and  $\chi_{zz}^{(1)}$ , for  $CsGeX_3$  are presented. There was few experimental results included for comparison. The main features

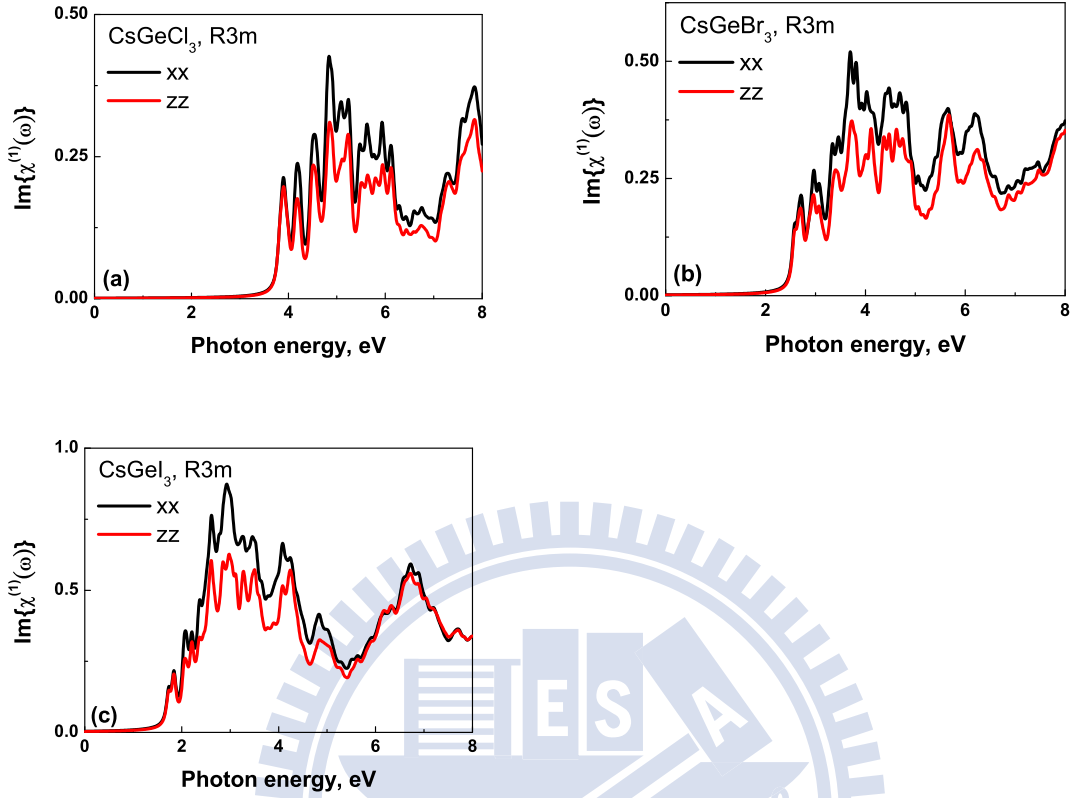


圖 3.5: Imaginary  $\chi_{xx}^{(1)}$  and  $\chi_{zz}^{(1)}$  for the rhombohedral  $CsGeX_3$  crystals.

of the linear response function can be attributed to the same regions of the electronic band structure for  $CGX$ .

In Fig. 3.6, the imaginary and real parts of the dielectric function,  $\epsilon''(\omega)$  and  $\epsilon'(\omega)$ , for  $CsGeX_3$  are presented in the last two rows. In the evaluation of all the response functions, the essential task is the integration of a function over IBZ. This is carried out by a "hybrid"

random sampling-tetrahedron method. We partition IBZ into many small tetrahedra, at whose vertices we evaluate the eigenvalues and velocity matrix elements on the basis of results from the calculations. The first peak is associated with  $\Delta E_R = E_G$  optical transition. The second structure in the function for the most part arises from  $\Delta E_M$  resonance.

In the evaluation of all the response functions, the essential task becomes the integration of a function over the IBZ. This we do in a 'hybrid' random sampling-tetrahedron method. We partition the IBZ into many small tetrahedra, at whose vertices we evaluate the eigenvalues and velocity matrix elements based on results from the calculations.

According equation 2.26, the unpolarized dielectric constants at zero-frequency of CGX were hightened from 4.8598 ( $\epsilon^{CGC}$ ) to 6.5313 ( $\epsilon^{CGI}$ ). These polarized dielectric constants,  $\epsilon_{zz}$  and  $\epsilon_{xx}$ , were increased in common with the unpolarized dielectric constant. The alike tendency was attributed with the structural distortion. The dielectric constants were about  $\epsilon^{CGC} : \epsilon^{CGB} : \epsilon^{CGI} \approx 12 : 13 : 16$ , and the first-principles calculated results were inceased as  $d_{Ge,cal}^{CGC} : d_{Ge,cal}^{CGB} : d_{Ge,cal}^{CGI} \approx 4 : 6 : 7$  and

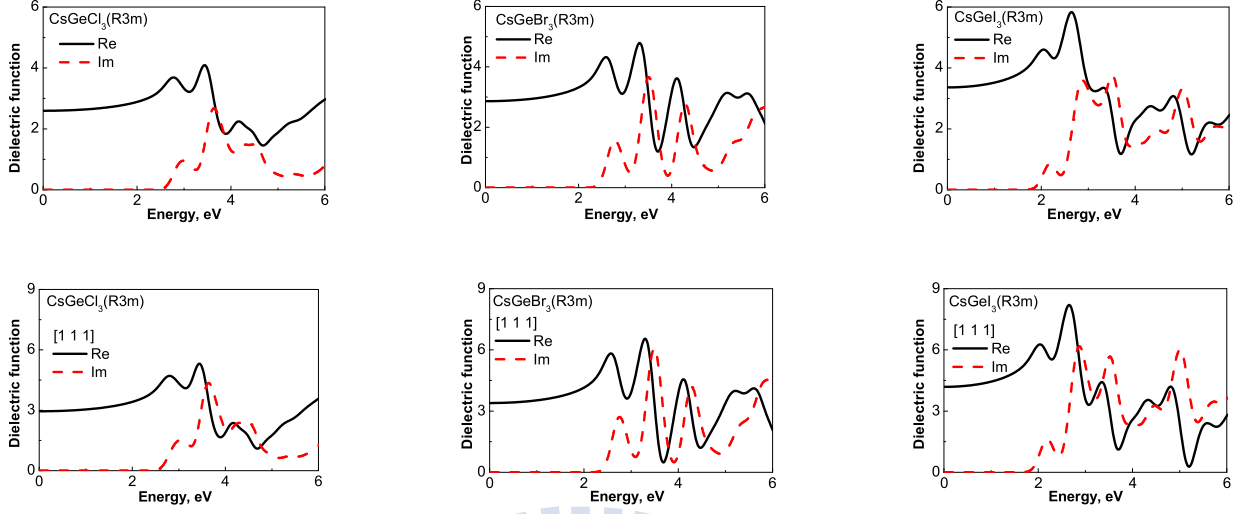


圖 3.6: Results for the calculated unpolarized dielectric function (the first row) and dielectric function in [111] direction of rhombohedral  $\text{CsGeX}_3$ .

$$\Delta\alpha_{cal}^{CGC} : \Delta\alpha_{cal}^{CGB} : \Delta\alpha_{cal}^{CGI} \approx 1 : 2 : 3.$$

### 3.4 Nonlinear Optical Properties

Various representative calculations of nonlinear bulk susceptibilities which adopt the summations-over-excited states (SOS) scheme were discussed in the review paper of B. Champagne and D. M. Bishop [101]. The models and calculating schemes employed in first principles calculations progressed in parallel to the development of *ab initio* band structure calculation. The scissors operator approximation, one of the

band-gap correction schemes, was good enough. However, in this study, we focused on the structural and the constituent effect on the NLO susceptibilities, and the 'scissors' correction scheme are implemented, discussed, and developed.

$CsGeX_3$  crystals belong to the crystal class 3m, which has the nonvanishing tensor elements,  $xzx = yzy$ ,  $xxz = yyz$ ,  $zxx = zyy$ ,  $zzz$ ,  $yyx = -yxx = -xxy = -xyx$  [1, 2, 17] assuming the Kleinman symmetry is valid [103]. For comparison, our calculated second-order non-linear optical susceptibilities,  $\chi_{ijk}^{(2)}$ , of rhombohedral  $CsGeCl_3$ ,  $CsGeBr_3$ , and  $CsGeI_3$  crystals are shown in Fig. 3.7 and Fig. 3.8. They were estimated from the first principles calculation based on the LASTO method and including the "scissor operator" correction.

Powder SHG measurements on sieved polycrystalline  $CGBr$  (Figure 3.9) and  $CGC$  revealed that the SHG efficiencies of  $CGBr$  and  $CGC$  higher than that of  $KDP$ . In figure 3.9, the detected SHG signals of  $CGBr$  in the higher (reflected) angle were saturated. The PMT detection sensitivity was kept the same magnitude and was not lowered



down, because the SHG signals of KDP (reference) can not be detected or identified in lower sensitivities. The integrated intensities were estimated from the reflection signals in various particle sizes, and showed the SHG responses of sieved polycrystalline  $CsGeBr_3$  were about 1.62 times larger than that of  $CsGeCl_3$  and 9.63 times larger than that of  $KH_2PO_4$  ( $KDP$ )(see Table 3.5). In addition, both  $CsGeBr_3$  and  $CsGeCl_3$  were phase-matchable (see Figure 3.10) as was  $KDP$ . That is, as the particle-size becomes substantially larger than the coherence length of the crystal, the collected SHG intensity gains no more and saturates as a certain value.

The estimate of the coherence length of the three crystals compared in this chapter is based on the position (particle size) of the saturation point. According to the relation between integrated  $I_{2\omega}$  with respect to average particle-size (Fig. 3.10), the coherence length  $L_c$  is  $\approx 200\mu m$  for KDP,  $\approx 150\mu m$  for CGC, and  $\approx 75\mu m$  for CGB.

$CsGeBr_3$  crystal is found in crystal class 3m, which has the nonvanishing tensor elements,  $xzx = yzy$ ,  $xxz = yyz$ ,  $zxx = zyy$ ,  $zzz$ ,  $yyy = -yxx = -xxy = -xyx$  [1, 2, 17] assuming Kleinman symmetry

is valid [103]. For comparison, *ab initio* calculated second-order non-linear optical susceptibilities of rhombohedral  $CsGeCl_3$ ,  $CsGeBr_3$ , and  $CsGeI_3$  crystals are shown in Table 3.6. They were estimated from the first principles calculation without integrating the band-gap correction scheme.

The  $d_{eff}$ , which were measured by PSHG method, was the accumulated effect, and the PSHG method was served as a screening technique of choosing proper NLO materials. It is hard to simulate the 2nd order NLO tensors,  $d_{ijk}^{(2)}$  or  $\chi_{ijk}^{(2)}$ , from a powder measurement. However, the responded trends of  $d_{eff}^{(2)}$ ,  $d_{ijk}^{(2)}$ , and  $\chi_{ijk}^{(2)}$  should be similar. Besides, there is a semi-empirical rule:  $d_{eff}^{(2)} \approx d_{ijk}^{(2)} = 1/2\chi_{ijk}^{(2)}$  [2]. In general, the magnitude of  $\chi_{ijk}^{(2)}$  is about double that of  $d_{eff}^{(2)}$ . The calculated second harmonic generation signal of CGB was  $\approx 2.8$  times larger than that of CGC crystal and  $\approx 2.7$  times smaller than that of CGI crystal. The major susceptibilities were increased as the atomic weight of halides was increased. This tendency is similar to the previous PSHG measurement. The measured NLO susceptibility of CGBr was not as large as the calculated one. The detected signals of CGBr in the high reflection angles (see Figure 3.9) were saturated, because the signals were much stronger than the detection threshold on PMT. If the de-

tection threshold on PMT were reranged to lower sensitivity to fulfill the stronger signal requirement, the signals of CGC and KDP would be too weak to detect or identify (Fig. 3.10). The reflected SHG signals and the under-estimated  $d_{eff}^{(2)}$  of CGB could be rescaled to  $\approx 5.19$  by a factor  $\approx 1.50$ . The rescaled  $d_{eff}^{(2)}$  of CGBr was about 2.45 times larger than that of  $CsGeCl_3$ , and was about half of the calculated  $\chi_{ijk}^{(2)}$ .

There are some reasons for the significant SHG signals of rhombohedral  $CsGeBr_3$  crystal. First of all, the SHG responses were contributed from the structural distortion and the off-centered  $Ge$  ion in the unit cell. The cell angle distortion of CGB is larger than that of CGC. The position of B-site cation,  $Ge$ , is closer to cell corner than that of CGC. The  $\chi_{zzz}^{(2)}$  increases as these distortions increases. Secondly, the band-gap values decreased [27, 28, 29, 30, 31, 12] and the NLO susceptibilities increased when the atomic weights of halides increased. The  $\chi_{ijk}^{(2)}$  is approximately inverse-proportional to the cubic of band-gap value [101, 2, 4]. (see Eq. 2.29) The third contribution has also been suggested that the electron lone-pair, the unbonding electron pair, of  $Ge$  which was polarized in [111] direction could give more contribution on

the MME summation. The lone-pair polarization was also mentioned in G. Thiele *et al*'s reports [27, 28, 29, 30, 31]. These reasons could form the important guidelines for further NLO crystal designation. Certain geometric (e.g., second-order Jahn-Teller, SOJT) distortions [104, 105, 106, 107, 108, 109, 110] were concerned with structural changes attributed to a nondegenerate ground state, interacting with a low-lying excited state. The distortion occurs where the energy gap between the highest occupied and lowest unoccupied molecular orbitals (HOMO/LUMO) is small and there is a symmetry-allowed distortion permitting the mixing of the HOMO and LUMO states. With perovskite-type ternary oxides as well as halides  $ABX_3$  ( $A = \text{Cs, Rb}$ ,  $B = \text{Ge, Cd}$ ,  $X = \text{Cl, Br, I}$ ), Goldschmidt's tolerance factor  $t$  [32, 33] serves as a discriminating parameter of classifying perovskites in terms of structure modifications and the resulting physical properties [34, 35, 36, 37, 38].

The type of stacking depends on the tolerance factor  $t_G$  define in eq. 1.1, where subscripts  $A$  and  $B$  denote the large and small cation, respectively and  $X$  denotes the anion.  $r$  denotes the ionic radii of Shannon and Prewitt [39, 40] which depend on the coordination number and bonding-specimens. The tolerance factor  $t$  of the  $\text{RbGeCl}_3$  crystal structure is

about 0.92 and far from the ideal value, 1.0. The  $t$ -ratio of  $\text{RbGeCl}_3$  and  $\text{CsGeCl}_3$  is similar to that of  $\text{SrTiO}_3$  and  $\text{BaTiO}_3$ .  $\text{RbGeCl}_3$  can be considered as a substitutional material for  $\text{CsGeCl}_3$  and their mixture can be used to tune the electronic or optical properties. The  $\text{RbGeCl}_3$  crystal belongs to a monoclinic space group  $P2_1\bar{m}$ , ( $a=7.988 \text{ \AA}$ ,  $b=6.941 \text{ \AA}$ ,  $c=5.800 \text{ \AA}$ ,  $\alpha = \gamma = 90^\circ$ ,  $\beta = 106.340^\circ$ )[46, 47], which can be considered as highly distorted perovskite crystal structure of  $\text{CsGeCl}_3$ , as shown in Fig. 3.11.

### 3.4.1 Second-order nonlinear optical susceptibilities

The optical SHG effect is investigated using a Kurtz powder technique. A Nd:YAG laser is utilized to generate fundamental 1064 nm light. Microcrystalline KDP served as the standard. The Kurtz powder SHG measurement showed that the intensity of double frequency signal is about one third as large as that of KDP which are 0.14 and 0.38 pm/V for HRGC and KDP [111], respectively. This result is in agreement with the above analysis of the molecular structure of HRGC.

The NLO coefficient for HRGC powder is compared with KDP using a semiquantitative methods, as illustrated in Chap. 2.5. A 1.064  $\mu\text{m}$  laser is split into two parts to irradiate the HRGC powder tablets and the KDP reference powder tablets. The SHG results for HRGC are about one third time as large as that of KDP references at 1.064 $\mu\text{m}$ , and the damage threshold is greater than 200 MW/cm<sup>2</sup> which is similar to that of CsGeCl<sub>3</sub> [22].

The Kurtz powder SHG measurement shows that the intensity of double frequency signal is about one third as large as that of KDP. This result is in agreement with above analysis of the molecular structure of HRGC. It is well known that second-order nonlinear optical susceptibility is much more sensitive to crystal structure than the linear optical susceptibility. The second-order nonlinear susceptibilities can be estimated according to eq. (3.1) in order to learn more about the hydrate-induced distortion. The value of  $d^2$  ( $= 2\chi^{(2)}$ ) is estimated to be 0.14 pm/V.

Powder SHG measurements on sieved polycrystalline HRGC revealed a less SHG efficiency 300 times that of KDP. In addition, the material

is phase-matchable (see Fig. 3.12). That is, as the particle size becomes substantially larger than the the coherence length of the crystal, the collected SHG intensity gains no more and saturates at a certain value. Our experimental results also revealed that HRGC is damaged under prolonged laser irradiation. The capillary tube became dark after several laser shots. This phenomenon did not occur when the tube is empty. On the basis of the intensity ratio between a phase-matchable material and KDP (which is also phase-matchable), one can calculate the average NLO bond susceptibility, [72]. For phase-matchable materials, the intensity ratio can be obtained [72]. The coherence length  $L_c$  is  $20 \mu\text{m}$  for KDP and is assumed to be  $15 \mu\text{m}$  for HRGC, whereas the average particle size  $\bar{r}$  is taken to be  $50 \mu\text{m}$  for both materials [72].

### 3.4.2 Structural Effects on Second-Order Nonlinear Susceptibilities

For the photon energy  $\hbar\omega$  of PSHG measurement well below the band-gaps, frequency-dependent  $\chi_{ijk}^{(2)}(\omega)$  and  $n(\omega)$  were nearly constants in this frequency region [2, 71]. The static  $\chi_{ijk}^{(2)}(0)$  could be considered as

good approximation to the frequency-dependent  $\chi_{ijk}^{(2)}(-2\omega; \omega, \omega)$  in the PSHG measurements. The second harmonic pattern over scattering angle to yield the total second harmonic intensity,  $I_{2\omega}$ , was integrated. The square of the effective nonlinearity,  $\langle d_{eff}^2 \rangle$ , averaged over the orientation distribution of crystalline powders of  $CsGeX_3$  was determined by

$$\begin{aligned}
 \langle d_{eff}^2 \rangle_{CGX} &= \\
 \langle d_{eff}^2 \rangle_{KDP} &\cdot \frac{I_{2\omega,CGX}^{total} \cdot n_{\omega,CGX}^2 \cdot n_{2\omega,CGX}}{I_{2\omega,KDP}^{total} \cdot n_{\omega,KDP}^2 \cdot n_{2\omega,KDP}} \\
 &\approx \langle d_{eff}^2 \rangle_{KDP} \cdot \frac{I_{2\omega,CGX}^{total} \cdot n_{CGX}^3}{I_{2\omega,KDP}^{total} \cdot n_{KDP}^3} \quad (3.1)
 \end{aligned}$$

with a reference NLO crystal, e.g. KDP, when  $n \approx n_{\omega} \approx n_{2\omega}$ . Powder *SHG* measurements revealed that the SHG efficiencies of CGB were higher than that of CGC. The band-gap of *CGI* is too small to detect the *SHG* signal of it. The detected *SHG* signals of The integrated intensities were estimated from the reflection signals in various particle sizes, and showed the SHG responses of sieved polycrystalline  $CsGeBr_3$  were about 1.62 times larger than that of  $CsGeCl_3$  and 9.63 times larger than that of KDP by Tang et al.[12, 11] (see Table 3.5)



The  $d_{eff}$ , which were measured by PSHG method, was the accumulated effect, and the PSHG method was served as a screening technique of choosing proper NLO materials. It is hard to simulate the 2nd order NLO tensors,  $d_{ijk}^{(2)}$  or  $\chi_{ijk}^{(2)}$ , from a powder measurement. However, the responded trends of  $d_{eff}^{(2)}$ ,  $d_{ijk}^{(2)}$ , and  $\chi_{ijk}^{(2)}$  should be similar. Besides, there is a semi-empirical rule:  $d_{eff}^{(2)} \approx d_{ijk}^{(2)} = 1/2\chi_{ijk}^{(2)}$ . [2]

The first principles calculation nonlinear coefficients of rhombohedral nonlinear optical crystals,  $CsGeX_3$  (X=Cl, Br, and I), were performed and listed in Table 3.5. The nonlinear coefficients of rhombohedral nonlinear optical crystals,  $CsGeX_3$ , were compared with the available powder second-harmonic generation (PSHG) measurement[12, 11]. In Table 3.5, all  $\chi_{ijk}^{(2)}(0)$  were enhanced in common with the magnitudes of dielectric constant of CGX, i.e.  $\chi_{CGC}^{(2)}(0) < \chi_{CGB}^{(2)}(0) < \chi_{CGI}^{(2)}(0)$ . This tendency was also related to the distortional factors as  $d_{Ge}^{CGC} < d_{Ge}^{CGB} < d_{Ge}^{CGI}$ .

In general, the magnitude of  $\chi_{ijk}^{(2)}$  is about double that of  $d_{eff}^{(2)}$ . The calculated  $\chi_{zzz}^{(2)}$  of CGB was  $\approx 2.0$  times larger than that of CGC crystal

and  $\approx 5.8$  times smaller than that of CGI crystal. The major susceptibilities were increased as the atomic weight of halides was increased. This tendency is similar to the previous PSHG measurement. The reflected SHG signals and the under-estimated  $d_{eff}^{(2)}$  of CGB was about 1.63 times larger than that of  $CsGeCl_3$ [12, 11].

### 3.4.3 Electronic Properties and Second-Order Nonlinear Susceptibilities

The original contributions came from the species Ge and X. This behavior was in common with that of frequency-dependent linear optical susceptibilities. The magnitudes of  $\chi_{ijk}^{(2)}$  were inversely proportional to the bandgap (shown in the first two rows in Table 3.5),  $E_G^{CGC} > E_G^{CGB} > E_G^{CGI}$ , of CGX, and were proportional to the degree of distortion.

### 3.5 Transmittance spectrum

According to the first-principles calculation result, the  $\text{RbGeCl}_3$  crystal has a direct band gap (see Fig. 4.4) with potential applications as efficient absorber or photon emitter. To gain more insight into the calculated optical properties, we further studied the PDOS and LDOS spectra of these crystals. The calculated PDOS for  $\text{RbGeCl}_3$  are presented in Fig. 3.14. Based on Fig. 3.14, the HOMO/LUMO values depend on the contributions of the germaniums and the chlorines.

Furthermore, in Fig. 3.15(a), absorption spectrum measured on single crystal  $\text{RbGeCl}_3 \cdot x(\text{H}_2\text{O})$  in visible range is shown. The absorption edge is 3.84 eV. The resulting bandgap of  $\text{RbGeCl}_3 \cdot x(\text{H}_2\text{O})$  can be tuned linearly in a wide spectral range by adjusting the substitution composition. From the UV-vis-near IR spectrum of HRGC (Fig. 3.15(a)), it is transparent in the visible region and even extended to about 350 nm, which is the absorption edge of HRGC. According to these data, the band gap of the HRGC is estimated to be 4 eV, which is even larger than the band gap of the famous  $\text{LiNbO}_3$  (3.5eV) crystal. The band gap is related to the laser damage threshold. The larger the band gap exists, the higher the laser damage threshold is. So, the

HRGC is expected to have high laser damage threshold.

The FTIR spectrum of HRGC crystalline powder is shown in Fig. 3.15(b). The transmittance is higher than 90% ranged from 2.5 to 25  $\mu\text{m}$ . There were few absorption peaks at 2.5 - 2.7  $\mu\text{m}$ , 3.0 - 5.9  $\mu\text{m}$  belong to the symmetric- and asymmetric-stretching of the crystalline water. So the transparent range of HRGC were from 2.0 - 20  $\mu\text{m}$ .

Infrared spectra were recorded on the (Perkin Elmer instruments Spectrum One) spectrometer in the range from 400  $\text{cm}^{-1}$  to 4000  $\text{cm}^{-1}$ , i.e. 2.5  $\mu\text{m}$  to 25  $\mu\text{m}$ , with the sample pressed between two *KBr* pellets. The transmittance of *CsGeBr<sub>3</sub>* powder was higher than 60% in mid-infrared range, from 2.5  $\mu\text{m}$  to 22.5  $\mu\text{m}$ . (see Figure 3.16) That meant SHG signals could transmit in NLO *CsGeBr<sub>3</sub>* single crystal. This transmission property in IR spectrum was similar to other NLO ternary halides, e.g. *CsGeCl<sub>3</sub>*, *CsGeI<sub>3</sub>* and superior to NLO oxide crystals, e.g. BBO, KTP.

The Raman spectrum of HRGC crystalline powder is shown in Fig. 3.15(c). The peaks at 324.28, 278.02, 251.72, 175.50, and 124.88  $cm^{-1}$  are due to the stretching of the 3-fold bonds in the  $Ge-Cl_3^-$  cluster and the A-site cation vibration. There are no other peaks in the region. So the transparent region of HRGC is wide (from 0.31 to 30.84  $\mu m$ ). This is of vital importance to many applied realms such as scout and other civil applications.

### 3.6 Thermogravimetric Analysis

There were four parts of thermal and structural responses, which were observed in this thermogravimetric measurement. (see Figure 3.17(a)) The resulted curve of TGA/DTA measurements on HRGC powder (Fig. 3.17(b)) reveals one transition in the range of 250-260°C, corresponding to a weight loss about 1.093%, which is in agreement with the calculated weight loss of water. The main weight loss occurred at temperature above 400°C.

No significant weight loss or phase change was observed from room

temperature up to 200°C. Slight DTG peak of CGB at 242.9°C indicated the phase change from rhombohedral to cubic. The phase change temperature was similar to the reports of G Thiele *et al* [29, 30]. The  $CsGeBr_3$  became the liquid phase around 352.5°C from cubic solid state phase when the temperature increased. The temperature DTG peak at 410.7°C showed that CGB was thermally decomposed when the temperature was higher 410.7°C. In summary, the NLO  $CsGeBr_3$  crystal could be properly operated under 200°C.

### 3.7 Results and Discussion

The species projected contributions to  $\chi_{xx}^{(2)}$ ,  $\chi_{xz}^{(2)}$ ,  $\chi_{zx}^{(2)}$ , and  $\chi_{zz}^{(2)}$  in rhombohedral  $CsGeX_3$  are shown in (Figures 3.18, 3.19, and 3.20). The main peaks of projected  $\chi_{ijk}^{(2)}$  of CGX are observed around the band edges. The dominant contributions come from the species Ge and X. This behavior is similar to that of the dielectric function. The magnitudes of  $\chi_{ijk}^{(2)}$  are inversely proportional to the bandgap (shown in the first two rows in Table 3.5),  $E_G^{CGC} > E_G^{CGB} > E_G^{CGI}$ , of CGX, and are

proportional to the degree of distortion.

There are two groups of significant peaks found in each second-order nonlinear optical susceptibility. First group of significant peaks is due to the second term in eq. 2.25, which is the sum of transitions from all valence states to the components in a conduction-band state associated with a given species, mediated by all possible intermediate states. Thus, these peaks are related to the conduction-band PDOS. The other group of peaks is due to the first term in eq. 2.25, which is the sum of transitions from the components in a valence-band state associated with a given species to all valence states, mediated by all possible intermediate states. Thus, these peaks are related to the valence-band PDOS. We found a close relationship between the relative positions of these peaks and the B-site cation displacement,  $d_{Ge}$ . according to our analysis for B-site cation displacement discussed above, we have  $d_{Ge,cal}^{CGC} : d_{Ge,cal}^{CGB} : d_{Ge,cal}^{CGI} \approx 4:6:7$ . The magnitudes and energy levels of the strongest peaks in group two are found to be 31.72 pm/V at -0.75eV for CGC, 00, -46.73 pm/V at -1.15eV for CGB, and -93.86 pm/V at -1.35eV for CGI, respectively. The energy levels of peak-deviation,  $p_D$ ,

are in a similar ratio, i.e.  $p_D^{CGC} : p_D^{CGB} : p_D^{CGI} \approx 4:6:7$ .

There are some reasons for the significant SHG signals of rhombohedral CsGeX<sub>3</sub> crystals. First of all, the SHG responses are contributed from the structural distortion and the off-centered Ge ion in the unit cell. The cell angle distortion of CGB is larger than that of CGC. The position of B-site cation, Ge in CGB, is closer to cell corner than that of CGC. The  $\chi_{zzz}^{(2)}$  increases as these distortions increase. Secondly, the band-gap values decrease [27, 28, 29, 30, 31, 12] and the NLO susceptibilities increase when the atomic weights of halides increase. The  $\chi_{ijk}^{(2)}$  is approximately inverse-proportional to the cubic of band-gap value [101, 2, 4]. (see Eq. 2.29) The third contribution has also been suggested that the electron lone-pair, the unbonding electron pair, of Ge which is polarized in the [111] direction could give stronger MME. For incident light polarized along [111]. This explains why the dielectric function for [111] polarized light is stronger than that for unpolarized light as seen in Fig. 3.6. The lone-pair polarization is also mentioned in Thiele *et al*'s reports [27, 28, 29, 30, 31]. These reasons could form the important guidelines for further NLO crystal design.



Experimental data at energies above the gap are very scarce for the materials considered here. The only data are listed in Table 3.5. The calculated energy bandgap are about 30% smaller than the experimental observation; however, this is to be expected at the level of the LDA methodology. The smaller bandgap also overestimates the NLO susceptibility. Although the smaller bandgap obtained with LDA can be corrected with a simple scissors approximation or more sophisticated GW correction, we did not intend to do so in this study. Our calculated second-order susceptibilities agreed reasonably well with available calculated and experimental results.

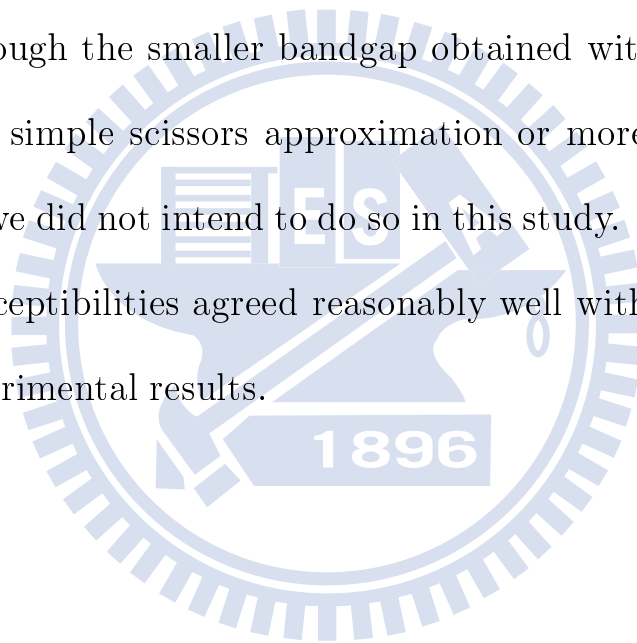


表 3.3: Bulk modulus, the optimized volumes, and the minimized total energies of the rhombohedral  $NLO$  crystals  $CsGeX_3$ .

(from eq.2.16)	$V_o$	$B$ (GPa)	$B'$	$E_o$
$CGC (R3m)$	989.8389	32.0868	4.3299	-22548.038446
$CGB (R3m)$	1161.7166	26.7310	4.3544	-35418.825606
$CGI (R3m)$	1473.8579	19.1247	4.2286	-62493.426167
$CGC (Pm - 3m)$	943.8503	36.6837	5.1252	-22548.084600
$CGB (Pm - 3m)$	1092.0108	30.4041	4.5134	-35418.876778
$CGI (Pmmm)$	1331.4844	25.2963	5.0481	-62493.263767
(from eq.2.17)	$V_o$	$B$ (GPa)	$B'$	$E_o$
$CGC (R3m)$	989.7925	32.3933	4.3607	-22548.038460
$CGB (R3m)$	1161.4951	26.9679	4.4539	-35418.825616
$CGI (R3m)$	1473.8799	19.2149	4.1967	-62493.426171
$CGC (Pm - 3m)$	944.6618	36.1070	4.4306	-22548.084544
$CGB (Pm - 3m)$	1092.2629	30.6591	4.4012	-35418.876814
$CGI (Pmmm)$	1332.2423	25.1711	4.6082	-62493.263719

表 3.4: Calculated optical properties, the linear and second order optical responses at zero frequency and non-linear optical coefficients of  $CsGeX_3$  (X=Cl, Br, and I) crystals . Available experimental data are also listed for comparison.

NLO crystal	$CsGeCl_3$	$CsGeBr_3$	$CsGeI_3$	
$E_{g,exp}$	3.67	2.32	1.53	Ref. [12, 11]
$E_{g,cal}$	2.26(5)	1.49(1)	1.01(6)	direct, R-point
$\chi_{zz}^{(1)}$	8.8477(5)	10.183(0)	12.551(4)	zero-frequency
$\chi_{xx}^{(1)}$	6.6550(5)	7.5836(7)	9.5420(6)	zero-frequency
$d_{eff,exp}^{(2)}$	2.12	3.46	NA	(pm/V) Ref. [12, 11]
$\chi_{zzz}^{(2)}$	11.64924	22.39020	127.7794	zero-frequency (pm/V)
$\chi_{zxx}^{(2)}$	2.629566	2.672494	4.590949	zero-frequency (pm/V)

表 3.5: Non-linear optical coefficients of NLO crystals  $CsGeBr_3$ ,  $CsGeCl_3$ ,  $KDP$ (as a reference), and  $BBO$ . They were integrated from the reflection powder second-harmonic generation signals in same measured conditions

NLO crystal	$n(\lambda = 1.064\mu m)$	$d_{eff}$ (pm/V)	$d_{eff}/d_{KDP}$
$CsGeBr_3$	2.31	3.46	9.63
$CsGeCl_3$	2.30	2.12	5.90
$KDP$	1.50	0.36	1.00
$BBO$	1.66	1.66	4.61

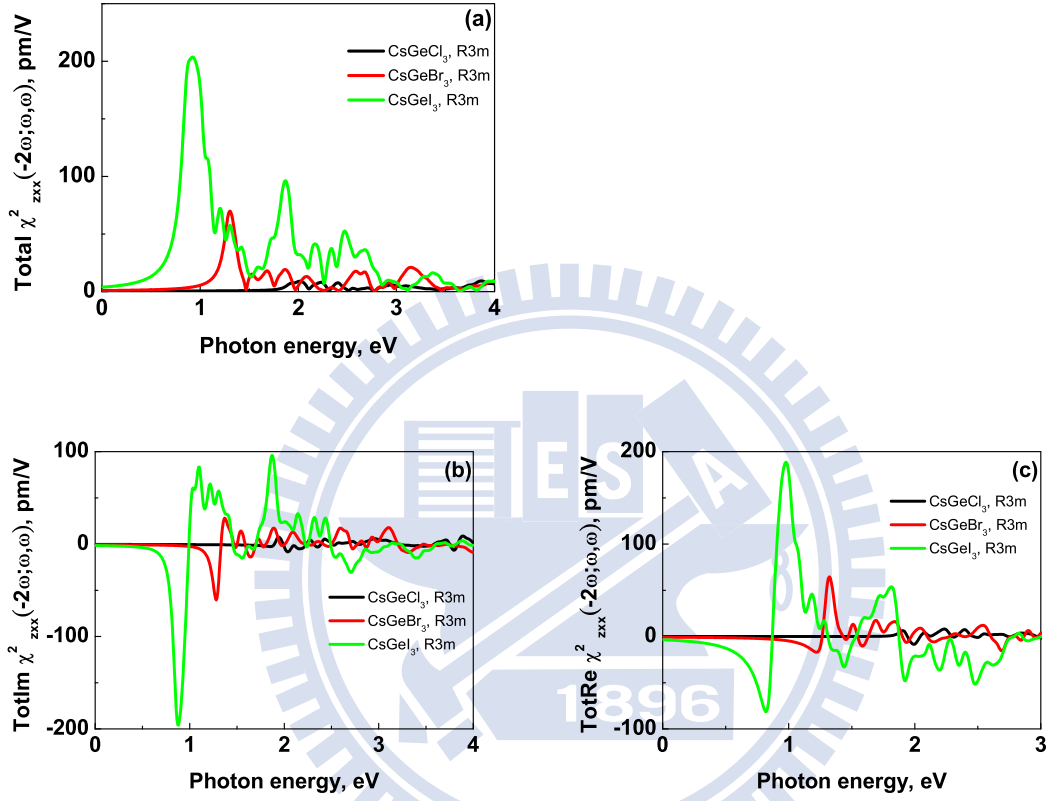


Figure 3.7: The total (a) absolute, (b) imaginary part, and (c) real part of frequency-dependent second-order nonlinear optical susceptibility, component  $\chi_{zxx}^{(2)}$ , by using equation 2.27 are calculated for  $CsGeCl_3$  (black),  $CsGeBr_3$  (red), and  $CsGeI_3$  (green).

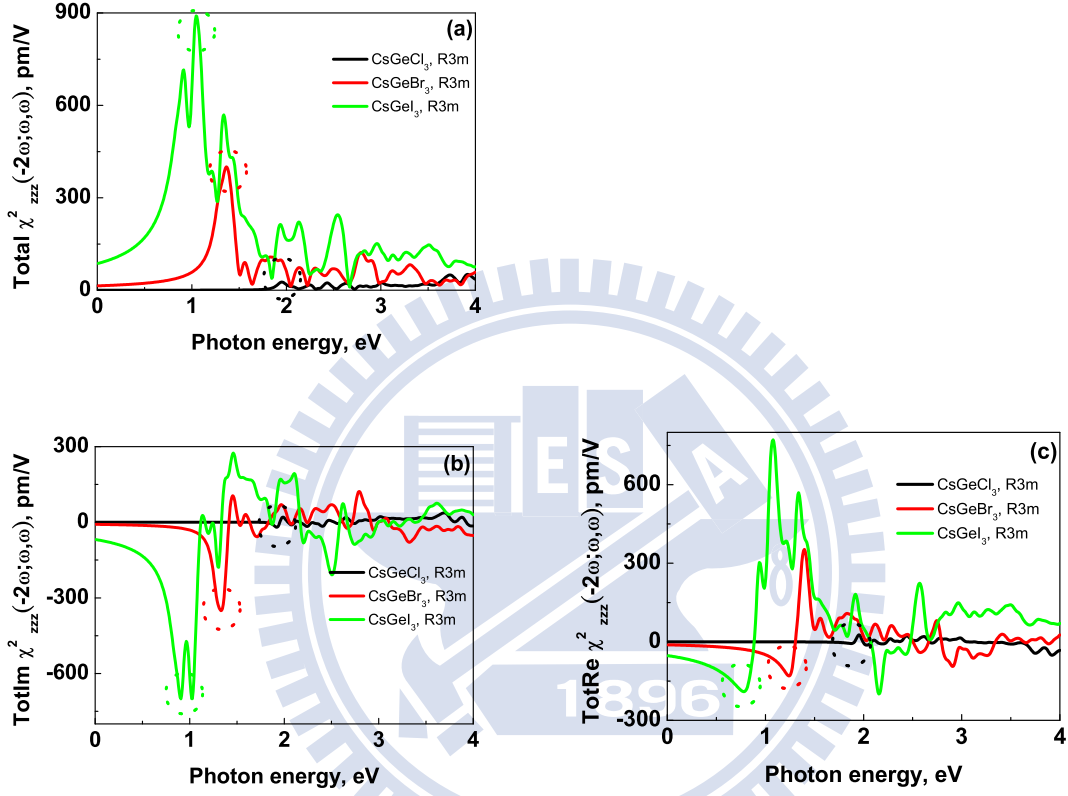


Figure 3.8: The total (a) absolute, (b) imaginary part, and (c) real part of frequency-dependent second-order nonlinear optical susceptibility, component  $\chi_{zzz}^{(2)}$ , by using equation 2.27 are calculated for  $CsGeCl_3$  (black),  $CsGeBr_3$  (red), and  $CsGeI_3$  (green).

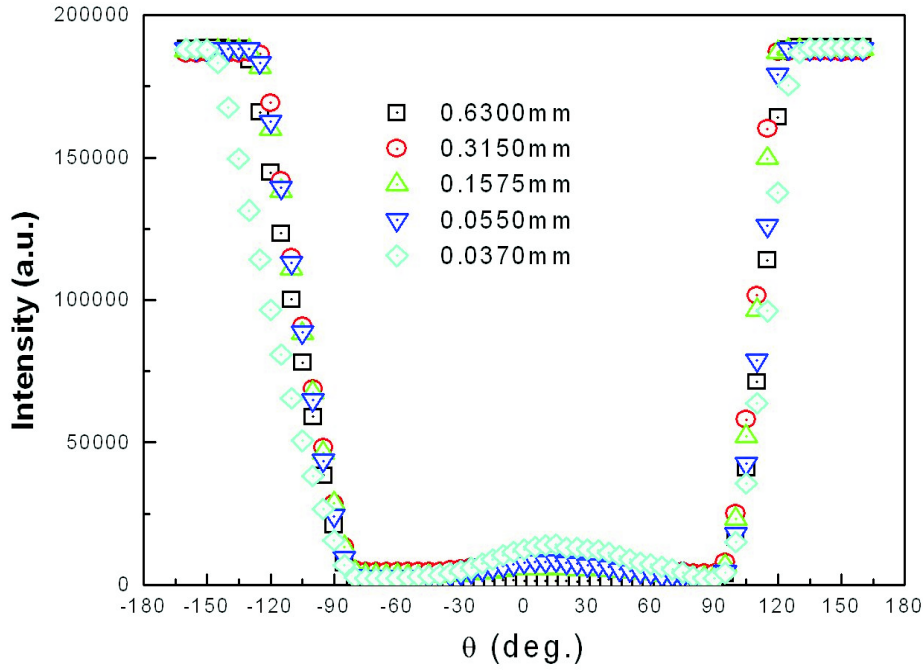


圖 3.9: The powder second harmonic generation results of rhombohedral nonlinear optical crystal  $CsGeBr_3$

表 3.6: Second-order non-linear optical susceptibilities of rhombohedral  $CsGeCl_3$ ,  $CsGeBr_3$ , and  $CsGeI_3$  crystals. They were estimated from the *ab initio* without employing the band-gap correction scheme

NLO crystal	$\chi_{zzz}^{(2)}$ (pm/V)	$\chi_{xyy}^{(2)}$ (pm/V)
$CsGeCl_3$	3.698	0.925
$CsGeBr_3$	10.40	1.112
$CsGeI_3$	28.36	0.918

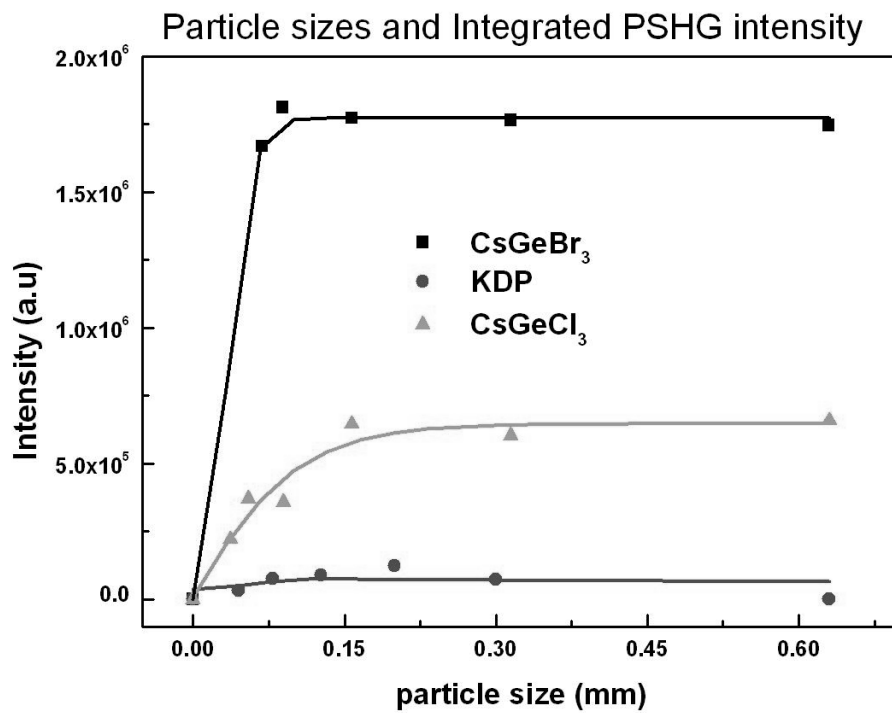


圖 3.10: The comparison of integrated powder second harmonic generation intensity of nonlinear optical crystal *KDP*, *CsGeCl<sub>3</sub>* and *CsGeBr<sub>3</sub>*

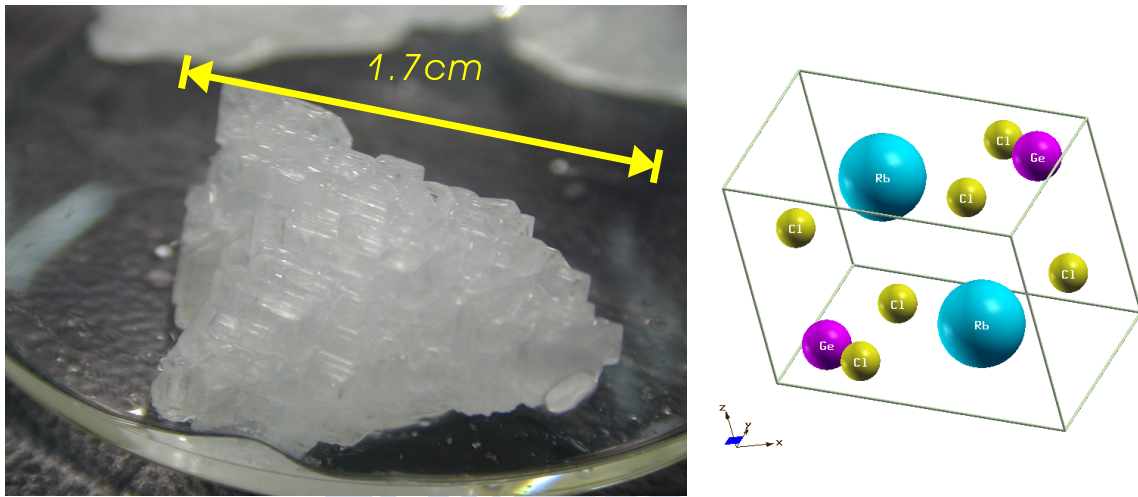


圖 3.11: One of the as-grown  $\text{RbGeCl}_3 \cdot x(\text{H}_2\text{O})$  crystals and the crystal structure model of the monoclinic  $\text{RbGeCl}_3$  crystal, whose space group is  $P2_1\bar{m}$ .



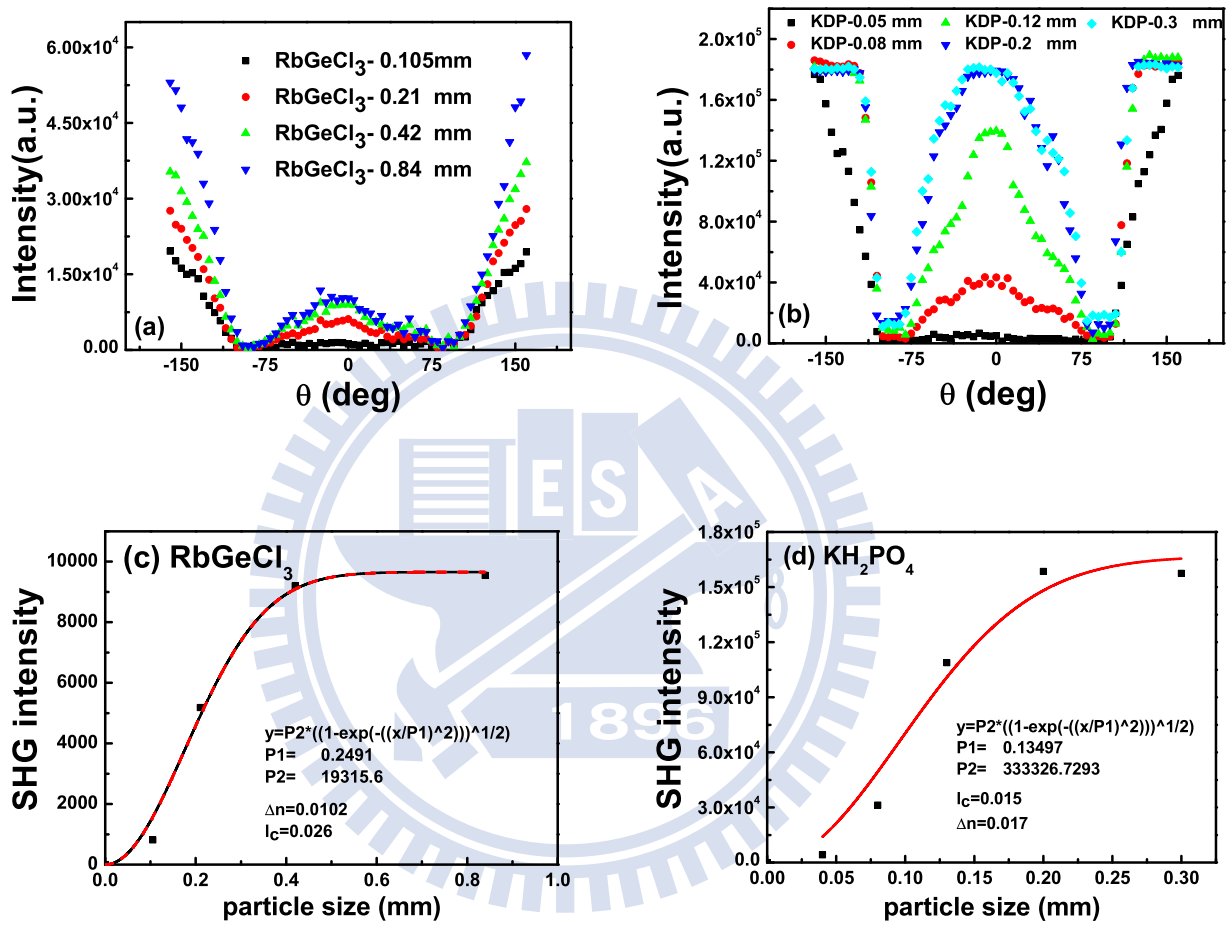


圖 3.12: Analysis of hyradizayion contribution in the NLO crystals the second-harmonic susceptibility  $\chi^{(2)}$  and the scaled values of  $\chi^{(2)}$  of the NLO crystals  $\text{RbGeCl}_3\text{H}_2\text{O}$ .

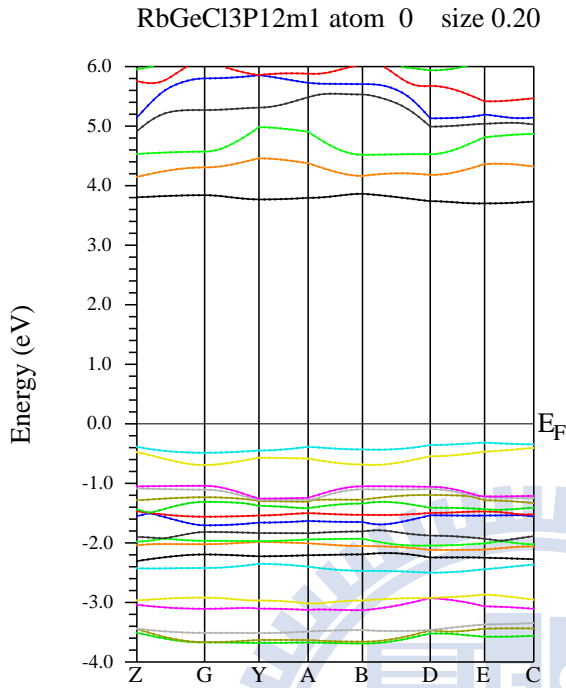


圖 3.13: Electronic band structure of the crystals RbGeCl<sub>3</sub>

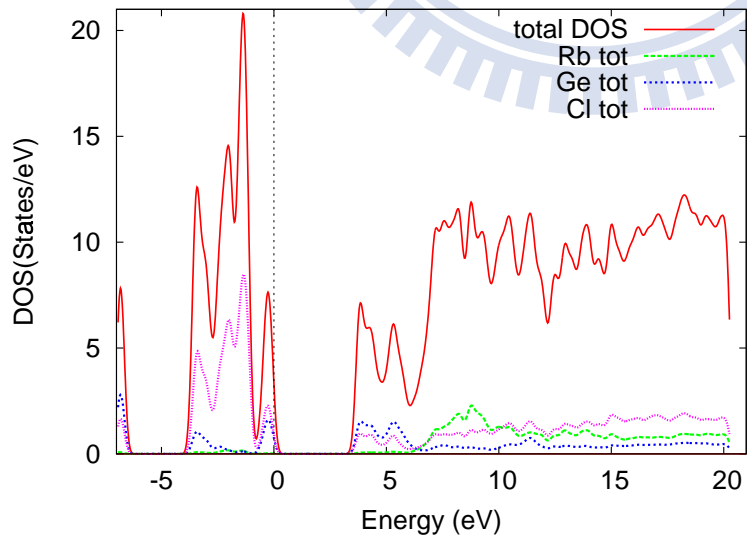


圖 3.14: The density of state analysis contribution in the crystals RbGeCl<sub>3</sub>

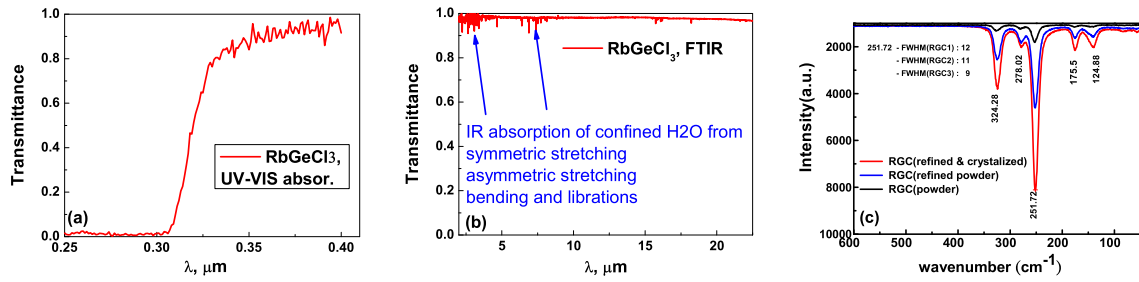


圖 3.15: (a) Measured transmittance of the crystal  $\text{RbGeCl}_3 \cdot x(\text{H}_2\text{O})$ . (b) The measured FTIR of the crystal  $\text{RbGeCl}_3 \cdot x(\text{H}_2\text{O})$ . (c) The measured Raman spectra the crystal  $\text{RbGeCl}_3 \cdot x(\text{H}_2\text{O})$ .

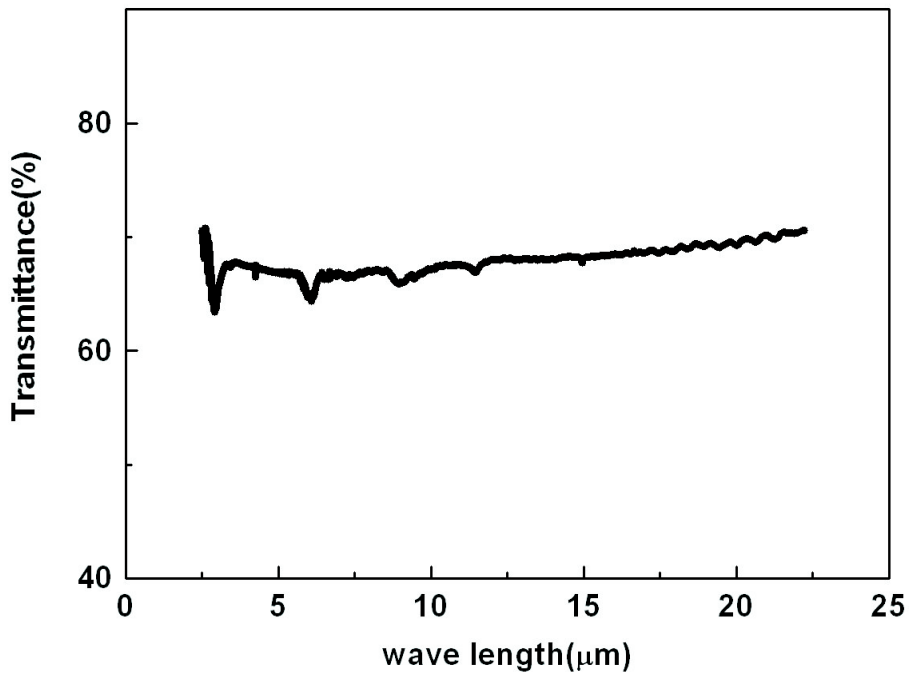


圖 3.16: The transmission analysis of rhombohedral nonlinear optical crystal  $\text{CsGeBr}_3$  in the mid-infrared range

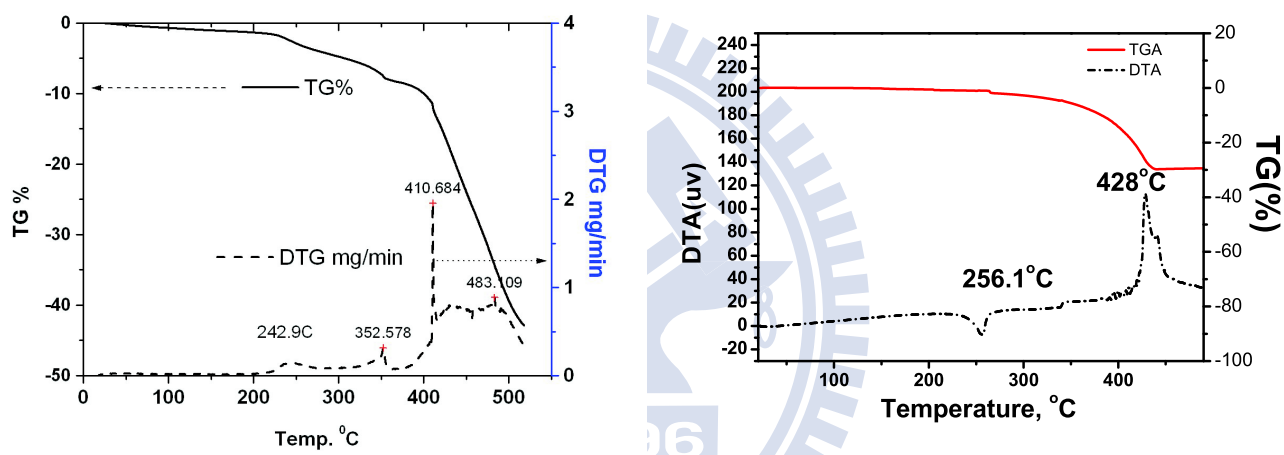


圖 3.17: The thermal analysis of (a) rhombohedral nonlinear optical crystal  $CsGeBr_3$  and (b) monoclinic nonlinear optical crystal HRGC.

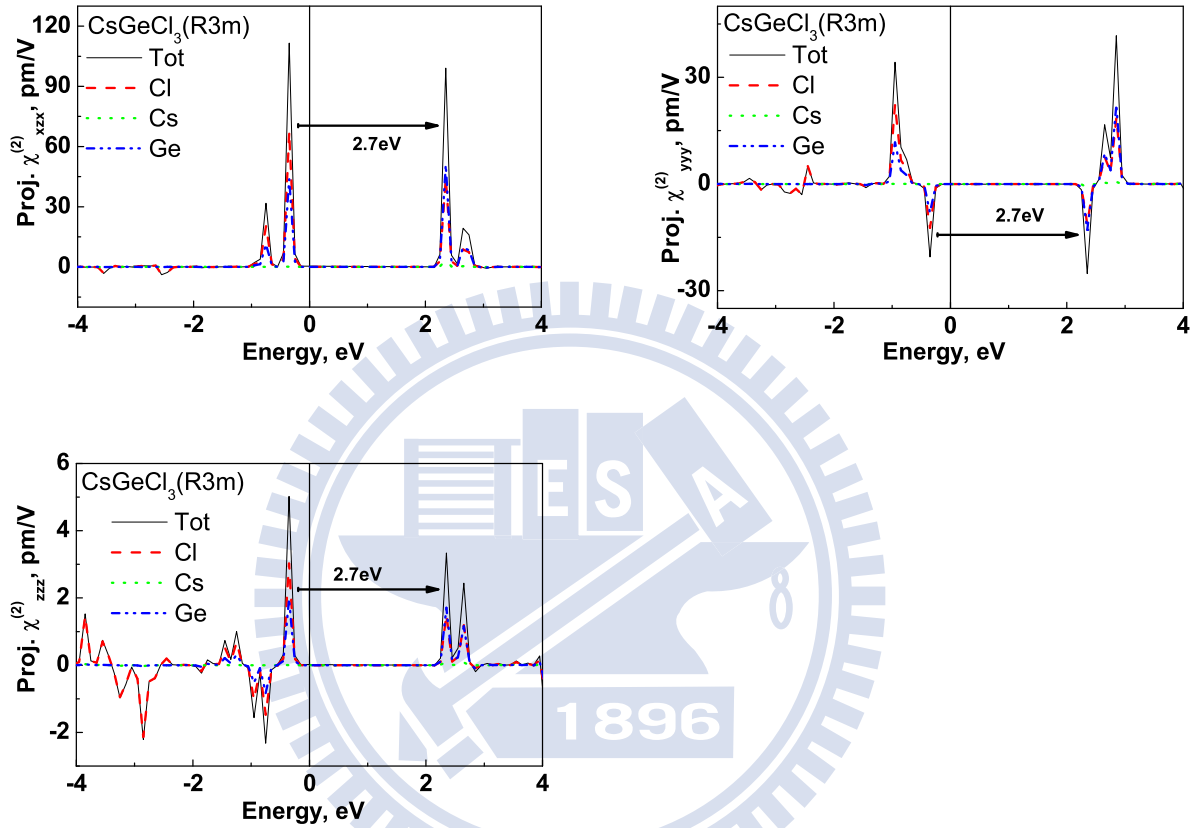


图 3.18: Second-order nonlinear optical susceptibility components of rhombohedral  $\text{CsGeCl}_3$  projected for various atomic species and energy bands using eq. 2.25. The contribution of each species is projected to  $\chi_{xzx}^{(2)} (= \chi_{zxx}^{(2)})$ ,  $\chi_{yyy}^{(2)}$ , and  $\chi_{zzz}^{(2)}$  in  $\text{CsGeCl}_3$ . Absolute value of SHG susceptibility  $\chi_{xyz}^{(2)}(\omega; \omega, 0)$ , solid line for  $\text{CsGeCl}_3$ .

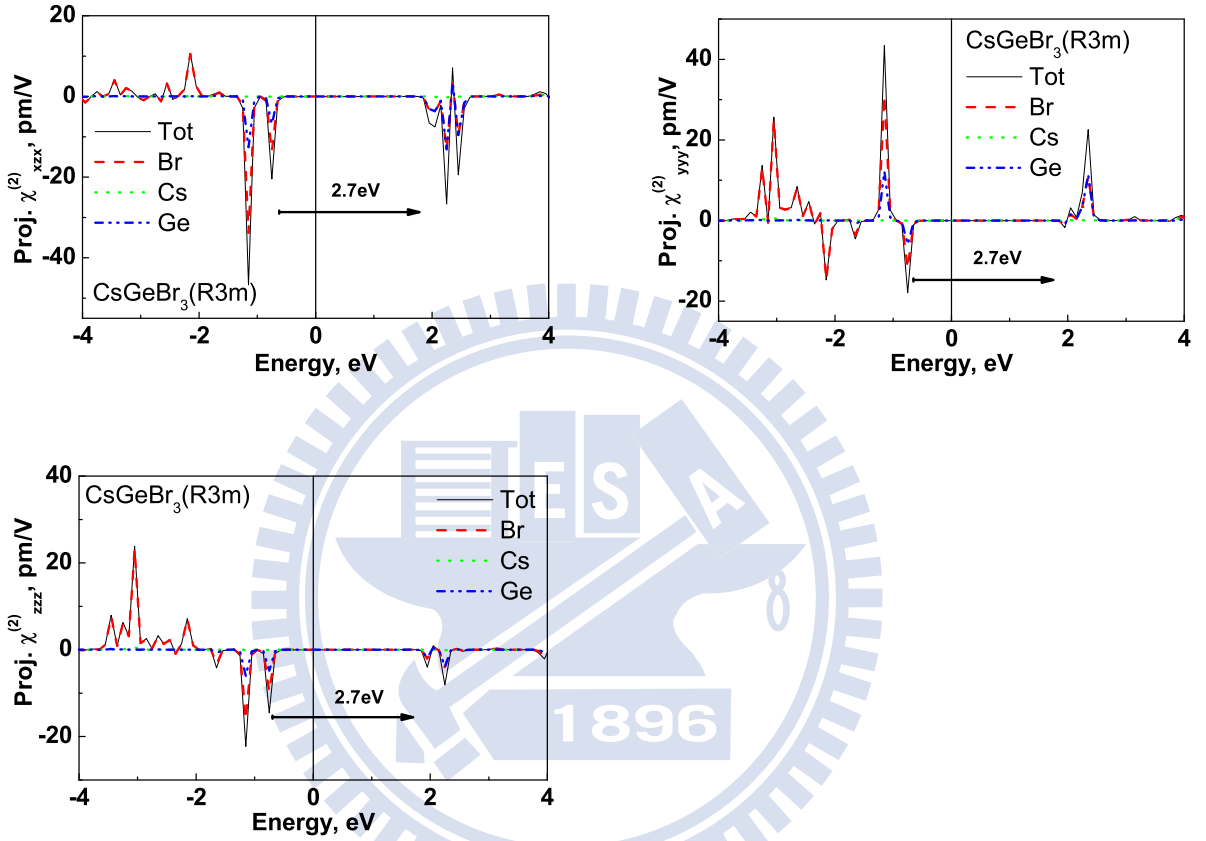


圖 3.19: Second-order nonlinear optical susceptibility components of rhombohedral  $\text{CsGeBr}_3$  projected for various atomic species and energy bands using eq. 2.25. The contribution of each species is projected to  $\chi_{xzx}^{(2)}$  ( $=\chi_{zxx}^{(2)}$ ),  $\chi_{yyy}^{(2)}$ , and  $\chi_{zzz}^{(2)}$  in  $\text{CsGeBr}_3$ . Absolute value of SHG susceptibility  $\chi_{xyz}^{(2)}(\omega; \omega, 0)$ , solid line for  $\text{CsGeBr}_3$ .

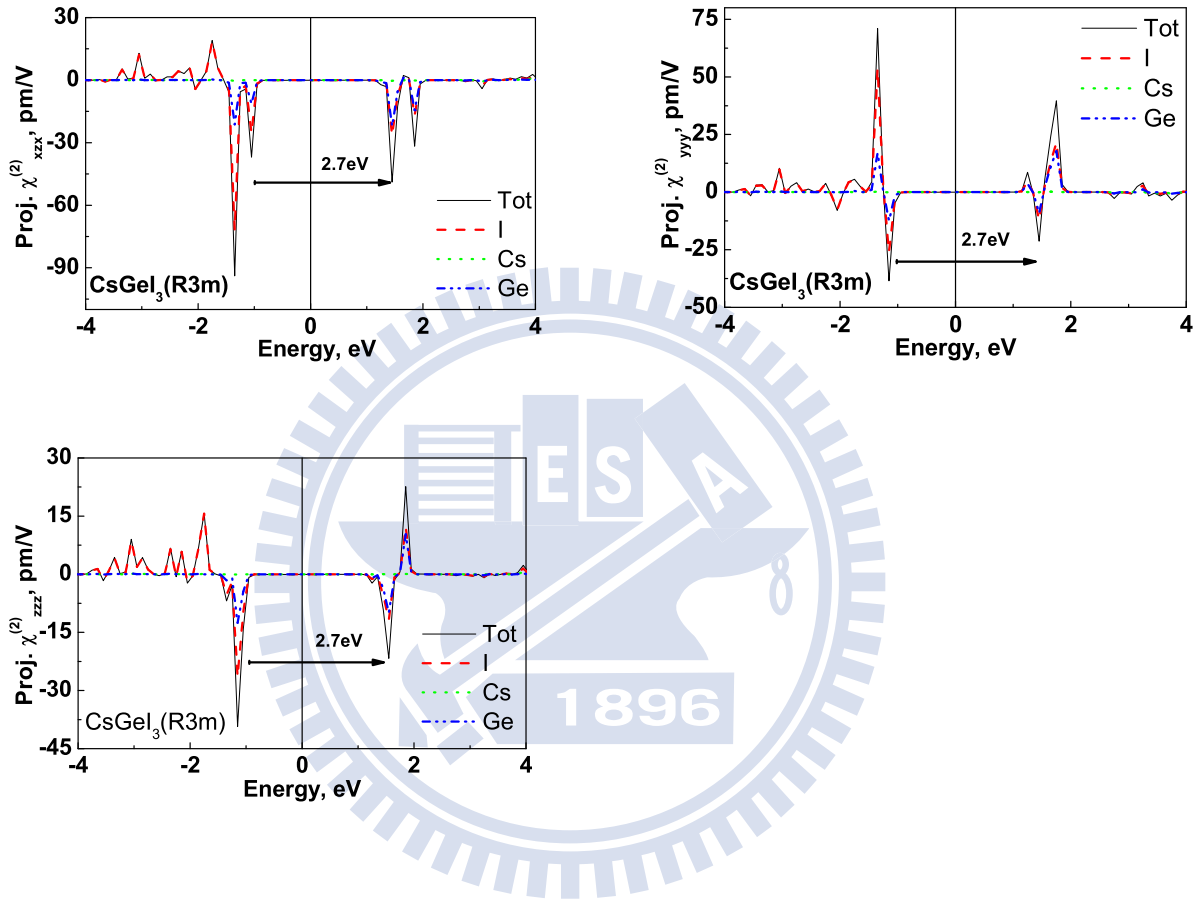


圖 3.20: Second-order nonlinear optical susceptibility of components of rhombohedral  $\text{CsGeI}_3$  projected for various atomic species and energy bands using eq. 2.25. The contribution of each species is projected to  $\chi_{xzx}^{(2)} (= \chi_{zxx}^{(2)})$ ,  $\chi_{yyy}^{(2)}$ , and  $\chi_{zzz}^{(2)}$  in  $\text{CsGeI}_3$ . Absolute value of SHG susceptibility  $\chi_{xyz}^{(2)}(\omega; \omega, 0)$ , solid line for  $\text{CsGeI}_3$ .

## Chapter 4

# Chalcopyrite-like compounds with tetrahedron distortions and their optical properties



### 4.1 Nonlinear optical crystals $AgGa(S_xSe_{1-x})_2$

As grown crystals up to 10mm in diameter and 5cm in length can routinely be prepared. All grown samples are single crystals, which exhibit various colours from yellow ( $AgGaS_2$ ) through red  $AgGa(S_xSe_{1-x})_2$  to black ( $AgGaSe_2$ ). Figure 4.2 show the absorption edge of the resulting



crystals.

#### 4.1.1 Crystal structure and mechanical properties

X-ray diffraction (XRD) patterns (fig. 4.1) show that the substitution-related diffraction peaks, e.g. [112] plane around  $2\theta \approx 26^\circ$  or [312] plane about  $2\theta \approx 52^\circ$ , are shifted gradually with substitution composition. From the crystal models used in this study, the *S* and *Se* atoms are located between these atomic planes. The substitution of *S* with *Se* atoms causes the change of interplanar spacing. The peak from [312] planes is found to achieve a minimum peak height when *S* and *Se* are 50% occupied. The *S* and *Se* atoms randomly occupy the crystallographic sites between the [312] planes, which cause a reduction in structural factor. The lattice parameters of  $AgGa(S_xSe_{1-x})_2$  crystals vary linearly with *x* by  $a = b \cong (5.99 - 0.55x)\text{\AA}$ ,  $c \cong (10.87 - 0.57x)\text{\AA}$ . This also generates a linear dependence of the cell volume on *x* with:  $V \cong (387.88 - 54.50x)\text{\AA}^3$ .

We summarize the calculated lattice properties of five crystals in Table 4.3 and Table 4.2 . Note that the tetrahedral coordination of *S* and/or *Se* atoms can be distorted by the presence of two types of metal-*S*

and/or metal-*Se* bonds. The average bond length is calculated to be  $Ga-S(2.17\text{\AA}-2.15\text{\AA})$ ,  $Ga-Se(2.30\text{\AA}-2.26\text{\AA})$ ,  $Ag-S(2.64\text{\AA}-2.59\text{\AA})$ , and  $Ag-Se(2.70\text{\AA}-2.65\text{\AA})$ . These results agree with the notion that stronger bonding between (*Ag*, *Ga*) and (*S*, *Se*) atoms leads to a shorter bond length in  $AgGa(S_xSe_{1-x})_2$  crystals with increasing *S* (*x*) composition. The calculated structural parameters are in good agreement with experimental values of  $AgGaSe_2$ , reported by Jaffe *at el* [49, 50] and this work. The slight underestimate of the lattice constants is attributed to the intrinsic nature of density functional theory (DFT). Our calculated structures of  $AgGa(S_xSe_{1-x})_2$  appear to be more distorted than the observed structure, which reflect in a larger value of the bond-length mismatch parameter *u* (table 4.3). The calculated values of  $AgGa(S_xSe_{1-x})_2$  crystals are about 0.3 with the supercell-models. The *u*-parameters yielded from the supercell-models are consistently higher than those with the single-unit-cell-models (about 0.29) and the experimental values of  $AgGa(S_xSe_{1-x})_2$ , reported by Jaffe *at el* (about 0.27). In Table 4.3, we also present the calculated bandgap for the  $AgGa(S_xSe_{1-x})_2$  crystals. The calculated bandgap show in Figure 4.3 is found to be proportional to the composition of *S* but inversely proportional to the cell-volume.

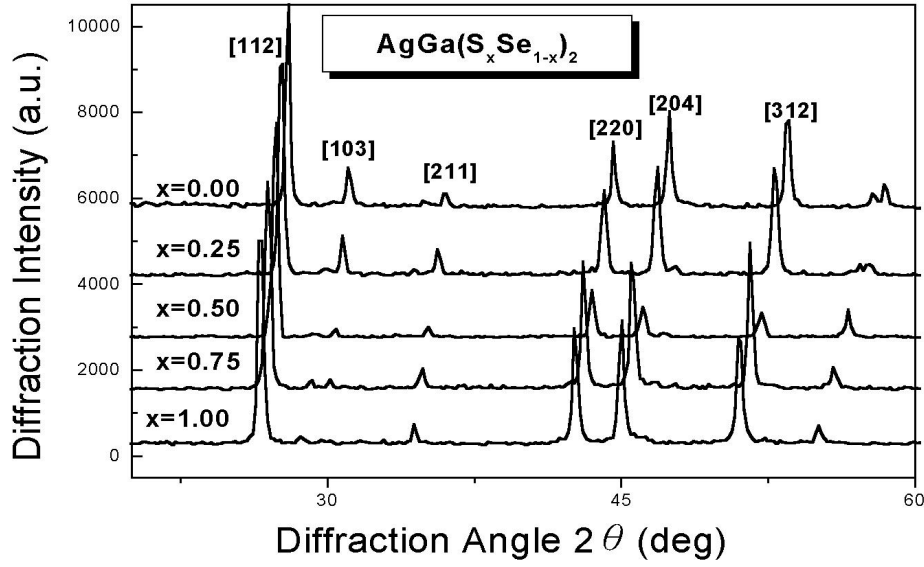


圖 4.1: X-ray powder diffraction of the NLO crystals  $AgGa(S_xSe_{1-x})_2$ . It is shown that the XRD peaks shift with S composition. A minimum peak height at [312] is observed when the S and Se was half substitution in the NLO crystals  $AgGa(S_xSe_{1-x})_2$ . From the DFT calculations, the equation-of-state parameters such as the bulk modulus and its pressure derivative can be deduced. The results are also summarized in Table 4.3. The bulk modulus for  $AgGaS_2$  is about 9.11 GPa. It is decreased to 8.15 GPa for  $AgGa(S_xSe_{1-x})_2$  and 7.31 GPa for  $AgGaSe_2$ . This tendency is consistent with the trend of a decreasing bonding strength (larger unit cell volume) and a narrower band gap.

### 4.1.2 Electronic structures, density of states, and optical spectrum

In Fig. 4.2, absorption spectra measured on single crystal  $AgGa(S_xSe_{1-x})_2$  in visible light range are shown. The absorption edge is found to increase from 1.7 eV to 2.64 eV with the composition of Sulfur. Photoluminescence (PL) spectra (fig. 4.3) reveal a similar trend of x-dependence. From PL measurements at room temperature, the band gap values of  $AgGa(S_xSe_{1-x})_2$  crystals can be fitted to  $E_{PL}(x) \cong (1.76 + 0.65x)$ eV. The experimental data taken from Matsushita *et al*[3] and ours lie between the calculated band-gap values with the single-unit-cell model and the supercell model. The resulting bandgap of  $AgGa(S_xSe_{1-x})_2$  can be tuned linearly in a wide spectral range by adjusting substitution composition. Furthermore, these crystals are all direct band-gap (see Figure 4.4) with potential applications as efficient absorber or photon emitter.

To gain more insight into the calculated optical properties we further studied the PDOS and LDOS spectra of these crystals. The calculated PDOS for  $AgGa(S_xSe_{1-x})_2$  are presented in Fig. 4.5. We found that the valence band maximums (VBM) of  $AgGa(S_xSe_{1-x})_2$  is mainly con-

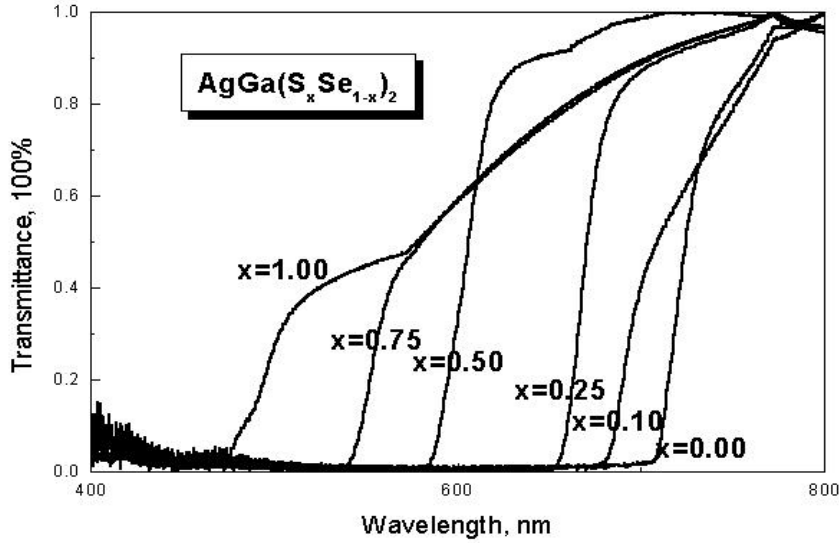


圖 4.2: Absorption edge measurements of the NLO crystals  $AgGa(S_xSe_{1-x})_2$ .

tributed by the (3)*p*-orbital of *S* and (4)*p*-orbital of *Se* atoms. However the roles played by *S* or *Se* atoms at the band edges can not be distinguished. Their contribution to the total density of states is a simple weighted summation over *S* and *Se* compositions (see fig. 4.5(*f*)). The substitution effect of the *S* or *Se* in  $AgGa(S_xSe_{1-x})_2$  crystal mainly shows up via the influences of cell-volume change. Based on this finding, we are expected to see some correlated behaviors such as a linear variation of *x* in  $AgGa(S_xSe_{1-x})_2$  shall cause a linear compression in cell volume, the band gap shall increase linearly, and the second-

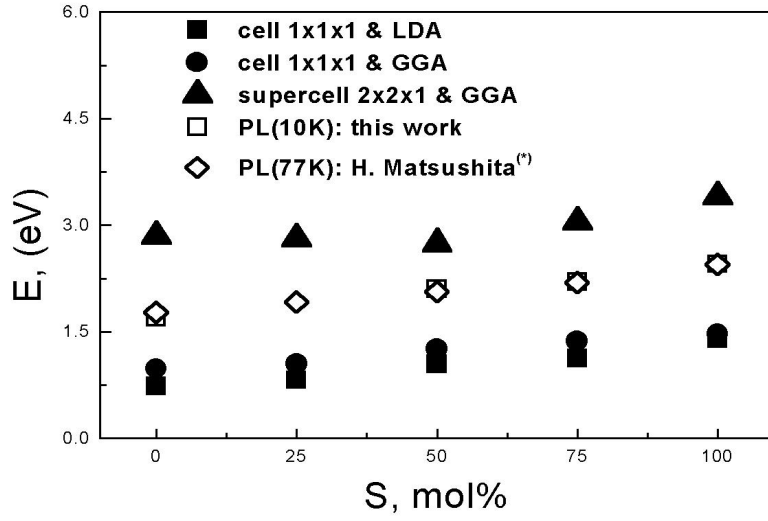


圖 4.3: The first-principles calculated bandgaps and photo-luminescence measurements of the NLO crystals  $AgGa(S_xSe_{1-x})_2$ . (\*): ref.[3]

order NLO susceptibility,  $\chi^{(2)}$ , shall decrease with the cubic power of bandgap [4]. We also test the concept by performing first-principles calculation on a series of artificial structures prepared by expanding the cell volume of  $AgGaS_2$  and compressing that of  $AgGaSe_2$ . The calculated results clearly show that the similar tendency on the band gap and the related optical properties. This finding agrees with an empirical rule proposed by Vegard, which states that the change of material properties caused by substitution can be calculated by simply taking

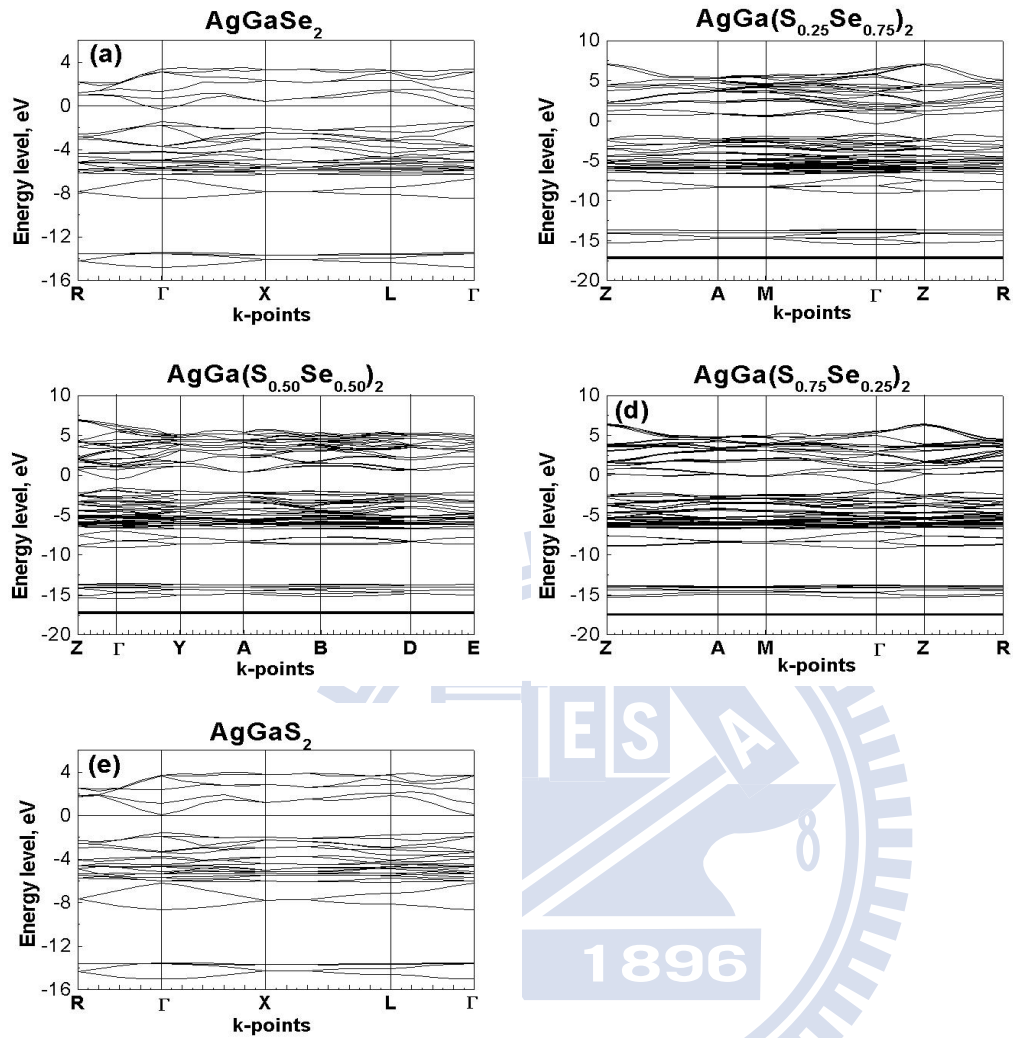


圖 4.4: Band structures of the NLO crystals  $\text{AgGa}(\text{S}_x\text{Se}_{1-x})_2$

a composition-weighted average of the pure substances, here are the  $\text{AgGaS}_2$  and  $\text{AgGaSe}_2$  [112, 113].

Our FTIR measurements show that the long wavelength limit of the transparent range of the crystals exhibits a similar dependence on substitution composition. Crystal  $\text{AgGaS}_2$  has an infrared cut-off wave-

length at ( $\sim 12\mu m$ ), which is shorter than the cut-off value of  $AgGaSe_2$  ( $\sim 18\mu m$ ). The infrared absorption edge of  $AgGa(S_xSe_{1-x})_2$  with  $x=0.25, 0.5, 0.75$  lies between  $\sim 13\mu m - \sim 15\mu m$ . This result is reasonable in view of the fact that Se atom is heavier than S and the infrared absorption edge is dominated by the stretching modes of the  $S, Se$ -metal bonds.

#### 4.1.3 Second-order nonlinear optical susceptibilities

It is well known that second-order nonlinear optical susceptibility is much more sensitive to crystal structure than linear optical susceptibility. We therefore calculate second-order nonlinear susceptibilities in order to learn more about the substitution-induced distortion. The results are summarized in the end of Table 4.3 and Table 4.2. To avoid unnecessary complication from dispersion and resonant effects, we use Eq. (2.29) to calculate the static second-harmonic susceptibility (the zero-frequency limit) of the  $AgGa(S_xSe_{1-x})_2$  crystals. For chalcopyrites, only two independent components, the 123 and 312 components, of  $\chi^{(2)}$  exist, where 1, 2, and 3 refer to the x, y, and z directions along the cubic axes, respectively [114]. However for the case with input



photon frequency far below the material absorption edge, these two components are essentially equal according to the Kleinman symmetry. For these materials, the calculated  $\chi_{123}^{(2)}$  is negative with a magnitude lying between -22.07pm/V and -51.21pm/V for  $AgGa(S_xSe_{1-x})_2$  with the supercell model. No any band-gap correction scheme was employed. These  $\chi_{123}^{(2)}$  values agree very with the experimental results of  $AgGaS_2$  and  $AgGaSe_2$ [57]. With the single-unit-cell model, the calculated  $\chi_{123}^{(2)}$  ranges from -47.07pm/V to -140.411pm/V with different x. These values are about two times larger than the calculated ones with the supercell model. Note that the nonlinearity of material is inversely proportional to the cubic power of the bandgap. We use this simple scaling rule to remove bandgap influence on the second-order nonlinearity. The result is presented in Fig. 4.6. Here  $AgGaS_2$  is used as the reference and the cubic power scaling rule is employed to predict the optical nonlinearity of other crystals. This is labeled as the scaled  $\chi_{123}^{(2)}$  value (filled symbols) and is compared to the first-principles calculation results (open symbols) with the single-unit-cell model. As it is shown in Fig. 4.6 that the deviation can be as large as 20% at  $x=0.25$ . The difference is most likely originated from the transition moment products, which are known to be sensitive to the detailed arrangement of unit

cell.

## 4.2 Innovative Wide Bandgap Materials: the Ternary Nitrides, and their Optical properties

In this section, structural properties and the fundamental electronic and optical properties of the  $A^{II}B^{IV}N_2$  ( $A^{II}=\text{Be, Mg}; B^{IV}=\text{C, Si, Ge}$ ) compounds are presented.

The aim of our work is to use the *ab initio* method to calculate electronics and optical properties of  $A^{II}B^{IV}N_2$  ( $A^{II} = \text{Be, Mg}, B^{IV} = \text{C, Si, Ge}$ ) ternary compounds, and to determine their prospects for applications.

### 4.2.1 Hexagonal and Tetragonal Ternary Nitrides

In Table 4.3(<sup>a</sup>: Ref. [115, 116, 117, 118, 119]) , six compounds were considered. The parameter  $\eta$  in Berium ternary nitrides increases as the

B-site cation goes from Carbon to Germanium. However, the variation in parameter  $\eta$  is not monotonic in Magnesium ternary nitrides.

#### 4.2.2 Electronic and optical properties

Band structures and optical properties of  $A^{II}B^{IV}N_2$  ( $A^{II}=\text{Be, Mg}$ ;  $B^{IV}=\text{C, Si, Ge}$ ) compounds were calculated for the stable designed phase, chalcopyrite, by the Linear Augmented Slater-Type Orbitals (LASTO) method.[51, 52, 53, 54, 55] The self-consistent procedure was performed on a grid of 1000 k-points uniformly distributed in the irreducible tetragonal BZ. The band structures obtained with the LASTO method are almost identical to those obtained with the *WIEN2K* package. However, the LASTO method is more efficient and allows the computation of  $\chi_{abc}^{(2)}(-2\omega : -\omega, -\omega)$ .

Figure 4.7 shows the electronic band structures for  $A^{II}B^{IV}N_2$  ( $A^{II}=\text{Be, Mg}$ ;  $B^{IV}=\text{C, Si, Ge}$ ) obtained by using the LASTO package. The electronic band structures of both chalcopyrite and orthorhombic  $\text{ZnGeN}_2$  are also calculated in Fig. 4.8, and are compared with Fig. 4.7. Figure

4.9 shows the corresponding projected density of states (PDOS). The calculated bandgaps vary from 2.68 eV (*BeGeN<sub>2</sub>*) to 4.24 eV (*MgCN<sub>2</sub>*), which are listed in the first row in Table 4.4. Because of the underestimation in bandgap in the DFT scheme, these results should be adjusted to the higher values, from  $\approx 4$  eV to  $\approx 6$  eV.

Figures 4.11 and 4.12 show the frequency-dependent second-order optical susceptibilities of  $A^{II}B^{IV}N_2$  compounds. It is found that *BeGeN<sub>2</sub>* has the largest value among these chalcopyrite ternary nitrides. These frequency-dependent  $\chi_{xyz}^{(2)}$  and  $\chi_{zxy}^{(2)}$  oscillate violently around band-edges, especially for *BeGeN<sub>2</sub>* and *MgGeN<sub>2</sub>*. Besides, the nonvanishing static  $\chi_{xyz}^{(2)}$  and  $\chi_{zxy}^{(2)}$  are shown in the fourth and fifth columns, respectively in Table 4.4. The magnitudes of  $\chi_{xyz}^{(2)}$  of *BeGeN<sub>2</sub>* and *MgGeN<sub>2</sub>* are significant, i.e. 18.45 pm/V and 16.78 pm/V, respectively. This can be attributed to the smaller bandgaps in these  $ABN_2$  compounds. However, the larger bandgap *MgCN<sub>2</sub>* has a similar  $\chi_{xyz}^{(2)}$ , i.e. 16.19 pm/V. It implies that *MgCN<sub>2</sub>* has larger oscillator strengths. We also calculated the frequency-dependent  $\chi_{xyz}^{(2)}$  for *ZnGeN<sub>2</sub>* for both I-42d and Pna21

structures, which are shown in Fig. 4.13. The static  $\chi_{yyz}^{(2)}$  and  $\chi_{zzz}^{(2)}$  are 6.33 pm/V and 13.40 pm/V, respectively (see Table 4.4). They are smaller than those values in chalcopyrite  $A^{II}B^{IV}N_2$  compounds, and are smaller than the  $\chi_{xyz}^{(2)}$  and  $\chi_{zxy}^{(2)}$  of chalcopyrite  $ZnGeN_2$  (16.13 pm/V and 23.69 pm/V). However, the bandgaps (1.54 eV for I-42d and 1.66 eV for Pna21) of  $ZnGeN_2$  are smaller than those of  $A^{II}B^{IV}N_2$  compounds that could limit their applications in ultra-violet range.

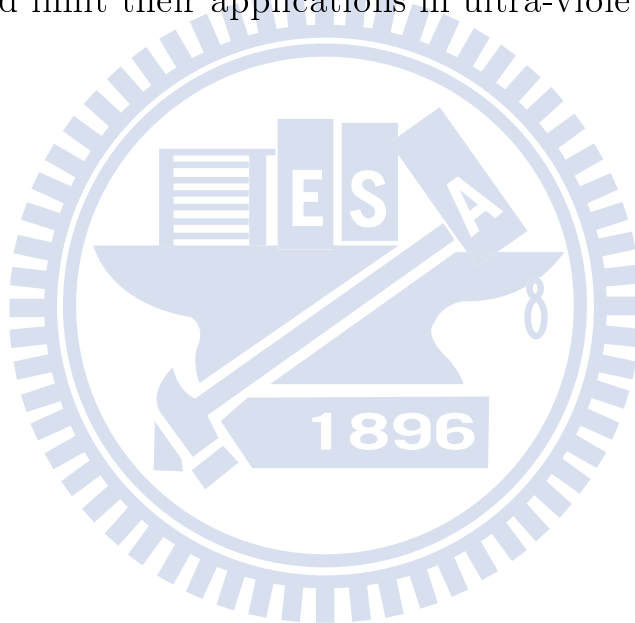


表 4.1: Structural parameters, bond-lengths, and bulk modulus of the NLO crystals  $AgGa(S_xSe_{1-x})_2$ . The calculated values are obtained via first-principles calculation with the supercell model.

	$x=0.00$	$x=0.25$	$x=0.50$	$x=0.75$	$x=1.00$
$a(\text{\AA})(\text{exp.})$	5.97	5.92	5.86	5.80	5.74
$a(\text{\AA})(\text{calc.})$	5.87	5.89	5.77	5.66	5.63
$c(\text{\AA})(\text{exp.})$	10.88	10.73	10.57	10.42	10.26
$c(\text{\AA})(\text{calc.})$	10.64	10.60	10.24	10.09	10.02
$Ga - S(\text{\AA})(\text{calc.})$		2.17	2.14	2.14	2.15
$Ga - Se(\text{calc.})$	2.30	2.29	2.27	2.26	
$Ag - S(\text{\AA})(\text{calc.})$		2.64	2.60	2.59	2.59
$Ag - S(\text{\AA})e(\text{calc.})$	2.70	2.68	2.67	2.65	
$\eta(\text{exp.})$	1.79	1.80	1.80	1.81	1.82
$\eta(\text{calc.})$	1.81	1.87	1.84	1.85	1.84
$u[S](\text{calc.})$		0.32	0.32	0.32	0.32
$u[Se](\text{calc.})$	0.31	0.31	0.31	0.31	
$B_o(\text{GPa})(\text{calc.})$	7.31	7.71	8.15	8.64	9.11
$\chi_{123}^{(2)}(\text{pm/V})(\text{calc.})$	-51.21	-43.31	-32.14	-26.08	-22.07

表 4.2: Structural parameters and bond-lengths of the NLO crystals  $AgGa(S_xSe_{1-x})_2$ , which are obtained via first-principles calculation with the single-unit-cell model.

	$x=0.00$	$x=0.25$	$x=0.50$	$x=0.75$	$x=1.00$
$a(\text{\AA})$	5.87	5.89	5.81	5.73	5.63
$c(\text{\AA})$	10.78	10.32	10.25	10.15	10.17
$Ga - S(\text{\AA})$		2.34	2.30	2.29	2.31
$Ga - Se(\text{\AA})$	2.44	2.43	2.41	2.40	
$Ag - S(\text{\AA})$		2.61	2.57	2.55	2.58
$Ag - Se(\text{\AA})$	2.67	2.65	2.63	2.65	
$\eta$	1.81	1.79	1.78	1.75	1.84
$u[S]$		0.29	0.29	0.29	0.29
$u[Se]$	0.28	0.28	0.28	0.29	
$\chi_{123}^{(2)}(pm/V)(calc.)$	-140.41	-107.03	-67.90	-54.22	-47.07

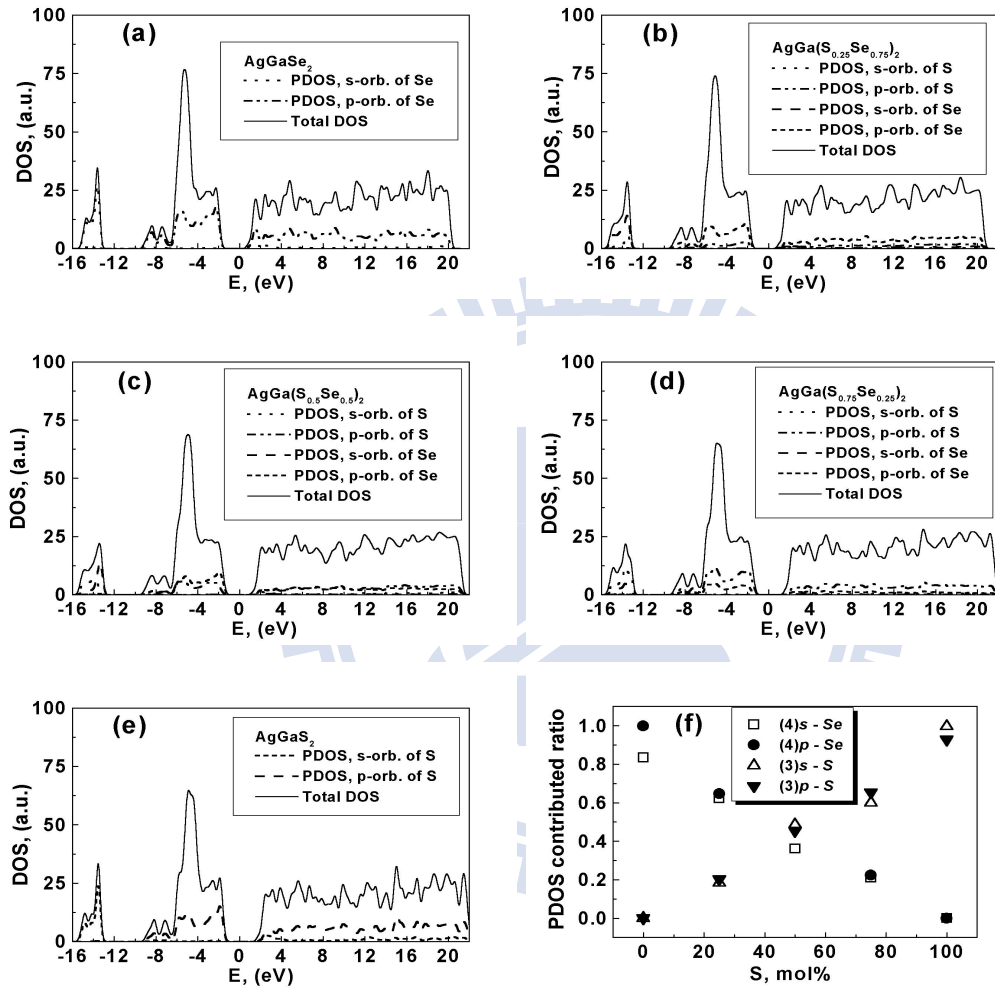


圖 4.5: Analysis of partial density of states (PDOS) of s- and p-orbital contribution via S and Se in the NLO crystals  $AgGa(S_xSe_{1-x})_2$



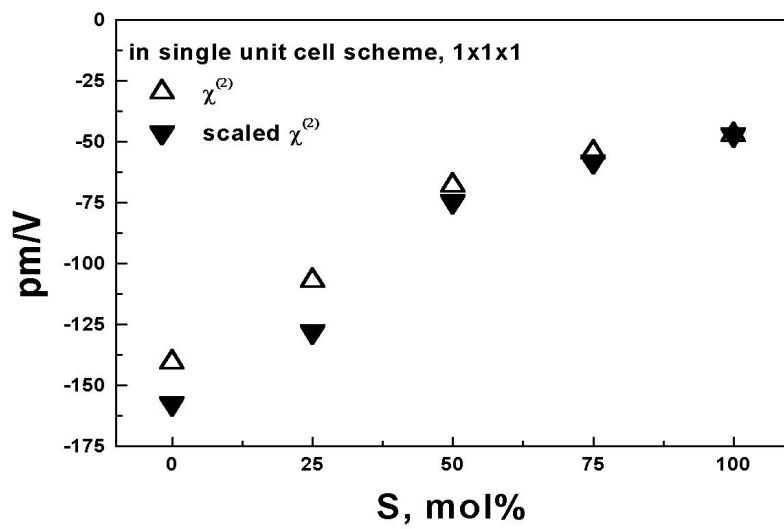


圖 4.6: The first-principles calculation of the second-harmonic susceptibility  $\chi^{(2)}$  and the scaled values of  $\chi^{(2)}$  of the NLO crystals  $AgGa(S_xSe_{1-x})_2$ . The scaled  $\chi^{(2)}$  values are estimated from that of the  $AgGaS_2$  with a cubic power of  $E_g$

表 4.3: The structural parameters of the NLO crystals  $A^{II}B^{IV}N_2$ .

	$a(\text{\AA})$	$b(\text{\AA})$	$c(\text{\AA})$	$A^{II} - N(\text{\AA})$	$B^{IV} - N(\text{\AA})$	$\eta$	$u$
BeCN <sub>2</sub>	3.710		7.272	1.7104	1.4957	0.98	0.47
BeSiN <sub>2</sub>	4.100		8.364	2.1681	1.5320	1.02	0.62
BeGeN <sub>2</sub>	4.250		9.320	2.2877	1.6446	1.10	0.62
MgCN <sub>2</sub>	4.110		7.562	1.9181	1.5800	0.92	0.51
MgSiN <sub>2</sub>	4.602		7.912	2.1150	1.7280	0.86	0.52
MgGeN <sub>2</sub>	4.690		9.890	2.2399	1.9228	1.05	0.49
BeSiN <sub>2</sub> <sup>ref.[115]</sup>	4.073		8.164			1.00	
BeSiN <sub>2</sub> ,Pna21 <sup>ref.[115]</sup>	4.939	5.697	4.639				
BeSiN <sub>2</sub> ,Pna21 <sub>exp</sub> <sup>ref.[116]</sup>	4.977	5.747	4.674				
BeGeN <sub>2</sub> <sup>g</sup>	4.225		8.531			0.98	
BeGeN <sub>2</sub> ,Pna21 <sup>ref.[115]</sup>	5.105	5.856	4.803				
ZnGeN <sub>2</sub>	4.523		8.608	2.0388	1.8272	0.95	0.45
ZnGeN <sub>2</sub> ,Pna21	5.384	6.379	5.144				
ZnGeN <sub>2</sub> <sup>ref.[115]</sup>	4.615		8.902			0.96	
ZnGeN <sub>2</sub> ,Pna21 <sup>ref.[115]</sup>	5.402	6.351	5.149				
ZnGeN <sub>2</sub> ,Pna21 <sub>exp</sub> <sup>ref.[117]</sup>	5.518	6.372	5.174				
ZnGeN <sub>2</sub> ,Pna21 <sub>exp</sub> <sup>ref.[118]</sup>	5.500	6.440	5.140				
ZnGeN <sub>2</sub> ,Pna21 <sub>exp</sub> <sup>ref.[119]</sup>	5.454	6.441	5.194				
ZnGeN <sub>2</sub> ,Pna21 <sub>exp</sub> <sup>ref.[119]</sup>	5.565	6.426	5.191				

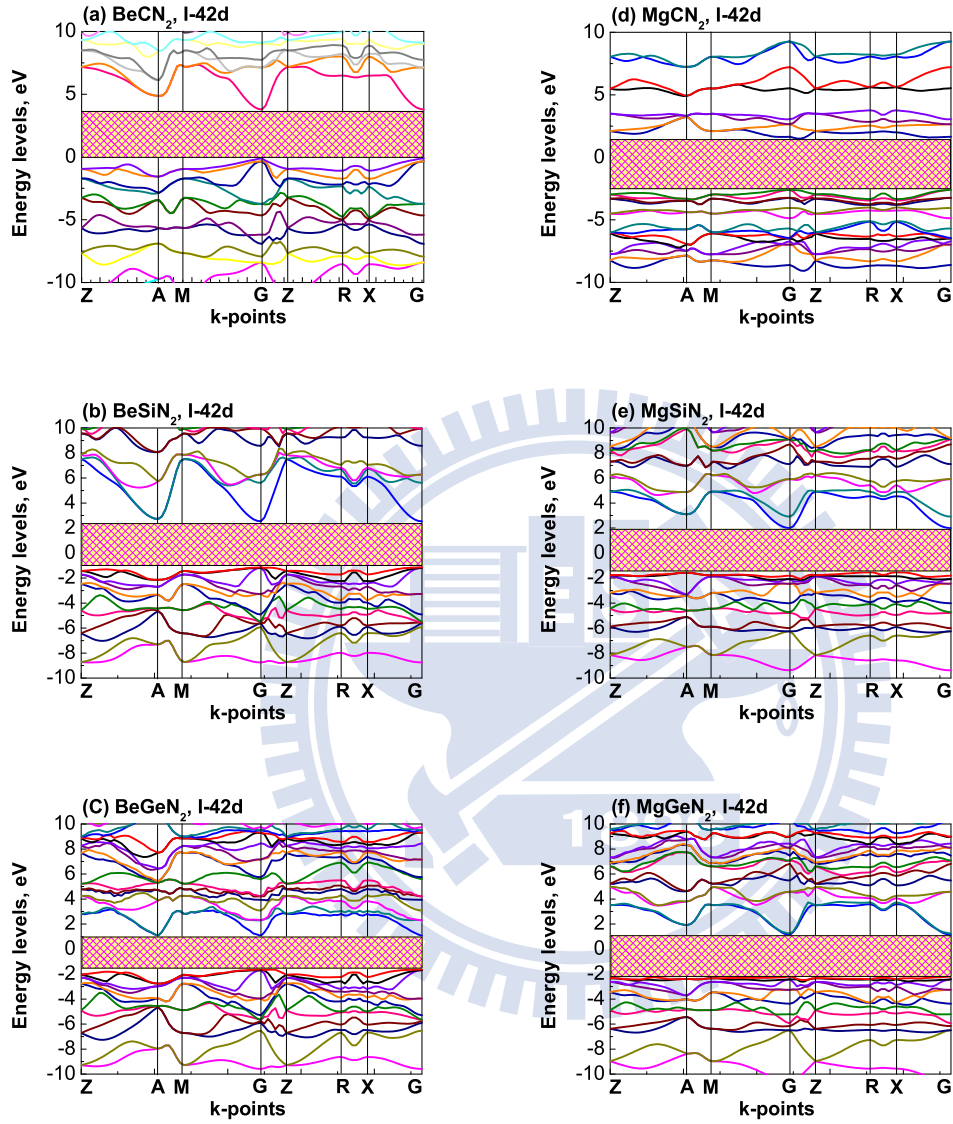


圖 4.7: Electronic band-structures of various chalcopyrite  $A^{II}B^{IV}N_2$  ( $A^{II}=\text{Be, Mg}$ ;  $B^{IV}=\text{C, Si, Ge}$ ) with space group symmetry I-42d (no. 122). They are (a)  $BeCN_2$ ; (b)  $BeSiN_2$ ; (c)  $BeGeN_2$ ; (d)  $MgCN_2$ ; (e)  $MgSiN_2$ ; and (f)  $MgGeN_2$ .

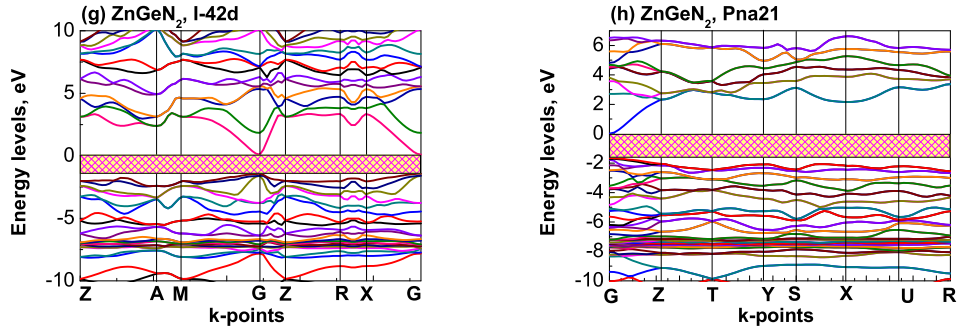


圖 4.8: The band-structures of (a) chalcopyrite  $ZnGeN_2$  and (b) orthorhombic  $ZnGeN_2$ .

表 4.4: The calculated bandgap values and optical susceptibilities in zero frequency of the NLO crystals  $A^{II}B^{IV}N_2$  by using first-principle calculation.

	$E_g, eV$	$\chi_{xx}^{(1)}$	$\chi_{zz}^{(1)}$	$\chi_{xyz}^{(2)}$	$\chi_{zxy}^{(2)}$	
$BeCN_2$	3.90	1.61	1.64	12.49	12.62	this work
$BeSiN_2$	3.67	1.55	1.56	6.45	6.47	this work
$BeGeN_2$	2.68	1.70	1.70	18.45	15.02	this work
$MgCN_2$	4.24	2.02	2.23	16.19	15.07	this work
$MgSiN_2$	3.79	1.54	1.59	8.39	7.68	this work
$MgGeN_2$	3.33	1.62	1.68	16.78	15.24	this work
$ZnGeN_2$	1.54			16.13	23.69	this work
$ZnGeN_2, Pna21$	1.66			6.33	13.40	this work
$ZnGeN_2, Pna21$	1.67					Ref. [115]

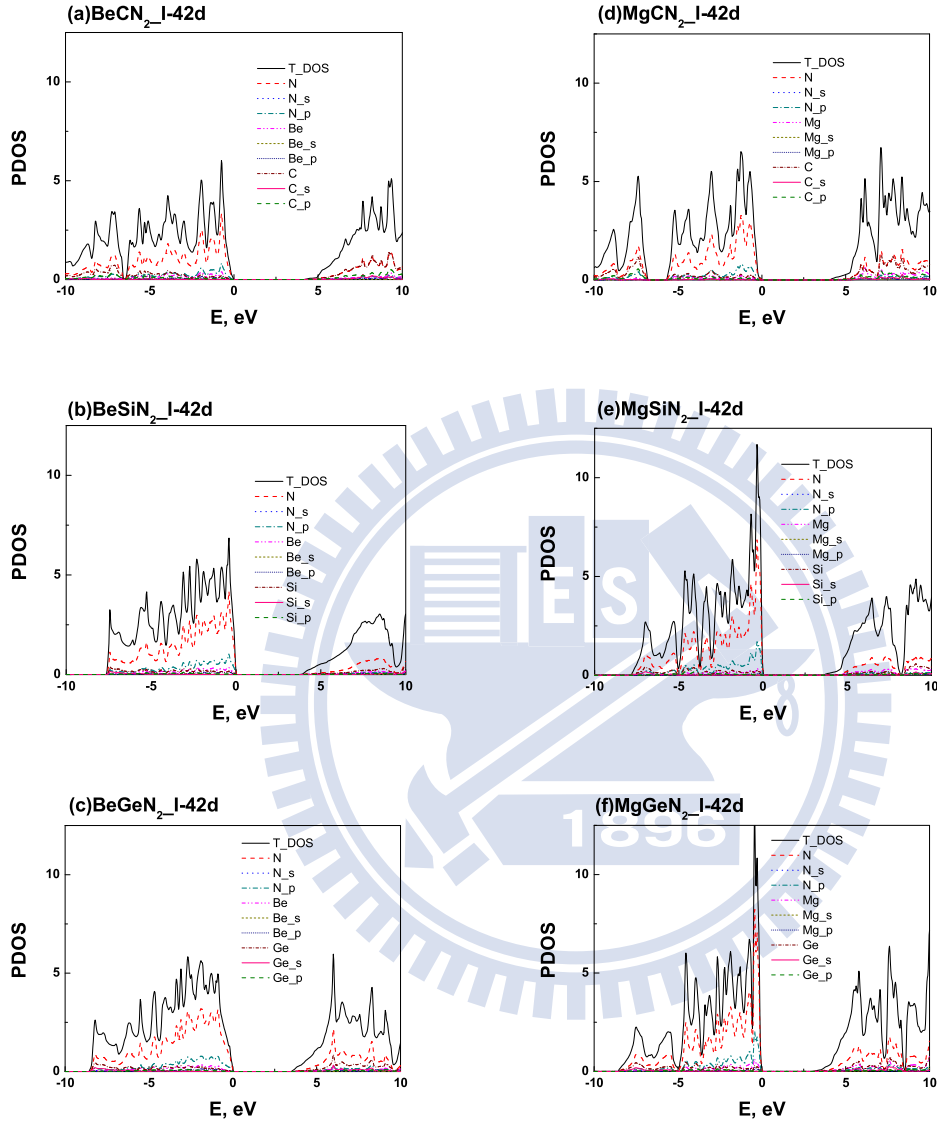


圖 4.9: Density of State of various chalcopyrite  $A^{II}B^{IV}N_2$  ( $A^{II}$ =Be, Mg;  $B^{IV}$ =C, Si, Ge) with space group symmetry I-42d (no. 33). They are (a) $BeCN_2$ ; (b) $BeSiN_2$ ; (c) $BeGeN_2$ ; (d) $MgCN_2$ ; (e) $MgSiN_2$ ; and (f) $MgGeN_2$ .

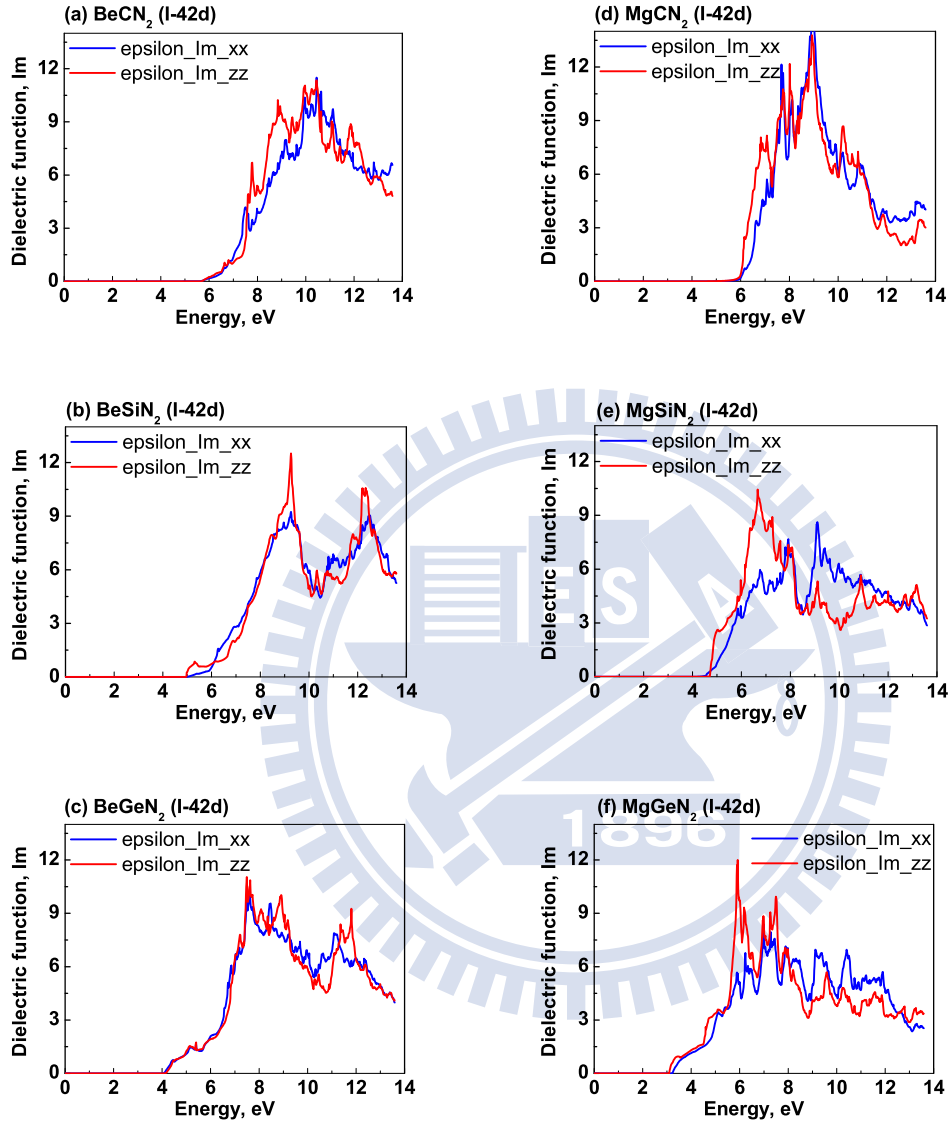


圖 4.10: Dielectric functions of various tetragonal  $A^{II}B^{IV}N_2$  ( $A^{II}=\text{Be, Mg}$ ;  $B^{IV}=\text{C, Si, Ge}$ ) with space group symmetry I-42d (no. 122). They are (a)  $\text{BeCN}_2$ ; (b)  $\text{BeSiN}_2$ ; (c)  $\text{BeGeN}_2$ ; (d)  $\text{MgCN}_2$ ; (e)  $\text{MgSiN}_2$ ; and (f)  $\text{MgGeN}_2$ .

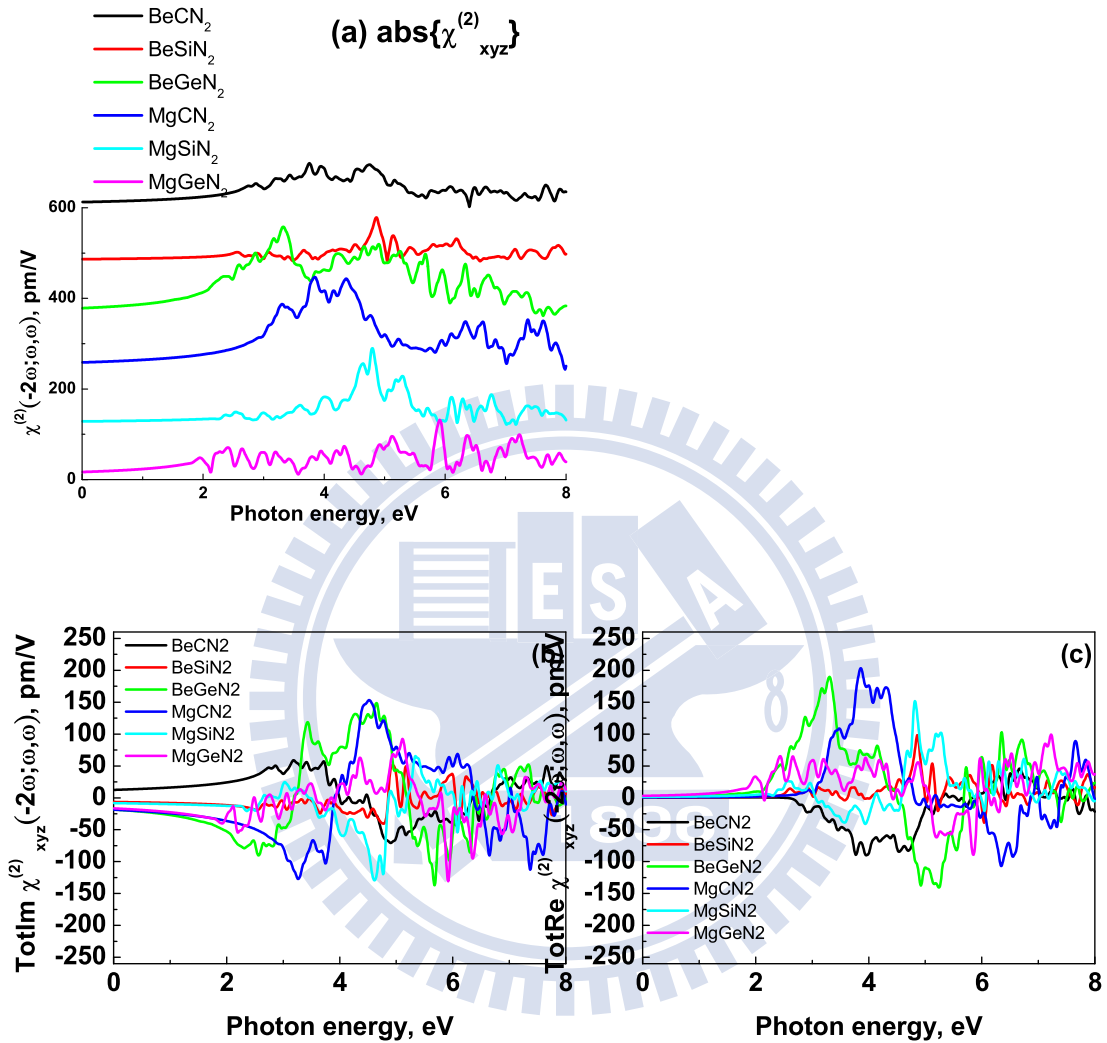


圖 4.11: Frequency-dependent second order nonlinear susceptibilities of various tetragonal  $A^{II}B^{IV}N_2$  ( $A^{II}=\text{Be, Mg}$ ;  $B^{IV}=\text{C, Si, Ge}$ ) with space group symmetry I-42d (no. 122). They are (a) Total  $\chi_{xyz}^{(2)}(-2\omega; \omega, \omega)$  responses; (b) Totally imaginary  $\chi_{xyz}^{(2)}(-2\omega; \omega, \omega)$  responses; (c) Totally real  $\chi_{xyz}^{(2)}(-2\omega; \omega, \omega)$  responses;

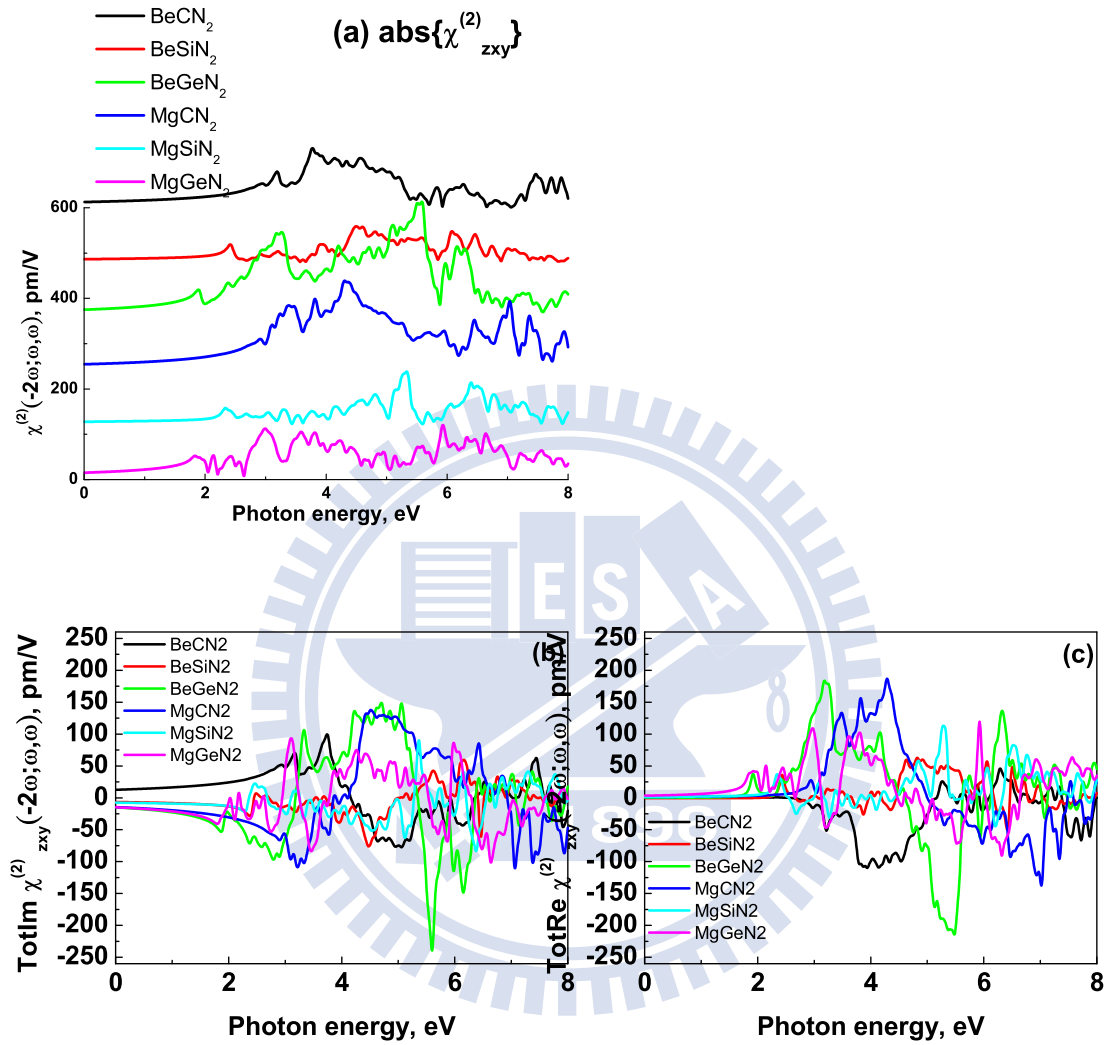


圖 4.12: Frequency-dependent second order nonlinear susceptibilities of various tetragonal  $A^{II}B^{IV}N_2$  ( $A^{II}=\text{Be, Mg}$ ;  $B^{IV}=\text{C, Si, Ge}$ ) with space group symmetry I-42d (no. 122). They are (a) Total  $\chi_{zxy}^{(2)}(-2\omega; \omega, \omega)$  responses; (b) Totally imaginary  $\chi_{zxy}^{(2)}(-2\omega; \omega, \omega)$  responses; (c) Totally real  $\chi_{zxy}^{(2)}(-2\omega; \omega, \omega)$  responses.



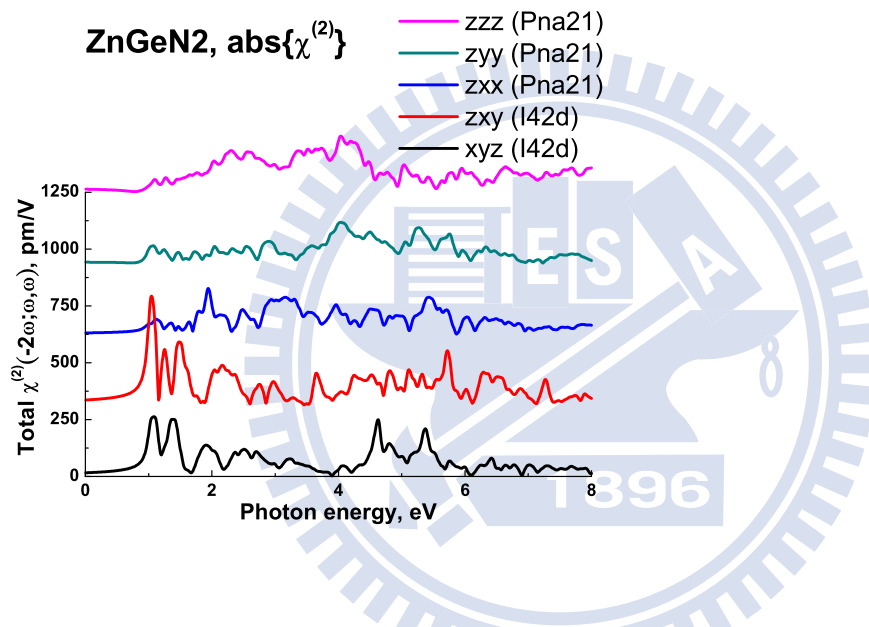


圖 4.13: Absolute values of frequency-dependent second order nonlinear susceptibilities for both structures I-42d and Pna21.

# Chapter 5

## Conclusion

The optoelectronic properties of the rhombohedral ternary halides ( $ABX_3$  ( $A=Cs, Rb, B=Ge, X=Cl, Br, I$ )), the wide-bandgap ternary nitrides ( $A^{II}B^{IV}N_2$  ( $A^{II} = Be, Mg, B^{IV} = C, Si, Ge$ )), and chalcopyrite  $AgGaS_2$ ,  $AgGaSe_2$ , and  $AgGa(S_xSe_{1-x})_2$  have been systematically studied. Their microstructures, electronic structures, linear- and nonlinear-optical properties of the crystals with two main polyhedron categories are examined in this study by using both the first principles calculation and the experimental methods.

First of all, direct effects of structural distortion and electronic properties for linear and second-order optical response in  $CsGeX_3$  based

on first-principles electronic structure calculations are presented. A response formalism that is free of any unphysical divergences are employed at zero frequency, we obtain reasonable agreement with experiment for  $\chi_{xyz}^{(2)}(\omega; \omega, 0)$  in the low-frequency regime. The SHG susceptibility has been presented and it shows important differences from other theoretical calculations. The lack of experimental data, as well as its contradictory nature, prevents any conclusive comparison with experiment over a large energy range. The structural deformed factors,  $\Delta\alpha$ ,  $d_{Ge}$ ,  $d_X$  are proposed to describe the degree of the distortion from an ideal perovskite structure.  $\Delta\alpha$  and  $d_{Ge}$  increase while  $d_X$  decrease when the halide anions are changed from Cl (3.67eV) to I (1.53eV). The direct structural distortion effect on these rhombohedral CGXs are analysed via the first-principles calculations. The dielectric function and the second harmonic generation response coefficient behave in the same manner as  $\Delta\alpha$  and  $d_{Ge}$ . The direct bandgaps,  $E_G$ , of CsGeX<sub>3</sub> all occur at the  $R$ -point,  $\Delta E_R$ . The bandgap values of CGX become smaller, i.e.  $E_G^{CGC} > E_G^{CGB} > E_G^{CGI}$  as the  $\Delta\alpha$  and  $d_{Ge}$  increase, i.e.  $d_{Ge}^{CGC} < d_{Ge}^{CGB} < d_{Ge}^{CGI}$ . Partial density of states (PDOS) analysis reveals that the valence band maximum (VBM) and conduction band minimum (CBM) are mainly contributed from the p-orbitals of germanium.

Species-projected contributions to  $\chi_{ijk}^{(2)}(\beta, E)$  in CGX are affected by both the structural distortion and the electronic band structures. The projection technique successfully differentiated the electronic and structural contributions. The magnitudes of  $\chi_{ijk}^{(2)}$  are in agreement with some reported experiment near the band gap. In summary, we found that the lattice distortion parameters play key roles in determining the linear and nonlinear optical responses of CGX crystals.

According to the powder X-ray diffraction pattern and powder SHG results, an innovative infrared nonlinear optical crystal  $CsGeBr_3$ , which was characterized as a rhombohedral crystal structure, was synthesized. *Ab initio* calculations on  $CsGeBr_3$  were also carried out to analyze the related electronic and optical properties. Space group symmetry of rhombohedral  $CsGeBr_3$  was found to be  $R3m$  (No. 160) and had no inversion center. The reflection powder second harmonic generation measurement of CGBr also showed that its nonlinear optical efficiency was larger than that of rhombohedral  $CsGeCl_3$  by about 1.62 times and KDP by about 9.63 times. Saturated PSHG integration results of increasing powder particle sizes revealed that rhombohedral  $CsGeBr_3$

was phase-matchable. The infrared transparent spectrum of rhombohedral  $CsGeBr_3$  was extended to more than  $22.5\mu m$ . The rhombohedral  $CsGeBr_3$  can be applied to infrared region as a potential nonlinear optical element.

Besides, hydrated rubidium Germanium chloride has been synthesized. Its single crystal with size of  $3 \times 2 \times 1 \text{ cm}^3$  is grown by slow evaporation in aqueous solution. The intensity of second harmonic generation effect is about one third of that of KDP, and is also phase-matchable. Infrared spectra, absorption-edge and Raman measurements indicate that the  $RbGeCl_3 \cdot xH_2O$  crystal (HRGC) is transparent in most of the IR region, and the transparent region ranges from  $0.31$  to  $30.84 \mu m$ . The HRGC's band gap is estimated to be  $3.84 \text{ eV}$ . These results show that HRGC can potentially be used as a new NLO crystal in the IR region.

Furthermore, working on another important category of materials, I have reported the results of the first principles calculations for the electronic properties, first- and second-order susceptibilities of the  $A^{II}B^{IV}N_2$  ( $A^{II}=\text{Be, Mg}$ ;  $B^{IV}=\text{C, Si, Ge}$ ) compounds with chalcopyrite structure

using the Linear Augmented Slater-Type Orbitals (LASTO) method. The second-order optical susceptibilities as functions of frequency for  $A^{II}B^{IV}N_2$  are also presented.  $BeGeN_2$  has the lowest bandgap value 2.68eV and the highest nonlinear optical responses,  $\chi_{xyz}^{(2)}=18.45\text{pm/V}$ . Our electronic band structure and density of states (PDOS) analysis reveal that the underestimate bandgaps of these chalcopyrite  $A^{II}B^{IV}N_2$  are wide enough (from 2.68eV to 4.24eV), and all locate at the  $\Gamma$ -point. Different from the other  $A^{II}B^{IV}N_2$  compounds, very heavy effective masses for highest occupied bands in  $MgSiN_2$  and  $MgGeN_2$ , are found. Our calculation results show that this new category of wide-bandgap ternary nitrides has potential applications in optoelectronics.

In final part, the electronic structures, optical and bulk properties of tetragonal nonlinear optical crystals,  $AgGa(S_xSe_{1-x})_2$  ( $x=0.0, 0.25, 0.5, 0.75, \text{ and } 1.0$ ), have been analyzed theoretically with first-principles calculation. In summary, the structural, electronic and optical properties of tetragonal nonlinear optical crystals,  $AgGa(S_xSe_{1-x})_2$  ( $x=0.0, 0.25, 0.5, 0.75, \text{ and } 1.0$ ), have been investigated theoretically and experimentally to reveal the cation substitution effect. The bond lengths of

$Ag - S$ ,  $Ag - Se$ ,  $Ga - S$ , and  $Ga - Se$  are found to vary with the substitution composition, but the bond length mismatch parameter  $u$  does not change. We found the major influence of cation substitution is to introduce cell volume changes. PDOS analysis shows that the valence band maximums (VBM) of  $AgGa(S_xSe_{1-x})_2$  is mainly contributed by the (3) $p$ -orbital of  $S$  and (4) $p$ -orbital of  $Se$  atoms. Their contribution to the total density of states is a simple weighted summation over  $S$  and  $Se$  compositions. The CBM and VBM are relatively shifted with the substitution concentration and the fundamental bandgap therefore reduces accordingly. The second harmonic generation coefficients  $\chi_{123}^{(2)}$  are also found to change with substitution. The substitution dependence can be ascribed to mainly from the bandgap change and minor contribution from the transition moment products. Based on our theoretical and experimental results, these materials could be useful for linear as well as nonlinear optical applications. We can choose the single-unit-cell model perform the other analysis instead of the supercell one in order to save the computation cost.

# Chapter 6

## Perspectives

Based on the previous studies and developments, some new classes of materials and their optoelectronic properties can be proposed and analyzed by using the first principles calculations for the electronic properties, first- and second-order susceptibilities.

First, the efficiency of numerical simulating optoelectronic properties on the nano-structures is still under-developed. There are a lot of interesting research topic in these realm, e.g., electronic band structure behavior of bilayer graphene with an external field.

Second, analyzing tools on some intrinsic electronic properties, e.g. the Auger recombination rates in nitride devices, the thermoelectric coeffi-

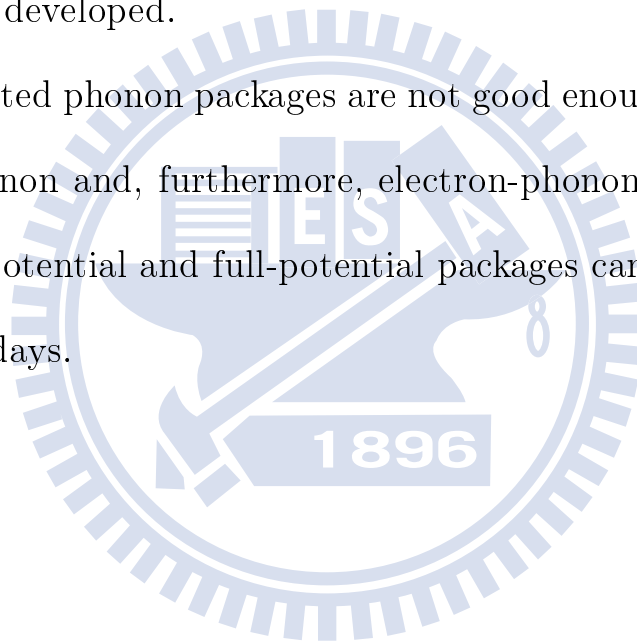


cients in some electronic cooling devices ..., etc, can be developed from first-principles density-functional-and many-body-perturbation theory.

Third, we can applying the understanding on material design in this study to the green energy materials, e.g., innovative solar cell materials, the hydrogen storage materials with more efficiency, ..., etc.

Forth, the analysis tools on the higher order susceptibilities of optical materials can be developed.

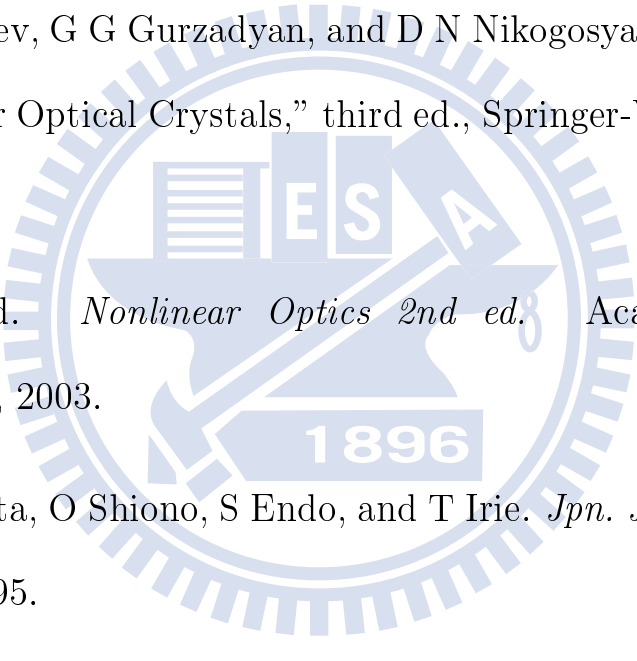
Finally, the updated phonon packages are not good enough. The useful and suitable phonon and, furthermore, electron-phonon analysis tools for both pseudopotential and full-potential packages can be go further in the following days.



## 參考文獻



# Bibliography

- 
- [1] V G Dmitriev, G G Gurzadyan, and D N Nikogosyan. "Handbook of Nonlinear Optical Crystals," third ed., Springer-Verlag, Berlin, 1999.
- [2] R W Boyd. *Nonlinear Optics 2nd ed.* Academic Press, Boston, MA, 2003.
- [3] H Matsushita, O Shiono, S Endo, and T Irie. *Jpn. J. Appl. Phys.*, 34:5546, 1995.
- [4] Y R Shen. *The Principles of Nonlinear Optics*. John Wiley and Sons, 2002.
- [5] R. H. Kingston. Parametric amplification and oscillation at optical frequencies. *Proc. IR*, 50:472, 1962.

- [6] J. A. Giordmaine and R. C. Miller. Tunable coherent parametric oscillation in  $\text{LiNbO}_3$  at optical frequencies. *Phys. Rev. Lett.*, 14(24):973, 1965.
- [7] D M Burland. *Chem. Rev.*, 94:1, 1994.
- [8] J Zyss in D S Chemla and J Zyss. *Nonlinear Optical Properties of Organic Molecules and Crystals*. Academic Press, Orlando, 1987.
- [9] L C Tang, L Q Liu, Y C Chang, J H Yau, J Y Huang, and C S Chang. *Jpn. J. Appl. Phys.*, 48(8):4, 2009.
- [10] L C Tang, Y C Chang, J Y Huang, M H Lee, and C S Chang. *Jpn. J. Appl. Phys.*, RP090260:(revised), 2009.
- [11] L C Tang, J Y Huang, C S Chang, M H Lee, and L Q Liu. *J. Phys.: Condens. Matter*, 17:7275, 2005.
- [12] Li-Chuan Tang, Chen-Shiung Chang, and Jung Y Huang. *J. Phys.: Condens. Matter*, 12:9129, 2000.
- [13] Chi-Ching Chang, Tzu-Chiang Chen, Li-Chuan Tang, and Hon-Fai Yau. Elimination of dynamic instabilities in the +c-face incident photorefractive  $\text{BaTiO}_3$  mutually pumped phase conjugator. *Jpn. J. Appl. Phys.*, 38:L567, 1999.

- [14] Tzu-Chiang Chen, Chi-Ching Chang, Li-Chuan Tang, and Hon-Fai Yau. High-resolution double self-pumped phase conjugations with +c-face incident configuration in a  $\text{batio}_3$ . *Jpn. J. Appl. Phys.*, 39:L1090, 2000.
- [15] Li-Chuan Tang, Chi-Ching Chang, Tzu-Chiang Chen, Hon-Fai Yau, and Pei-Xian Ye. Fast response self-pumped phase conjugator based on a +c-face incident configuration in a pentagon-shaped  $\text{batio}_3$  crystal. *Optical and Quantum Electronics*, 34:1241, 2002.
- [16] L C Tang, M H Lee, C H Yang, J Y Huang, and C S Chang. *J. Phys.: Condens. Matter*, 15:6043, 2003.
- [17] J F Nye. *Physical Properties of Crystals*. Oxford University Press, Oxford, 1957.
- [18] J Zhang, N Su, C Yang, J Qin, N Ye, B Wu, and C Chen. *Chem. Proc. SPIE*, 3556:1, 1998.
- [19] J Zhang. PhD thesis, Wuhan University, Department of Material Science, 1995.

- [20] M D Ewbank, F Cunningham, R Borwick, M J Rosker, and P Gunter. *CLEO97 paper*, CFA7:462, 1997.
- [21] M Hagemann and H-J Weber. *Appl. Phys. A*, 63:67, 1996.
- [22] QingTian Gu, QiWei Pan, Wei Shi, Xun Sun, and ChangShui Fang. *Prog. Cryst. Growth Charact. Mater.*, 40:89–95, 2000.
- [23] QingTian Gu, QiWei Pan, XiangWen Wu, Wei Shi, and ChangShui Fang. *J. Cryst. Growth*, 212:605–607, 2000.
- [24] QingTian Gu, ChangShui Fang, Wei Shi, XiangWen Wu, and QiWei Pan. *J. Cryst. Growth*, 225:501–504, 2001.
- [25] Peng Ren, Jingui Qin, and Chuangtian Chen. *Inorg. Chem.*, 42:8–10, 2003.
- [26] Peng Ren, Jingui Qin, Tao Liu, Yicheng Wu, and Chuangtian Chen. *Opt. Mater.*, 23:331–334, 2003.
- [27] U Schwarz, H Hillebrecht, M Kaupp, K Syassen, H.-G. von Schnering, and G Thiele. *Journal of Solid State Chemistry*, 118:20–27, 1995.
- [28] U Schwarz, F Wagner, K Syassen, and H Hillebrecht. *Phys. Rev. B*, 53(19):12545, 1996.

- [29] G Thiele, H W Rotter, and K D Schmidt. *Z. Anorg. Allg. Chem.*, 545:148, 1987.
- [30] G Thiele, H W Rotter, and K D Schmidt. *Z. Anorg. Allg. Chem.*, 559:7–16, 1988.
- [31] D-K Seo, N Gupta, M-H Whangbo, H Hillebrecht, and G Thiele. *Inorg. Chem.*, 37:407, 1998.
- [32] V M Goldschmidt. *Ber. Dtsch. Chem. Ges. [in German]*, 60:1263, 1927.
- [33] V M Goldschmidt. *Fortschr. Min. [in German]*, 15:73, 1931.
- [34] F S Galasso. *Perovskites and High *t* Superconductors*. Gordon and Breach, New York, 1990.
- [35] V Butler, C R Catlow, B E F Fender, and J H Harding. *Solid State Ionics*, 8:109V113, 1982.
- [36] L G Tejuca, J L G Fierro, and J M D Tascon. *Adv. Catal.*, 36:237V328, 1989.
- [37] H Yokokawa, N Sakai, T Kawada, and M Dokiya. *Solid State Ionics*, 52:43V56, 1992.

- [38] Noel W. Thomas. *Br. Ceram. Trans.*, 96:7V15, 1997.
- [39] R D Shannon and C T Prewitt. *Acta Crystallogr. Sect.*, B 25:925, 1969.
- [40] R D Shannon. *Acta Crystallogr. Sect.*, A 32:751V767, 1976.
- [41] P. Blaha, K. Schwarz, G. K. H. Madsen, D. Kvasnicka, and J. Luitz. *WIEN2K, An Augmented Plane Wave + Local Orbitals Program for Calculating Crystal Properties*. Karl-heinz Schwarz, Tech. Universitat Wien, Wien, Austria, 2001, ISBN 3-9501031-1-2.
- [42] S Siebentritt and U Rau. *Wide-Gap Chalcopyrites*. Springer-Verlag, Berlin, 2006.
- [43] Jung Y Huang, L C Tang, and M H Lee. *J. Phys.: Condens. Matter*, 13:10417, 2001.
- [44] V. L. Shaposhnikov, A. V. Krivosheeva, F. Arnaud D'Avitaya, J. L. Lazzari, and V. E. Borisenko. *Phys. Stat. Sol. (b)*, 245(1):142–148, 2008.
- [45] J E Sipe and E Ghahramani. *Phys. Rev. B*, 48:11705, 1993.
- [46] S C Abrahams and J L Bernstein. *J. Chem. Phys.*, 59:1625, 1973.



- [47] B Tell and H M Kasper. Optical and electrical properties of aggas2 and aggase2. *Phys. Rev. B*, 4:4455–4459, 1971.
- [48] J Camassel, L Artus, and J Pascual. *Phys. Rev. B*, 42:5717, 1990.
- [49] J E Jaffe and A Zunger. *Phys. Rev. B*, 28:5822, 1984.
- [50] J E Jaffe and A Zunger. *Phys. Rev. B*, 29:1882, 1984.
- [51] J. W. Davenport. *Phys. Rev. B*, 29:2896, 1984.
- [52] J. W. Davenport, M. Weinert, and R. E. Watson. *Phys. Rev. B*, 32:4876, 1985.
- [53] J. W. Davenport, R. E. Watson, and M. Weinert. *Phys. Rev. B*, 32:4883, 1985.
- [54] G. W. Fernando, J. W. Davenport, R. E. Watson, and M. Weinert. *Phys. Rev. B*, 40:2757, 1989.
- [55] Y.-C. Chang, R. B. James, and J. Davenport. *Phys. Rev. B*, 73:035211, 2006.
- [56] V Petrov, F Rotermond, and F Noack. *J. Opt. A: Pure Appl. Opt.*, 3, R1, 2001.

- [57] Sergey N. Rashkeev and Walter R. L. Lambrecht. *Phys. Rev. B*, 63:165212, 2001.
- [58] D A Roberts. *IEEE J. Quantum Electron*, 28:2057, 1992.
- [59] J C Mikkelsen Jr. and H Kidal. *J. Appl. Phys.*, 49(1):426, 1978.
- [60] N Yamamoto, A Mouri, M Seyoyama, and H Horinaka. *Jpn. J. Appl. Phys.*, 28(12):2513, 1989.
- [61] K Balakrishnan, B Vengatesan, and P Ramasamy. *Journal of Materials Science*, 29:1879, 1994.
- [62] M Robbins and V G Lambrecht. *Mater. Res. Bull.*, 8:703, 1973.
- [63] A G Jackson, M C Ohmer, and S R LeClair. *Infrared Phys. Technol.*, 38:233, 1997.
- [64] X. Gonze, J. M. Beuken, R. Caracas, F. Detraux, M. Fuchs, G. M. Rignanese, L. Sindic, M. Verstraete, G. Zerah, F. Jollet, M. Torrent, A. Roy, M. Mikam, Ph. Ghosez, J.-Y. Raty, and D. C. Allan. First-principles computation of material properties : the abinit software project. *Computational Materials Science*, 25:478–492, 2002.

- [65] X. Gonze, G. M. Rignanese, M. Verstraete, J. M. Beuken, Y. Pouillon, R. Caracas, F. Jollet, M. Torrent, M. Mikami G. Zerah, Ph. Ghosez, M. Veithen, J. Y. Raty, V. Olevano, F. Bruneval, L. Reining, R. Godby, G. Onida, D. R. Hamann, and D. C. Allan. A brief introduction to the abinit software package. *Zeit. Kristallogr.*, 220:558–562, 2005.
- [66] M C Payne, M P Teter, D C Allan, T A Arietas, and J D Joannopoulos. *Rev. Mod. Phys.*, 64:1045, 1992.
- [67] M. D. Segall, P. L. D. Lindan, M. J. Probert, C. J. Pickard, P. J. Hasnip, S. J. Clark, and M. C. Payne. *J. Phys.: Condens. Matter*, 14(11):2717, 2002.
- [68] A N Christensen and S E Rasmussen. *Acta Chem. Scand.*, 19:421, 1965.
- [69] I V Tananaev, D F Dzhurinskii, and Yu N Mikhailov. *Zh. Neorgan. Khim [in Russian]*, 9(7):1570–7, 1964.
- [70] L Nyqvist and G Johnsson. *Acta Chem. Scand.*, 25:1615, 1971.
- [71] W K Chen, C M Cheng, J Y Huang, W F Hsieh, and T Y Tseng. *J. Phys. Chem. Solids*, 61:969–977, 2000.

- [72] S K Kurtz and T T Perry. *J. Appl. Phys.*, 39:3798–3813, 1968.
- [73] J P Dougherty and S K Kurtz. *J. Appl. Crystallogr.*, 9:145–158, 1976.
- [74] R W Boyd. *Nonlinear Optics*. Academic Press, Boston, MA, 1992.
- [75] A Graja. *Acta Phys. Pol. A*, 37:539, 1970.
- [76] P N Prasad and D J Williams. *Introduction to Nonlinear Optical Effects in Molecules and Polymers, chap. 6*. Wiley, New York, 1991.
- [77] H J Monkhorst and J D Pack. *Phys. Rev. B*, 13:5188, 1976.
- [78] C Aversa and J E Sipe. *Phys. Rev. B*, 52:14636, 1995.
- [79] A Dal Corso and F Mauri. *Phys. Rev. B*, 50:5756, 1994.
- [80] D J Moss, J E Sipe, and H M van Driel. *Phys. Rev. B*, 36:1153, 1987.
- [81] D J Moss, E Ghahramani, J E Sipe, and H M van Driel. *Phys. Rev. B*, 41:1542, 1990.
- [82] E Ghahramani, D J Moss, and J E Sipe. *Phys. Rev. B*, 43:8990, 1991.

- [83] E Ghahramani, D J Moss, and J E Sipe. *Phys. Rev. B*, 43:9700, 1991.
- [84] D J Moss, E Ghahramani, and J E Sipe. *Phys. Status Solidi B*, 164:587, 1991.
- [85] M Z Huang and W Y Ching. *Phys. Rev. B*, 45:8738, 1992.
- [86] M Z Huang and W Y Ching. *Phys. Rev. B*, 47:9464, 1993.
- [87] W Y Ching and M Z Huang. *Phys. Rev. B*, 47:9479, 1993.
- [88] Z H Levine and D C Allan. *Phys. Rev. B*, 44:12781, 1991.
- [89] V Fiorentini, M Methfessel, and M Scheffler. *Phys. Rev. B*, 47:13353, 1993.
- [90] A F Wright and J S Nelson. *Phys. Rev. B*, 50:2159, 1994.
- [91] K Karch, F Bechstedt, and T Pletl. *Phys. Rev. B*, 56:3560, 1997.
- [92] V Milman, M H Lee, and M C Payne. *Phys. Rev. B*, 49:16300, 1994.
- [93] Francis Birch. Finite elastic strain of cubic crystals. *Physical Review*, 71:809–824, 1947.

- [94] H Krakauer, M Posternak, and A J Freeman. *Phys. Rev. B*, 19:1706, 1979.
- [95] E Wimmer, H Krakauer, M Weinert, and A J Freeman. *Phys. Rev. B*, 24:864, 1981.
- [96] D Sanchez-Portal, E Artacho, and J M Soler. *J. Phys.: Condens. Matter*, 8:3859, 1996.
- [97] M. D. Segall, C. J. Pickard, R. Shah, and M. C. Payne. *Mol. Phys.*, 89:571, 1996.
- [98] M. D. Segall, R. Shah, C. J. Pickard, and M. C. Payne. *Phys. Rev. B*, 54:16317, 1996.
- [99] S N Rashkeev, W R L Lambrecht, and B Segall. *Phys. Rev. B*, 57:3905, 1998.
- [100] C G Duan, J Li, Z Q Gu, and D S Wang. *Phys. Rev. B*, 59:369, 1999.
- [101] Benoît Champagne and David M. Bishop. *Advances in Chemical Physics*, 126:41, 2003.
- [102] W Kraus and G Nolze. *J. Appl. Cryst.*, 29:301–303, 1996.

- [103] D A Kleinman. *Phys. Rev.*, 126:1977–1979, 1962.
- [104] U Opik and M H L Pryce. *Proc. R. Soc. London Sect., A* 238:425–447, 2003.
- [105] R F W Bader. *Mol. Phys.*, 3:137–151, 1960.
- [106] R F W Bader. *Can. J. Chem.*, 40:1164–1175, 1962.
- [107] R G J Pearson. *J. Am. Chem. Soc.*, 91:4947–4955, 1969.
- [108] R G J Pearson. *Mol. Struct.: THEOCHEM*, 103:25–34, 1983.
- [109] R A Wheeler, M.-H. Whangbo, T Hughbanks, R Hoffmann, J K Burdett, and T A J Albright. *J. Am. Chem. Soc.*, 108:2222–2236, 1986.
- [110] M Kunz and I D J Brown. *Solid State Chem.*, 115:395–406, 1995.
- [111] Robert C. Eckardt, Hisashi Masuda, Yuan Xuan Fan, and Robert L. Byer. Absolute and relative nonlinear optical coefficients of kdp, kd\*p, bab,04, lao3, mgo: Limo3 and ktp measured by phase-matched second-harmonic generation. *IEEE J. Quantum Electron.*, 26:922–933, 1990.
- [112] C Fong and J C Phillips. *Phys. Rev. B*, 14:5387, 1976.

- [113] J C Wooly, R K Williardson, and H L Goering. *Compound Semiconductors*. Reinhold, New York, 1962.
- [114] R W G Wyckoff. *Crystal Structures*. Interscience Publishers, New York, 1963.
- [115] V. L. Shaposhnikov, A. V. Krivosheeva, F. Arnaud D'Avitaya, J.-L. Lazzari, and V. E. Borisenko. *Phys. Stat. Sol. (b)*, 245(1):142–148, 2008.
- [116] P. Eckerlin. *Z. Anorg. Allg. Chem.*, 533:225, 1967.
- [117] L. D. Zhu, P. H. Maruska, P. E. Norris, P. W. Yip, and L. O. Bouthillette. *MRS Internat J. Nitride Semicond. Res.*, 4S1(G3):8, 1999.
- [118] T. Misaki, A. Wakahara, H. Okada, and A. Yashida. *J. Cryst. Growth*, 260:125, 2004.
- [119] M. Winterberger, M. Maunaye, and Y. Laurent. *Mater. Res. Bull.*, 8:1049, 1973.




# 附錄



# Appendix A

## Acronym

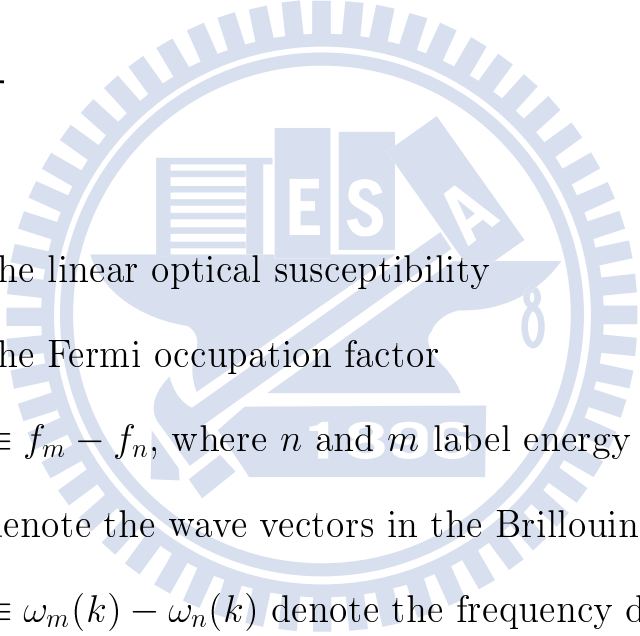
- 
- BZ : the Brillouin-Zone
- CGB :  $\text{CsGeBr}_3$ , Cesium Germanium Bromide
- CGC :  $\text{CsGeCl}_3$ , Cesium Germanium Chloride
- CGI :  $\text{CsGeI}_3$ , Cesium Germanium Iodide
- CGX :  $\text{CsGeX}_3$ , X=Cl, Br, or I, Cesium Germanium Halides
- CASTEP : CAMbridge Serial Total Energy Package
- ABINIT : *ab initio*; ABINIT is a package whose main program allows one to find the total energy, charge density and electronic structure of systems made of electrons and nuclei (molecules and periodic solids) within Density Functional Theory (DFT),

using pseudopotentials and a planewave basis

SHG	: Second Harmonic Generation
PSHG	: Powder Secon Harmonic Generation
PDOS	: Partial or projected density of states
PPP	: the planewave basis set in planewave pseudopotential scheme
LDOS	: Local density of states
MME	: the momentum matrix element
NLO	: Non-linear Optics or Non-linear Optical
LCAO	: Linear Combination of Atomic Orbitals
LASTO	: the Linear Augmented Slater-Type Orbitals method
DFT	: Density Functional Theory
TDOS	: Total density of states

# Appendix B

## Notation

- 
- $\chi_I^{ab}(-\omega; \omega)$  : the linear optical susceptibility
- $f_i$  : the Fermi occupation factor
- $f_{mn}$  :  $\equiv f_m - f_n$ , where  $n$  and  $m$  label energy bands
- $\mathbf{k}$  : denote the wave vectors in the Brillouin zone
- $\omega_{mn}(k)$  :  $\equiv \omega_m(k) - \omega_n(k)$  denote the frequency differences
- $r_{mn}$  : are the dipole matrix elements
- $\Delta$  : denotes the constant shift used in the 'scissors approximation' to correct the energy band gap difference caused by the local density approximation
- $v_{mn}$  : the velocity matrix elements via  $r_{mn} = v_{mn}/(i\omega_{nm})$
- $\delta_{mc}$  : =1, if band  $m$  denotes one of the conduction bands

- $t_G$  : Goldschmidt tolerance factor
- $\Delta\alpha$  : the deviation percentage of lattice angles in comparison to the ideal perovskite structure.
- $d_{Ge}^{rhom}$  : the displacement percentage of the smaller B-site cation, Germanium, displaces along the diagonal axis from the cell center to the corner in a perovskite structure
- $d_X^{rhom}$  : the displacement percentage of the anion, halides, displaces from the face center to the center in a perovskite structure
- $u$  : an internal tetrahedral distortion parameter in the chalcopyrite structure with respect to the zinc-blende cubic structure, can be used as a measure of bond-length mismatch
- $\eta$  : a structural tetragonal distortion parameter of the chalcopyrite structure with respect to the zinc-blende cubic structure, is the ratio lattice of c-axis and a-axis,  $\eta = c/2a$ , which is not always =1.
- $E_g$  : the energy band gap
- $\Psi_{nk}(\vec{r})$  : be the self-consistent wave function of the crystal at the  $n$ -th band and  $k$ -th point in the Brillouin-Zone (BZ)
- $\Phi_{lm}^{(i)}(\vec{r})$  :  $\Psi_{nk}(\vec{r})$  can be decomposed into a linear

- combination of the atomic orbitals of the  $l$ -th orbital  $i$ -th atom
- $C_{nk,lm}^{(i)}$  : denotes the projection coefficients of  $\int_{V_o} \Psi_{nk}(\vec{r}) \cdot \Phi_{lm}^{(i)*}(\vec{r}) dV$
- $h_{nk,l}^{(\beta)}$  : Thea fraction of  $l$ -th orbital of the  $\beta$ -species contributes to the population in  $\Psi_{nk}(\vec{r})$
- $\lambda$  : wavelength
- $\alpha_{ij}(\omega)$  : is the absorption coefficient and is related to the imaginary part of the dielectric function by [99]
- $f_c$  : reperedented the Fermi distribution of the conduction band  $c$
- $f_v$  : reperedented the Fermi distribution of the valence band  $v$
- $p_{cv}^i(k, \text{\AA}^{-1})$  : denoted the momentum matrix element (MME, in unit of  $\text{\AA}^{-1}$ ) from the conduction band  $c$  to the valence band  $v$  at the  $k$  point of the BZ
- $I_{2\omega}$  : the total second-harmonic intensity
- $L$  : a crystal plate with thickness
- $\epsilon_{ij}(\vec{q}, \omega)$  : the dielectric function
- $I_\omega$  : is the intensity of the incident fundamental beam
- $n_\omega, n_{2\omega}$  : are the indices of refraction of the crystal plate in the fifferent frequencies
- $d_{eff}$  : the effective nonlinearity of the crystal plate

- $\chi_{ijk}^{(n)}$  : the n-th order nonlinear susceptibility of the crystal in i-, j-, and k-components
- $\bar{r}$  : denotes the averaged particle size
- $\bar{l}_c$  : is the coherent length of crystalline powders
- $\langle d_{eff}^2 \rangle$  : the square of the effective nonlinearity averaged over the orientation distribution of crystalline powders
- $\bar{l}_{pm}$  : is the phase-matching length of crystalline powders
- $\theta_{pm}$  : is the phase matching angle
- $\Delta n_{B,2\omega}$  : denotes the birefringence of material at the second-harmonic wavelength

